

Finite Element Analysis of a Plated Mid-Shaft Fracture of the Humerus

Ardavan Sufi Siavash

A Thesis
in
The Department
of
Mechanical and Industrial Engineering

Presented in Partial Fulfillment of the Requirements
for the Degree of Master of Applied Science (Mechanical Engineering) at
Concordia University

Montréal, Québec, Canada

March 2008

© Ardavan Sufi Siavash, 2008



Library and
Archives Canada

Bibliothèque et
Archives Canada

Published Heritage
Branch

Direction du
Patrimoine de l'édition

395 Wellington Street
Ottawa ON K1A 0N4
Canada

395, rue Wellington
Ottawa ON K1A 0N4
Canada

Your file Votre référence
ISBN: 978-0-494-40925-1
Our file Notre référence
ISBN: 978-0-494-40925-1

NOTICE:

The author has granted a non-exclusive license allowing Library and Archives Canada to reproduce, publish, archive, preserve, conserve, communicate to the public by telecommunication or on the Internet, loan, distribute and sell theses worldwide, for commercial or non-commercial purposes, in microform, paper, electronic and/or any other formats.

The author retains copyright ownership and moral rights in this thesis. Neither the thesis nor substantial extracts from it may be printed or otherwise reproduced without the author's permission.

AVIS:

L'auteur a accordé une licence non exclusive permettant à la Bibliothèque et Archives Canada de reproduire, publier, archiver, sauvegarder, conserver, transmettre au public par télécommunication ou par l'Internet, prêter, distribuer et vendre des thèses partout dans le monde, à des fins commerciales ou autres, sur support microforme, papier, électronique et/ou autres formats.

L'auteur conserve la propriété du droit d'auteur et des droits moraux qui protègent cette thèse. Ni la thèse ni des extraits substantiels de celle-ci ne doivent être imprimés ou autrement reproduits sans son autorisation.

In compliance with the Canadian Privacy Act some supporting forms may have been removed from this thesis.

Conformément à la loi canadienne sur la protection de la vie privée, quelques formulaires secondaires ont été enlevés de cette thèse.

While these forms may be included in the document page count, their removal does not represent any loss of content from the thesis.

Bien que ces formulaires aient inclus dans la pagination, il n'y aura aucun contenu manquant.

■+■
Canada

Abstract

Finite element analysis of a plated mid-shaft fracture of the humerus

Ardavan Sufi Siavash

Internal fixation with rigid metal plates is a widely accepted technique for the treatment of bone fractures. The objective of this study is to evaluate the response of bone, fracture plate, screws and callus at different stages of healing to various applied loads. A three-dimensional, half-symmetric finite element model was developed. The stress and strain states in the assembly were investigated for pure compression, pure tension, twisting moment and combination of compressive and shear forces, which generate a bending moment, simulating getting up from a chair, carrying a suitcase and turning a screw driver. Two types of commonly used fracture plates were compared: 316 stainless steel and Ti-6Al-4V titanium alloy.

The results of this research showed that there is less stress shielding of the bone with the titanium alloy plate and screws than with the stainless steel ones. The maximum equivalent von-Mises stress was found to be less in compression and tension than in bending and twisting. The majority of load transfer within the assembly occurred in the screws. For large bending and twisting moments stresses can be higher than the strength of the stainless steel plate. Excessive loading should thus be avoided to prevent possible failure. The research further found that the relative motion between bone and fracture plate was largest during tensile loading.

Acknowledgements

I am most grateful to my supervisor, Dr. Gerard J. Gouw, for his encouragement, support, and patience throughout this research. Without his help, advice and positive attitude, my studies in this area would not have been possible.

I would also like to thank, my family for their great love. Their support was a major factor in the success of my work.

Table of Contents

List of figures.....	viii
List of tables.....	xiii
List of symbols and abbreviations	xvii
Glossary	xviii
1. Introduction and scope of the thesis research	1
1.1 Thesis outline.....	2
2. Background and literature review.....	4
2.1 Basic long bone structure.....	4
2.2 Bone fracture.....	6
2.3 Fracture healing mechanisms.....	7
2.3.1 The union phase of fracture healing.....	8
2.3.2 The remodeling phase of fracture healing	12
2.4 Stress shielding	12
2.5 Mechanical properties of long bones	13
2.6 Fracture fixation methods	17
2.6.1 Non-operative methods.....	17
2.6.2 Operative methods	19
2.7 Finite element analysis of fracture fixation	24
3. Development of the finite element model.....	39
3.1 Bone model	39
3.2 Fracture plate model	41
3.3 Screw model.....	42
3.4 Mesh generation.....	43
3.4.1 Bone	44
3.4.2 Callus	45
3.4.3 Fracture plate and screws.....	48
3.5 Modeling the interfaces.....	49
3.5.1 Fracture plate – screws head interface	50
3.5.2 Bone – screw interface.....	51
3.5.3 Bone – fracture plate interface.....	52

3.6	Materials selection	54
3.6.1	Bone	54
3.6.2	Fracture plate and screws.....	54
3.7	Boundary conditions	57
3.7.1	Constraints	57
3.7.2	Loading conditions.....	59
4.	Results and discussion	67
4.1	Load case 1 – pure compression	68
4.1.1	Stress distribution in the bone: pure compression case	69
4.1.2	Stress distribution in the plate: pure compression case	71
4.1.3	Stress distribution in the screws: pure compression case	72
4.1.4	Stress distribution in the callus: pure compression case	74
4.1.5	Summary and discussion of the stresses: pure compression case.....	76
4.1.6	Elastic strains: pure compression case	77
4.1.7	Contact analysis of the bone-plate interface: pure compression case.....	77
4.2	Load case 2 – pure tension.....	80
4.2.1	Stress distribution in the bone: pure tension case	80
4.2.2	Stress distribution in the plate: pure tension case	82
4.2.3	Stress distribution in the screws: pure tension case	84
4.2.4	Stress distribution in the callus: pure tension case.....	85
4.2.5	Summary and discussion of the stresses: pure tension case	86
4.2.6	Elastic strains: pure tension case.....	87
4.2.7	Contact analysis of the bone-plate interface: pure tension case	88
4.3	Load case 3 – combined compression and shear force	91
4.3.1	Assembly with the stainless steel plate.....	91
4.3.2	Assembly with the titanium plate	100
4.4	Summary and discussion: compression and shear case	110
4.4.1	Summary and discussion of the stresses for both plates:	
	compression and shear case	110
4.4.2	Summary and discussion of the strains for both plates:	
	compression and shear case	111

4.4.3	Summary and discussion of the contact analysis at the interface of.....	
	bone-fracture plate	113
4.5	Load case 4 – twisting moment	115
4.5.1	Stress distribution in the bone: twisting moment case.....	115
4.5.2	Stress distribution in the plate: twisting moment case.....	118
4.5.3	Stress distribution in the screws: twisting moment case.....	118
4.5.4	Stress distribution in the callus: twisting moment case	120
4.5.5	Summary and discussion of the stresses: twisting moment case	121
4.5.6	Elastic strain: twisting moment case.....	122
4.5.7	Contact analysis of the bone-plate interface: twisting moment case	123
5.	Conclusion and future work.....	125
6.	References.....	128

List of figures

Figure 2.1: A mature long bone - partially sectioned (Thibodeau and Kevin, 2007).....	5
Figure 2.2: Fracture healing: fracture damages (1) – periosteum partly or completely, (2) – haversian systems, (3) – muscles and their neighboring nerves and blood vessels, and (4) skin (McRae, 2002)	9
Figure 2.3: The periosteum is partially torn (McRae, 2002)	10
Figure 2.4: Fracture gap is bridged with a rigid callus (McRae, 2002).....	10
Figure 2.5: The bone ends are not aligned (McRae, 2002).....	11
Figure 2.6: Medullary canal at fracture site fills with blood and soft tissues (McRae, 2002)	11
Figure 2.7: (1) Bone reduction, (2) long arm plaster and (3) collar and cuff sling..... (McRae, 2002)	18
Figure 2.8: (1) Weights and pulley system, (2) traction cord, (3) support for..... the proximal end of the splint, and (4) Thomas Splint ring (McRae, 2002)...	19
Figure 2.9: Lateral condylar fracture which is held by two k-wires in its position (McRae, 2002)	20
Figure 2.10: Mid-shaft fracture of humerus (1) fracture fixation plate, (2) screws..... (McRae, 2002)	21
Figure 2.11: Forearm fractures and fracture fixation plates (Saidpour, 2006)	21
Figure 2.12: Proximal fracture of humerus which is fixed by intermedullary..... nail with proximal and distal bolting (McRae, 2002).....	22
Figure 2.13: Humerus three-part fractures, (1) articular surface, (2) cancellous..... screw, and (3) tension band (McRae, 2002)	22
Figure 2.14: Left: 4.5mm diameter cortical screw, Right: 3.5mm diameter cancellous..... screw (Fazzini).....	23
Figure 2.15: A broken femur which is treated by an external fixator (McRae, 2002).....	23
Figure 2.16: Plate reinforced bone system under pure bending.....	28
Figure 2.17: Part of a waisted fracture plate (Saidpour, 2006).....	29
Figure 2.18: Fracture plate under flexural loading. Top: FEA, Bottom: Destructive test (Saidpour, 2006)	30

Figure 2.19: Von-Mises stress distribution in waisted fracture plate models loaded	
in torsion (Saidpour, 2006)	31
Figure 2.20: Fracture plate under torsional load. Top: FEA, Bottom: Destructive test.....	
(Saidpour, 2006)	31
Figure 2.21: Titanium plate configurations used for stress analyses: A: ladder type	
plate, B: two small plates, C: large/small plates, and D: large plate.....	34
Figure 2.22: a) a solid model of the distal radius, b) L-plate and straight plate profiles	
(Lin et al, 2006).....	35
Figure 2.23: a) axial load, b) bending moment, c) torsion (Lin et al, 2006).....	36
Figure 3.1: Finite element model of the humerus	41
Figure 3.2: Fracture fixation plate (Narang Medical Limited)	42
Figure 3.3: Finite element model of the fracture plate.....	42
Figure 3.4: Cortical Screw (Fazzini).....	43
Figure 3.5: Finite element model of the screw	43
Figure 3.6: Left: Solid187 faces, Right: Solid 187 cross-section (Ansys).....	44
Figure 3.7: Solid187 geometry (Ansys).....	44
Figure 3.8: Bone model (distal humerus) mesh	45
Figure 3.9: Solid187 geometry (Ansys).....	46
Figure 3.10: Callus mesh	46
Figure 3.11: 20-node quadratic pyramid elements	47
Figure 3.12: Fracture plate mesh	48
Figure 3.13: Screw mesh.....	48
Figure 3.14: Fracture plate – screw heads interface	51
Figure 3.15: Bone – screw interface	52
Figure 3.16: Bone – fracture plate interface	53
Figure 3.17: Symmetry plane.....	58
Figure 3.18: Displacement at the proximal end of humerus	58
Figure 3.19: Pretension in a screw	59
Figure 3.20: Diagram of upper arm and lower arm	61
Figure 3.21: Free body diagram of lower arm	62
Figure 3.22: Free body diagram of the upper arm	63

Figure 3.23: Modified free body diagram of the upper arm	64
Figure 4.1: Finite element model of bone, plate, screws and callus	67
Figure 4.2: Stress distribution in the model with a SS plate for the 1 st week of healing..	69
Figure 4.3: Stress distribution in the bone with the SS fracture plate for the 6 th week	
of healing	70
Figure 4.4: Stress distribution in the bone with the Ti fracture plate for the 6 th week	
of healing	70
Figure 4.5: Stress distribution in the SS plate for the 1 st of week of healing.....	71
Figure 4.6: Stress distribution in the SS plate for the 3 rd week of healing	72
Figure 4.7: Stress distribution in the stainless steel screws for the 1 st week of healing ...	73
Figure 4.8: Stress distribution in the titanium screws for the 1 st week of healing.....	73
Figure 4.9: Stress distribution in the stainless steel screws for the 8 th week of healing ...	74
Figure 4.10: Stress distribution in the callus during different stages of the healing.....	
process in case of a SS plate	75
Figure 4.11: Contact at the bone and the SS plate interface for the 3 rd week of healing..	78
Figure 4.12: Relative motion between the bone and the SS plate for the 3 rd week	
of healing	79
Figure 4.13: Stress distribution in bone with the SS fracture plate for the 1 st week.....	
of healing	81
Figure 4.14: Stress distribution in bone with the Ti fracture plate for the 1 st week.....	
of healing	81
Figure 4.15: Stress distribution in the SS plate for the 1 st of week of healing.....	83
Figure 4.16: Stress distribution in the SS plate for the 3 rd week of healing	83
Figure 4.17: Stress distribution in the titanium screws for the 1 st week of healing.....	84
Figure 4.18: Stress distribution in the stainless steel screws for the 3 rd week of healing.	85
Figure 4.19: Stress distribution in the callus at different stages of healing in case	
of a Ti plate	86
Figure 4.20: Relative motion between the bone and the SS plate for the 1 st week of	
healing.....	89
Figure 4.21: Relative motion between the bone and the Ti plate for the 1 st week of	
healing.....	89

Figure 4.22: Contact at the bone and the SS plate interface for the 3 rd week of healing..	90
Figure 4.23: Stress distribution in the bone for the 3 rd week of healing (SS, $\alpha=45^\circ$)	92
Figure 4.24: Stress distribution in the SS fracture plate for the.....	
1 st week of healing ($\alpha=45^\circ$)	93
Figure 4.25: Stress distribution in the SS fracture plate for the.....	
3 rd week of healing ($\alpha=45^\circ$).....	94
Figure 4.26: Stress distribution in the stainless steel screws for the.....	
1 st week of healing ($\alpha=45^\circ$)	95
Figure 4.27: Stress distribution in the stainless steel screws for the.....	
3 rd week of healing ($\alpha=45^\circ$).....	96
Figure 4.28: Contact at the bone and the SS fracture plate interface for the	
3 rd week of healing ($\alpha=30^\circ$).....	99
Figure 4.29: Relative motion between the bone and the fracture plate for the.....	
1 st week of healing ($\alpha=15^\circ$)	99
Figure 4.30: Relative motion between the bone and the fracture plate for the.....	
6 th week of healing ($\alpha=15^\circ$)	100
Figure 4.31: Stress distribution in the bone for the 3 rd week of healing ($\alpha=45^\circ$).....	101
Figure 4.32: Stress distribution in the Ti fracture plate for the 1 st week of healing	
($\alpha=15^\circ$)	102
Figure 4.33: Stress distribution in the Ti fracture plate for the 1 st week of healing	
($\alpha=30^\circ$)	103
Figure 4.34: Stress distribution in the Ti fracture plate for the 1 st week of healing	
($\alpha=45^\circ$)	104
Figure 4.35: Stress distribution in the callus at different stages of healing	
in the case of a Ti plate ($\alpha=30^\circ$)	106
Figure 4.36: Contact at the bone and the Ti fracture plate interface for the	
3 rd week of healing ($\alpha=30^\circ$).....	108
Figure 4.37: Relative motion between the bone and the Ti fracture plate for the	
1 st week of healing ($\alpha=45^\circ$)	108

Figure 4.38: Relative motion between the bone and the Ti fracture plate for	
the 6 th week of healing ($\alpha=45^\circ$)	109
Figure 4.39: Relative motion changes with respect to the stage of healing in the.....	
model with the SS plate	114
Figure 4.40: Relative motion changes with respect to the stage of healing in the.....	
model with the Ti plate	114
Figure 4.41: Stress distribution in the bone with the SS plate for the 3 rd week.....	
of healing	116
Figure 4.42: Stress distribution in the Ti fracture plate for the 1 st week of healing	117
Figure 4.43: Stress distribution in the Ti fracture plate for the 6 th week of healing	117
Figure 4.44: Stress distribution in the titanium screws for the 1 st week of healing	119
Figure 4.45: Stress distribution in the stainless steel screws for the 8 th week of.....	
healing.....	119
Figure 4.46: Stress distribution in the callus at different stages of healing in.....	
case of the SS plate	121
Figure 4.47: Relative motion between the bone and the Ti plate for the 3 rd week of.....	
healing.....	123
Figure 4.48: Contact at the bone and the Ti plate interface for the 3 rd week of healing.	124

List of tables

Table 2.1: Average technical constants for bone (Ashman and van Buskirk, 1986).....	14
Table 2.2: Material properties of cortical bone (Ramakrishna et al., 2004)	14
Table 2.3: Young's modulus and Poisson's ratio of the humerus (Zadpoor, 2005).....	15
Table 2.4: Material properties used in finite element analysis (Lovald et al., 2006).....	15
Table 2.5: Material properties of human tibia (Ionescu et al., 2003).....	16
Table 2.6: Material properties of cortical bone (Lin et al., 2006).....	16
Table 2.7: Material properties of young and old cortical bone (Clavert et al., 2006).....	16
Table 2.8: Summary of different material properties.....	17
Table 2.9: Design parameters of bone plate and calculated stress values	27
Table 2.10: Material properties of callus at different stages of healing.....	32
Table 2.11: Stress variation at the bone fracture-interface for SS, SGT and SGL plate	
fixations at different stages of bone healing (based on Ganesh et al., 2005)	33
Table 2.12: Magnitude of stresses in the fracture plate during the 50% of healing	
(Ganesh et al., 2005)	34
Table 2.13: Maximum equivalent von-Mises stress for the bone under different load	
conditions.....	37
Table 2.14: Displacement at the radius end of the model.....	37
Table 2.15: The approximate maximum strain on the healing fracture interface	37
Table 3.1: Dimensions of male and female aboriginal humerus (mm).....	40
Table 3.2: Finite element model statistics.....	49

Table 3.3: Elements statistics.....	49
Table 3.4: Material properties of cortical bone (Ramakrishna et al., 2004)	54
Table 3.5: Material properties statistics	57
Table 3.6: Weights and centers of gravity of body segments (Pheasant, 1986)	60
Table 3.7: Compressive and shear force in elbow with respect to the angle of.....	
lower arm and armrest.....	64
Table 3.8: Maximum twisting moment applied to the humerus	65
Table 3.9: Summary of load cases investigated.....	66
Table 4.1: Maximum equivalent von-Mises stresses in different parts of the assembly ..	76
Table 4.2: Maximum equivalent elastic von-Mises strains in different parts of the.....	
assembly	77
Table 4.3: Maximum relative motions at the interface of bone and fracture plate	79
Table 4.4: Maximum equivalent von-Mises stresses in different parts of the assembly ..	87
Table 4.5: Maximum equivalent elastic von-Mises strains in different parts of the.....	
assembly	88
Table 4.6: Maximum relative motions at the bone and the fracture plate interface	90
Table 4.7: Compressive and shear forces	91
Table 4.8: Maximum equivalent von-Mises stresses in the bone at different	
stages of healing.....	92
Table 4.9: Maximum equivalent von-Mises stresses in the SS plate at different.....	
stages of healing.....	94
Table 4.10: Maximum deflections in the SS fracture plate	95

Table 4.11: Maximum equivalent von-Mises stresses in the screws at different	
stages of healing	96
Table 4.12: Maximum equivalent von-Mises stresses at different stages of healing	97
Table 4.13: Maximum equivalent elastic von-Mises strains in different parts.....	
of the assembly.....	98
Table 4.14: Maximum relative motions at the bone - SS plate interface.....	100
Table 4.15: Maximum equivalent von-Mises stresses in the bone at different	
stages of healing	102
Table 4.16: Maximum equivalent von-Mises stresses in the Ti plate at different.....	
stages of healing.....	104
Table 4.17: Maximum deflections in the Ti fracture plate	105
Table 4.18: Maximum equivalent von-Mises stresses in the screws at different	
stages of healing.....	105
Table 4.19: Maximum equivalent von-Mises stresses in the callus at different.....	
stages of healing	106
Table 4.20: Maximum equivalent elastic Von Mises strains in different parts of the.....	
assembly	107
Table 4.21: Maximum relative motions at the interface of the bone and the Ti plate	109
Table 4.22: Maximum equivalent von-Mises stresses at different stages of healing	110
Table 4.23: Maximum equivalent von-Mises stresses at different stages of healing	112
Table 4.24: Maximum relative motions at the interface of bone and fracture plate.....	113
Table 4.25: Maximum equivalent von-Mises stresses in different parts of the.....	
assembly	122

Table 4.26: Maximum equivalent elastic von-Mises strains in different parts.....	
of the assembly.....	123
Table 4.27: Maximum relative motions at the interface of bone-fracture plate	124

List of symbols and abbreviations

AFP	Axially flexible plate
CFRP	Carbon fiber reinforced plastic
E_1, E_2, E_3	Young's modulus
EI	Bending stiffness
F_C	Compressive force
FEM	Finite element methods
F_T	Transverse (shear) force
F_{Triceps}	Triceps force
G_{12}, G_{13}, G_{23}	Shear modulus
H_E	Horizontal elbow force
H_S	Horizontal shoulder force
PLLA	Poly-L-lactide
SG	Stiffness graded
SGL	Stiffness graded in length
SGT	Stiffness graded in thickness
V_E	Vertical elbow force
V_S	Vertical shoulder force
$\gamma, \gamma_{12}, \gamma_{13}, \gamma_{21}, \gamma_{23}, \gamma_{32}, \gamma_{32}$	Poisson's ratio

Glossary

Diaphysis	Long bone shaft
Distal	Further away from the trunk
Epiphyses	Long bone head
Femur	Thigh bone
Fibula	A small bone next to the shin bone
Haversian systems	Fundamental functional unit of compact bone
Humerus	Upper arm bone
Mandible	Lower jaw bone
Osteoblasts	Bone-forming cells
Osteoclasts	Bone-destroying cells
Osteon	The chief structural unit of compact bone
Periosteum	Vascular membrane surrounding long bones
Phalanges	Finger and toe bones
Proximal	Closer to the trunk
Radius	Forearm bone
Tibia	Shin bone
Ulna	Elbow bone

1. Introduction and scope of the thesis research

Internal fixation with rigid metal plates used in conjunction with specially designed screws is a widely accepted technique for the treatment of bone fractures. Fracture plates and screws are often fabricated of metallic alloys, with stainless steel and titanium Ti-6Al-4V being commonly. While there are various designs for both fracture plates and screws, the main reasons for using internal fixation plates is to provide excellent reduction of the bone fragments, hold the broken bone in the proper position and keep the parts aligned.

The main objective of this study is to generate a Finite Element Model (FEM) of an internal fracture fixation plate for a mid-shaft fracture of the humerus, in order to investigate the state of internal stress and strain in the assembly, as well as to examine and compare the performance of the assembly under different load conditions.

The high stiffness of a fracture fixation plate compared to the bone may have a stress shielding effect on the underlying bone, and the bone may fracture again after the plate is removed. Reducing the stiffness of the fixation plate is a way to reduce the stress shielding effect, but at the same time it may cause pain, discomfort and also non-union healing. In order to compromise between the stiffness and the strength, two plates are used in this study and their performance is evaluated. The evaluation demonstrates how the addition of a rigid fracture fixation plate can change the mechanical properties of the underlying bone during different stages of fracture healing.

Another aspect of this research is to study the effect of different realistic load conditions on the internal stress and strain state in the callus and to illustrate which type of complex movements may cause refracture. Although the main reason of using the fracture plate is to keep the broken parts together and enable the patient to perform the regular daily activities, it is crucial that complex movements are prevented in order to help the healing process.

Small motions exist in the interface of fracture plate and bone. When the assembly is subjected to different load conditions, the fracture plate and bone compress each other. The goal of this project is also to investigate the relative micro-motion at the bone-plate interface and regions of the stress concentration in the bone and callus.

1.1 Thesis outline

The remainder of this thesis is organized as follows:

Chapter 2 presents the required background and relevant information needed to put this research into a proper context. The chapter starts with an overview of basic bone anatomy and physiology, especially the structure of long bones with detailed references to mechanical properties of the humerus. Then, fracture mechanisms of long bones as well as fracture healing mechanisms are discussed. With this groundwork in place, the next part of the chapter presents an overview of operative and non-operative fracture fixation methods. The final part of this chapter presents a summery of the literature review and related work focusing on the finite element analysis of fracture fixation plates in order to compare the performance of various fracture plates.

Chapter 3 gives an overview of how the FEM model of bone, fracture plate and screws was generated. A problem statement is given as well as the manufacturer's specifications for the fracture plate and screws. Next, a detailed procedure of mesh generation as well as the modeling of the interfaces are provided, followed by a comprehensive review of the material selection process. Subsequently, the boundary conditions as well as the engineering constraints are discussed. This chapter concludes with a simple stress analysis of a humerus to define realistic loading conditions for the model.

Chapter 4 presents the results of the finite element analysis in terms of internal state of stress and strain under different load conditions. In addition, the results of the contact analysis at the interface of the bone and the fracture plate are included. This chapter concludes with a detailed summary of the results.

Chapter 5 presents conclusions concerning the research project and recommendations for future work.

2. Background and literature review

This chapter reviews relevant background literature, including basic bones structure, bone fracture, fracture healing, stress shielding, mechanical properties of long bones, fracture healing methods. The last sections review previous work in the area of internal fracture fixation using plates.

2.1 Basic long bone structure

Bone is a composite material consisting of collagen fibers in a mineralized matrix. Similar to other composites, the collagen fibers provide resistance to tensile loading while the mineral matrix provides excellent compressive strength (Thibodeau and Kevin, 2007).

Bone as an engineering material provides protection to various parts of the body. For instance, the brain is surrounded by a thin layer of bone called the skull (Foux et al., 1993).

There are different long bones in the body such as the long bones of the legs including the femur in the thigh, tibia and fibula in the lower leg, humerus in the upper arm, radius and ulna in the lower arm and phalanges in the hands and feet.

The long bones in the human body all share some basic structural features. These consist of a diaphysis or shaft and two epiphyses or extremities. The central region of a long bone is called the diaphysis which is the most tubular part of the bone. The diaphysis is composed of compact bone and its interior part is medullary canal which is normally filled by fatty yellow bone marrow.

The epiphyses consist of an outer covering of compact bone with cancellous bone inside and it has a tendency to transfer joint and body loads to the diaphyseal region of the bone. The diaphysis and epiphyses are separated by epiphyseal cartilage, which becomes fixed when growth is complete.

Long bones are almost completely surrounded by a vascular membrane called the periosteum which plays an important role in fracture healing since it contains dormant cells that become active in the case of a fracture.

The outer layer is fibrous and the inner layer is osteogenic containing osteoblasts (bone-forming cells) and osteoclasts (bone-destroying cells), which are involved in maintenance and remodeling of bones; it gives attachment to muscles and tendons and protects bones from injury. Hyaline cartilage replaces periosteum on the articular surfaces of bones forming synovial joints (Thibodeau and Kevin, 2007 and Hayes, 1997). Figure 2.1 illustrates the structure of a longitudinal section of a long bone.

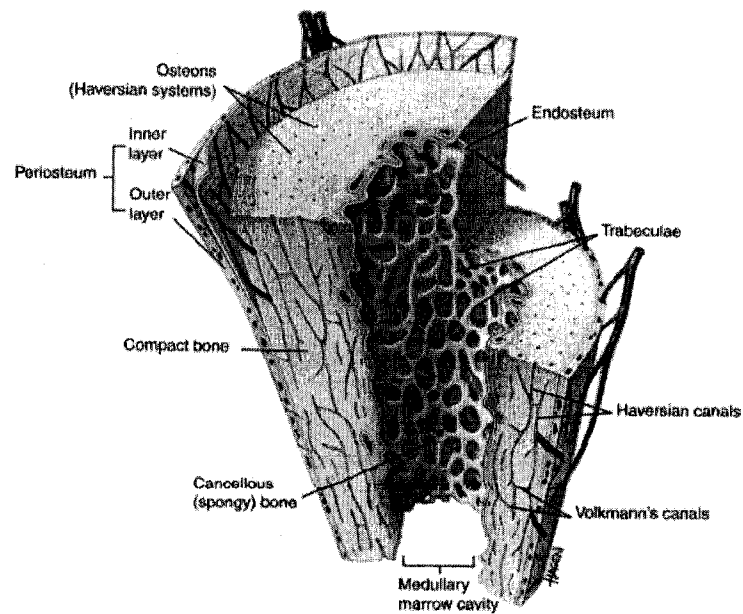


Figure 2.1: A mature long bone - partially sectioned (Thibodeau and Kevin, 2007)

2.2 Bone fracture

When a bone becomes cracked, collapses in multiple parts, or breaks into two pieces, there is a bone fracture. Additionally, certain medical conditions such as cancer, may weaken the bones so that bone fracture happens (Thibodeau and Kevin, 2007).

Fractures are categorized as closed or open and simple or multi-fragmentary. An open fracture is a broken bone that penetrates the skin. Once a broken bone sticks out of the skin, urgent surgery is most of the time required to clean the area of the fracture. In closed fractures, unlike the open fractures, skin is undamaged. Simple fractures occur along one line so that they break the bone into two parts, but multi-fragmentary fractures split the bone into multiple parts.

Generally speaking, the three principal stress planes (tensile, compressive and shear stress) indicate the fracture planes. Moreover, they can help predict when and how the material will fail. Cortical bone is generally weaker in tension and in shear particularly along the longitudinal plane. This anisotropic behavior plays an important role in influencing bone failure under external loads (Tencer and Johnson, 1994). Long bone fractures are mainly subjected to a combination of applied loads which produce a complex fracture pattern.

When a pure bending load is applied to the bone, the convex side of the bone is under tension whereas the concave part is under compression. As a matter of fact, bone is weaker in tension compared with compression so that first cracks start forming on the tension side of the bone. Once a crack starts propagating, the neutral axis of bone shifts down to the compressive side, because bone has reduced structural resistance to bending (Chao, 1997 and Hart, 1989).

Despite the fact that weight bearing long bones such as femur and tibia are usually subjected to compressive loads, it is of great interest to investigate the combined effects of both bending and axial compression.

When a bone is subjected to a purely compressive load the failure mechanism tends to be oblique cracking of the osteons.

During bending, tension on the convex side of the bone combines with the axial compression load. Therefore, a combination of two fracture processes occurs. As was mentioned formerly, a transverse crack occurs on the tensile side of the bone because of the bending load while the compressive force on the bone results in an oblique fracture. The protruding oblique surface impacts the other surface and the result is a characteristic butterfly segment which occurs on the concave side of the bone.

When a bone is subjected to a purely torsional load the result is typically a spiral fracture with the fracture line oriented at about 45° to the axis about which the torque is applied. From a purely mechanical point of view this failure of the bone is due to tensile forces that have been induced in the bone as a result of the applied torque. Since bone is stronger in compression, tensile failure occurs perpendicular to the diagonal in tension. The crack will be perpendicular to the diagonal in tension, so it will spiral at 45° to the long axis in the direction opposite to the applied torque.

2.3 Fracture healing mechanisms

One of the most distinctive features of bone is its ability to restore to its original tissue structure after injury (Salter, 1999). The focus of this study is the relationship between the mechanical and biological aspects of fracture healing. The two most general phases of the fracture healing process are the union phase and the remodeling phase.

2.3.1 The union phase of fracture healing

When the body starts to join the fractured fragments of bone together, a bridging process happens. However, bridging may happen by two separate processes, namely primary healing and secondary healing.

2.3.1.1 Primary fracture healing

Primary bone healing or primary cortical healing starts when the fracture is stable, aligned, and its surfaces are completely connected (Schatzker and Tile, 2005).

Primary fracture healing will only take place under two circumstances: The first condition is that the fractured bone must be brought back to its original anatomical configuration. The second condition is that there must be a significant decrease in inter-fragmentary strain. Both of these conditions are normally met through the use of rigid internal fracture fixation plates (Einhorn, 1998).

When the formation of fibrous tissue begins, osteoclasts on one side of the fracture area tunnel into the adjacent side of the fracture and create new haversian systems by providing pathways for the penetration by blood vessels. These tunnels are conducive to mineral salt deposits and storage which gives bone tissue its strength. Furthermore, these distinctive tunnels in bone can be easily observed using a low power microscope and are referred to as cutting cones (Einhorn, 1998).

In addition, primary term originates from the fact that bone is completely healed without the need for any intermediate or precursor cells to become involved (McKibbin, 1978). Primary healing does not see any callus formation, which affects the strength of the fixation area in several ways (Perren, 1979).

2.3.1.2 Secondary fracture healing

At the beginning, intermediate fibro-cartilage forms between the bone fragments before being remodeled into new bone. Macroscopically, secondary fracture healing is characterized by the formation of both periosteal and endosteal callus (Hayes and Mow, 1997). Callus tissue is composed of bony and cartilaginous material that forms a connecting bridge across a bone fracture during repair (McRae, 2002).

Callus formation plays an important role in providing mechanical stability to the fracture. Since the periosteal callus is on the exterior surface of the bone it effectively increases the diameter of the bone surrounding the fracture site and therefore it increases the polar moment of inertia of the bone (Hayes and Mow, 1997).

For fractures treated with non-operative methods bone follows its natural healing process which is shown in figure 2.2.

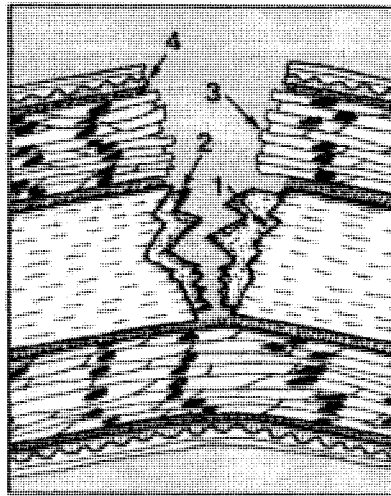


Figure 2.2: Fracture healing: fracture damages (1) – periosteum partly or completely, (2) – haversian systems, (3) – muscles and their neighboring nerves and blood vessels, and (4) skin (McRae, 2002)

There is an initial phase of bone death at the fracture site accompanied by a rapid bridging of the fracture gap with the rigid periosteal callus (figures 2.3, 2.4 and 2.5).

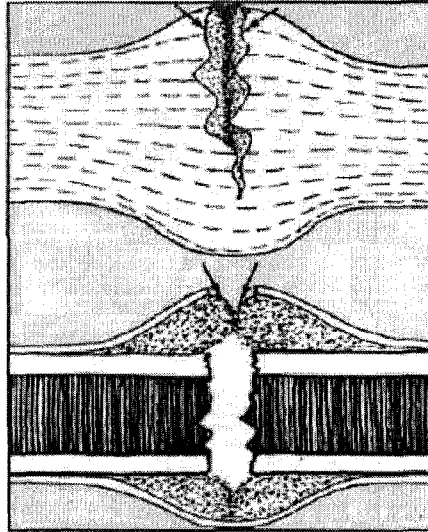


Figure 2.3: The periosteum is partially torn (McRae, 2002)

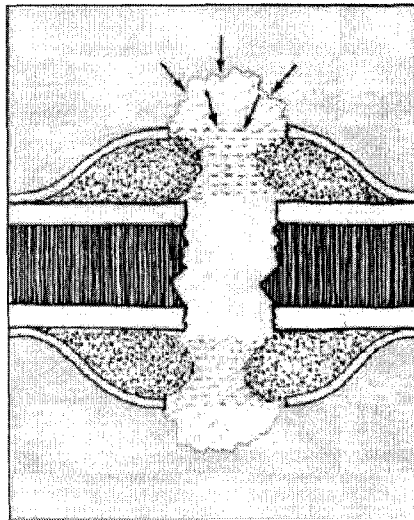


Figure 2.4: Fracture gap is bridged with a rigid callus (McRae, 2002)

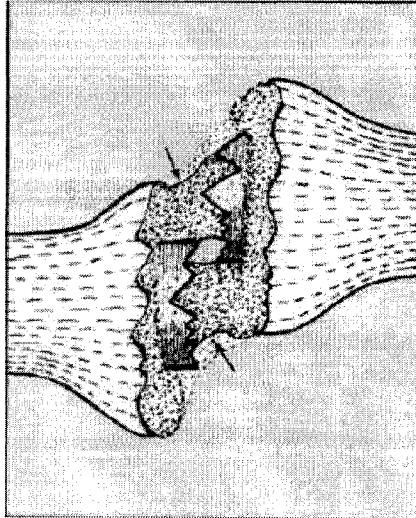


Figure 2.5: The bone ends are not aligned (McRae, 2002)

In the medullary canal, the gap at the fracture site is filled with blood and fibrous tissues (figure 2.6). As the bone heals, this is converted to woven bone. The formation of the periosteal callus is the most important aspect of non-operatively managed fractures. After this initial phase of callus formation, the remodeling phase of bone healing begins (Ferguson et al., 1996).

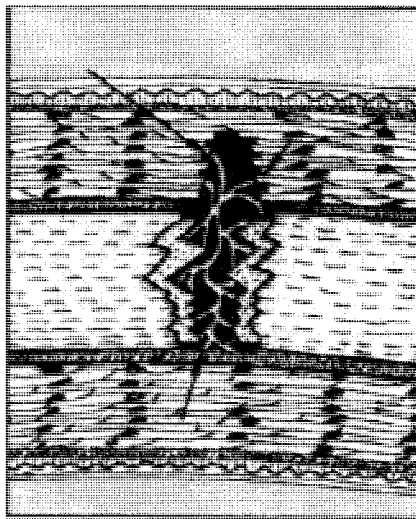


Figure 2.6: Medullary canal at fracture site fills with blood and soft tissues (McRae, 2002)

2.3.2 The remodeling phase of fracture healing

Remodeling process is transforming the newly formed temporary bone into harder and stronger cortical bone. The remodeling phase of fracture healing takes place over a long period of time. It continues until the bone returns to its original size and shape. The mechanical environment of the bone has a significant effect on the rate and amount of remodeling that occurs (McKibbin, 1978).

It is necessary to mention that the process by which bone functionally adapts, or remodels itself in response to its mechanical environment is commonly referred to as Wolff's law. It was first described by Julius Wolff in 1868 and holds that every change in the form or function of a bone is followed by adaptive changes in its internal architecture and its external shape (Cowin, 1987).

2.4 Stress shielding

Wolff's law has important implications in fracture healing, particularly when rigid internal fixation devices are employed (Cowin, 1987). In every composite system made by two materials in which one material is stiffer than the other, the stiffer material transmits the greater portion of the load. Since implants are typically made from metallic alloys which are stiffer than cortical bone, a large portion of the load bears by the fracture plate instead of transmitting by the bone. For instance, the modulus of elasticity of stainless steel is ten times greater than that of humerus, this will produce stress-shielding or stress protection effect (Cowin, 1987). In this case, a repeated fracture can occur in the same general area as where the first fracture had happened.

Wolff proposed the theory that bone will adapt itself to the applied loads. On the one hand, if the applied load increases bone will remodel to become stronger and consequently the external cortical part of the bone becomes thicker. On the other hand, if the applied load to the bone decreases remodeling process speed decreases as well, as a result bone becomes weaker. In other words, bone is deposited in areas of high stress and is reabsorbed in areas of low stress (Cordey et al., 2000).

It is shown that bone remodeling is very sensitive to stress and a change of 1 MPa, which represents less than 1% of ultimate strength of bone, in a plated femur can result in observable remodeling differences (Carter et al., 1981).

2.5 Mechanical properties of long bones

In this part, mechanical properties of long bones with major focus on mechanical properties of humerus are discussed.

Bone is a non-linear, anisotropic, non-homogeneous material with time independent viscoelastic properties. Tensile strength of compact bone is in the range of 70-140 MPa while its compressive strength is in the range of 140 - 210 MPa. On the other hand, compressive modulus of elasticity of bone is between 11 - 13 GPa whereas its tensile modulus of elasticity is between 17 -20 GPa (Tencer and Johnson, 1994). Despite the fact that in most finite element studies bone is considered as a linear isotropic material, it can be modeled either orthotropic or transversely isotropic. In this study, bone modeled as an orthotropic material. Several researchers have studied the material properties of cortical bone in human and animals. Ashman and van Buskirk (1986) used an ultrasonic technique to study the elastic properties of the human femur and human mandible. Despite the fact that the mandible is not categorized as a long bone, the data

indicate that human mandible is elastically homogenous but anisotropic. It is considered as a compact bone. It seems that the mandible is like a long bone bent into the shape of a horseshoe (Ashman and van Buskirk, 1986). The results of their study are shown in table 2.1. The 1-direction is radial, the 2-direction is circumferential and the 3-direction is axial.

Table 2.1: Average technical constants for bone (Ashman and van Buskirk, 1986)

	Femur	Mandible
E_1 (GPa)	12.0	12.8
E_2	13.4	15.6
E_3	20.0	20.1
G_{12} (GPa)	4.53	4.68
G_{13}	5.61	5.68
G_{23}	6.23	6.67
γ_{12}	0.376	0.282
γ_{13}	0.222	0.289
γ_{23}	0.235	0.265
γ_{21}	0.422	0.366
γ_{32}	0.371	0.454
γ_{31}	0.350	0.341

Various researchers (Ferguson, 1996, Lawrence, 2000 and Ramakrishna, 2004) have considered bone as a transverse isotropic material and the material properties assigned are shown in table 2.2.

Table 2.2: Material properties of cortical bone (Ramakrishna et al., 2004)

Cortical Bone	
E_1 (GPa)	14.5
E_2	14.5
E_3	19.7
G_{12} (GPa)	7.0
G_{13}	7.0
G_{23}	5.28
γ_{12}	0.285
γ_{13}	0.285
γ_{23}	0.265

Zadpoor (2005) has conducted a study on human hand arm vibrations, especially the humerus, using a finite element method. He has considered the humerus as an isotropic material. Mechanical properties of compact bone which are used by Zadpoor are shown in table 2.3. Reported Young's modulus varies between 8 MPa and 30 MPa.

Table 2.3: Young's modulus and Poisson's ratio of the humerus (Zadpoor, 2005)

Humerus	
E (GPa)	17.2
γ	0.3

Lovald et al. (2006) compared different plate-screw systems used in mandibular fracture reduction using finite element analysis. Material properties used in this study are shown in table 2.4.

Table 2.4: Material properties used in finite element analysis (Lovald et al., 2006)

Material properties	Young's modulus (GPa)	Poisson's ratio
Cortical bone	13.7	0.30
Cancellous bone	7.93	0.30
Dentin	17.6	0.34
Titanium plate and screws	110	0.34

As is already mentioned, most of the finite element analyses have considered cortical bone as an isotropic homogeneous medium. A better approximation of bone is to consider it an orthotropic linear elastic solid governed by Hooke's law. Ionescu et al. (2003) have compared several orthotropic finite element models of the whole tibia. Table 2.5 represents the material properties of cortical bone of a human tibia.

Table 2.5: Material properties of human tibia (Ionescu et al., 2003)

Cortical Bone	
E_1 (GPa)	6.91
E_2	8.51
E_3	18.4
G_{12} (GPa)	2.41
G_{13}	3.56
G_{23}	4.91
γ_{12}	0.49
γ_{13}	0.12
γ_{23}	0.14

Lin et al. (2006) have investigated the interactions of plate fixation angles in the internal double plating of distal radius in conjunction with various loading conditions using non-linear finite element analysis. Table 2.6 shows material properties of cortical bone.

Table 2.6: Material properties of cortical bone (Lin et al., 2006)

Cortical Bone	
E (GPa)	17
γ	0.3

Clavert et al. (2006) designed an accurate 3D digital model of the humerus and rotator cuff muscles. Then, they used this model to study strain distribution in humeral tubercles according to bone density. The material properties which they used in their work represented in table 2.7.

Table 2.7: Material properties of young and old cortical bone (Clavert et al., 2006)

Cortical bone		
	Young bone	Old bone
E (GPa)	16	12
γ	0.3	0.3

Table 2.8 summarizes the above mentioned material properties of compact bones.

Table 2.8: Summary of different material properties

	Bone	Young's Modulus (GPa)	Shear Modulus (GPa)	Poisson's ratio
Ashman et al. (1986)	Femur	$E_1 = 12.0$ $E_2 = 13.4$ $E_3 = 20.0$	$G_{12} = 4.53$ $G_{13} = 5.61$ $G_{23} = 6.23$	$\gamma_{12} = 0.376$ $\gamma_{13} = 0.222$ $\gamma_{23} = 0.235$ $\gamma_{21} = 0.422$ $\gamma_{32} = 0.371$ $\gamma_{31} = 0.350$
	Mandible	$E_1 = 12.8$ $E_2 = 15.6$ $E_3 = 20.1$	$G_{12} = 4.68$ $G_{13} = 5.68$ $G_{23} = 6.67$	$\gamma_{12} = 0.282$ $\gamma_{13} = 0.289$ $\gamma_{23} = 0.265$ $\gamma_{21} = 0.366$ $\gamma_{32} = 0.454$ $\gamma_{31} = 0.341$
Ramakrishna et al. (2004)	Cortical Bone	$E_1 = 14.5$ $E_2 = 14.5$ $E_3 = 19.7$	$G_{12} = 7.0$ $G_{13} = 7.0$ $G_{23} = 5.28$	$\gamma_{12} = 0.285$ $\gamma_{13} = 0.285$ $\gamma_{23} = 0.265$
Zadpoor (2005)	Humerus	$E = 17.2$		$\gamma = 0.3$
Lovald et al. (2006)	Cortical Bone	$E = 13.7$		$\gamma = 0.3$
Ionescu et al. (2003)	Cortical Bone	$E_1 = 6.91$ $E_2 = 8.51$ $E_3 = 18.4$	$G_{12} = 2.41$ $G_{13} = 3.56$ $G_{23} = 4.91$	$\gamma_{12} = 0.49$ $\gamma_{13} = 0.12$ $\gamma_{23} = 0.14$
Lin et al. (2006)	Cortical Bone	$E = 17$		$\gamma = 0.3$
Clavert et al. (2006)	Cortical Bone (Young)	$E = 16$		$\gamma = 0.3$
	Cortical Bone (Old)	$E = 12$		$\gamma = 0.3$

2.6 Fracture fixation methods

Fracture fixation methods are divided into non-operative methods and operative methods.

2.6.1 Non-operative methods

In this method, there is no need to do surgery on the broken bone.

2.6.1.1 Cast immobilization

In most cases, a broken bone can heal successfully once the broken ends have been aligned and the ends of the broken bone are in adequate connection. In this case, a plaster or fiberglass cast keeps the broken ends in the appropriate position while they heal.

Figure 2.7 shows a long arm plaster used to immobilize the humerus. In this case, weight of the plaster and also weight of limb reduce the fracture and keep the humerus aligned.

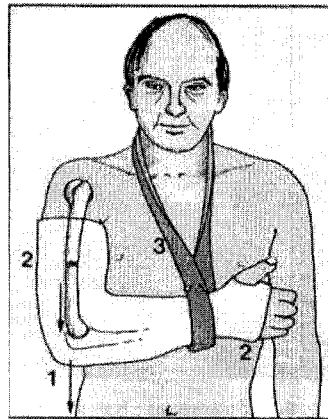


Figure 2.7: (1) bone reduction, (2) long arm plaster and (3) collar and cuff sling (McRae, 2002)

2.6.1.2 Traction

Alignment of the bone by a gentle and steady pulling force is called traction. Traction force normally transfers to the bone through different pulleys or a metal pin. As a matter of fact, traction is one of the preliminary methods of fracture treatment. Figure 2.8 shows the traction for a broken femur. The weights transfer through the cord and pulleys to the splint. It is necessary to mention that the Thomas Splint is a long leg splint,

allowing traction to a fractured leg. In addition, it extends from a ring at the hip joint to beyond the foot.

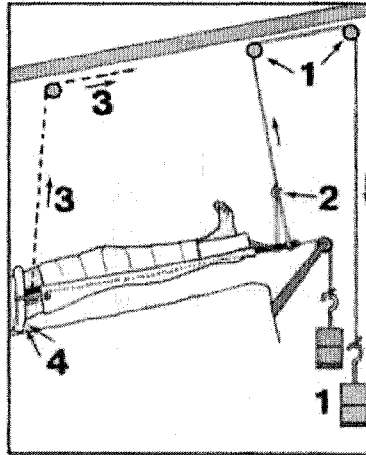


Figure 2.8: (1) Weights and pulley system, (2) traction cord, (3) support for the proximal end of the splint, and (4) Thomas Splint ring (McRae, 2002)

2.6.2 Operative methods

In this type of treatment, surgery must be performed on the broken bone. During the surgery, the bone fragments are put back to their normal position, aligned, and then held together with special devices such as wires, pins, plates, intermedullary nails and screws.

2.6.2.1 Wires and pins

Wires and pins are usually used in combination with other types of internal fixation devices to stick the bones together. In addition, they can also be utilized alone to treat fractures of small bones such as the small bones in hand. Figure 2.9 shows the lateral condylar fracture which is held by two k-wires in its position.

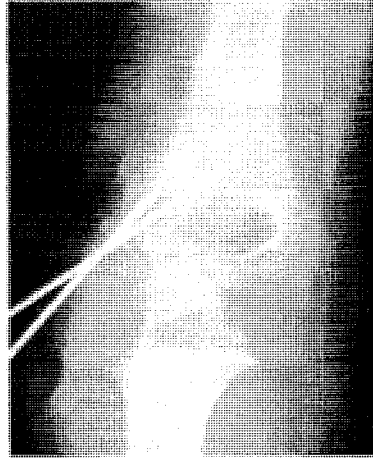


**Figure 2.9: Lateral condylar fracture which is held by two k-wires in its position
(McRae, 2002)**

2.6.2.2 Plates

Plates are internal supports that hold the fractured ends of the bone together. Plates are normally extended along the bone and fixed by screws to the bone. The number of screws depends on different factors such as the position of the broken bone, number of the plate holes, etc. However, it is necessary to mention that if two bones are parallel to each other both break, such as in the forearm, plating one bone may provide enough support for the other bone. After healing is complete, the plate may be left in the body or removed. Internal fixation plates are normally used when the surgeon decides that they are the best method to restore the bone into its normal function immediately, without the need for a possibly long hospital stay.

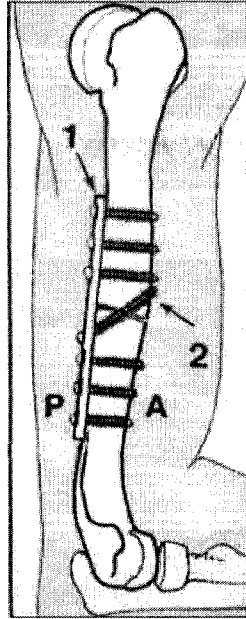


Figure 2.10: Mid-shaft fracture of humerus (1) fracture fixation plate, (2) screws (McRae, 2002)

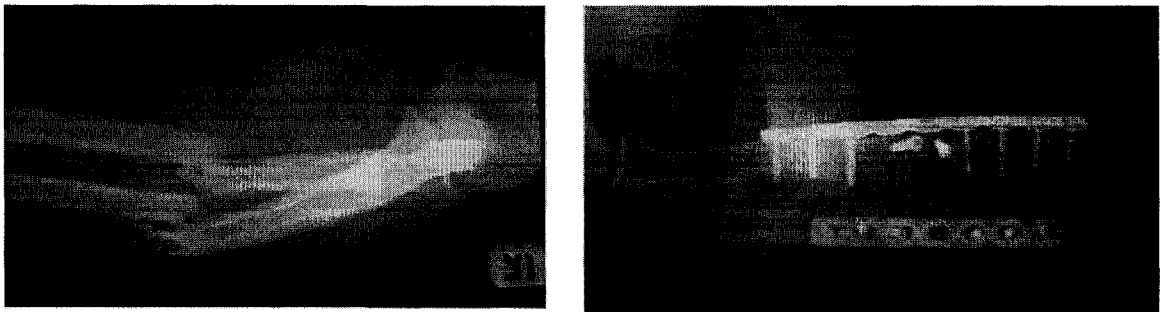


Figure 2.11: Forearm fractures and fracture fixation plates (Saidpour, 2006)

2.6.2.3 Intermedullary nails or rods

In the case of a long bone fracture another way to align the broken bone is to use an intermedullary nail. Generally speaking, long bones are in the form a hollow cylinder which is filled by some yellow marrow. An intermedullary nail is inserted into the medullary canal and keeps the bone aligned. This nail is kept in the bone until the fracture has healed and removed after healing. However, sometimes it is decided to leave

the nail in place. Figure 2.12 shows a humerus proximal fracture which is treated by an intermedullary nail with proximal and distal cross bolting.

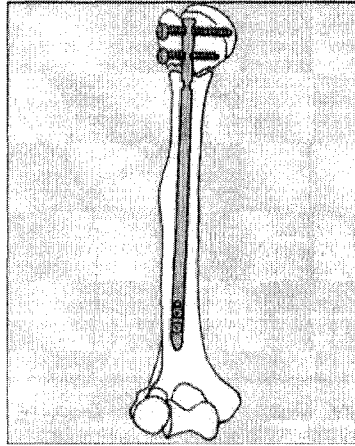


Figure 2.12: Proximal fracture of humerus which is fixed by intermedullary nail with proximal and distal bolting (McRae, 2002)

2.6.2.4 Screws

Although screws have simple shapes, there are several screw designs based on the specific usage of the screws. Figure 2.13 shows a humerus with multiple proximal fractures which are treated using a cancellous screw and a tension band.

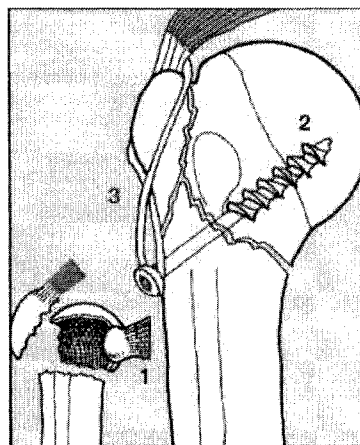


Figure 2.13: Humerus three-part fractures, (1) articular surface, (2) cancellous screw, and (3) tension band (McRae, 2002)

Figure 2.14 shows a cortical and a cancellous screw.



Figure 2.14: Left: 4.5mm diameter cortical screw, Right: 3.5mm diameter cancellous screw (Fazzini)

2.6.2.5 External fixation

In external fixation, pins or screws are put into the broken bone on both sides of the fracture site. After repositioning the bone fragments by the orthopedic surgeon, pins or screws are connected to clamps or metal bars outside the skin. This device stabilizes the bones in the appropriate position so that they can heal. The external fixation device would be removed after a certain amount of time. Figure 2.15 shows a fractured tibia which is fixed by an external fixator.

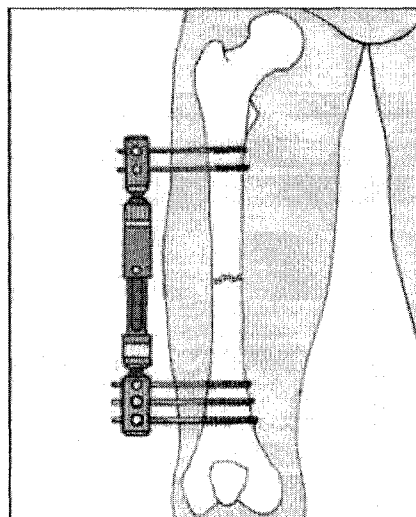


Figure 2.15: A broken femur which is treated by an external fixator (McRae, 2002)

2.7 Finite element analysis of fracture fixation

In simple terms, the finite element method can be described as a technique for obtaining the solution to a complex problem by subdividing it into a collection of smaller and simpler problems that can be solved using numerical techniques. An approximate solution to the original complex is then found based on the combined solutions from the simple sub-problems (Cowin, 1989). The complex geometry of the bone in combination with fixation plates, material properties, boundary conditions and information regarding stress distribution in the assembly makes it complicated to find a precise solution for most of engineering problems. Implementation of finite element modeling in the field of orthopedics is an important tool for design and analysis. As is mentioned before, in this method, a mathematical model is created that integrates the mechanical and structural properties of the material and then solved for stresses and strains using advanced numerical techniques. This method is ideal because the computer model overcomes many of the limitations of laboratory studies. Full stress distributions can be obtained at any desired point in the model. On top of that, a model can be tested under different load conditions, material properties and also boundary conditions. Finally, the model can be analyzed several times without the concern of the development of a stress history.

In the finite element process, the geometry of the model is first defined and a mathematical model of the structure is formed by dividing the entire model into a finite number of elements. The geometry of the element is represented by the coordinates of its corner points or nodes, with a shape function or interpolation function describing the shape of the edges between nodes. The stiffness of each element is calculated numerically and is dependant on the shape and material behavior of that element. The stiffness matrix

which relates the displacement at each node to the forces acting on the element then is combined to form a global stiffness matrix for the structure. The boundary conditions which are applied to the model in the form of forces and displacement are then substituted into the problem and the problem is solved for the unknown displacements. Nodal stresses and strains then are calculated from nodal displacements. The accuracy of the representation of the load response is dependant on many factors such as the refinement of the element mesh, the material definitions, and assumptions made in loading and boundary conditions.

A various number of element types that differ in their number of nodal points, shape, and dimensional criteria are available to make the model. For simple models, 2D elements are often used while it would be of great interest to use 3D elements for more complicated models such as bone. In that case, a more accurate result which depends on the geometry of the model is obtainable.

Hayes et al. (1979) created an axisymmetric model of the normal proximal tibia loaded to simulate weight-bearing. This model predicted maximum compressive stresses beneath the center of the loading region and maximum shear stresses beneath the edge of the loading region. In addition, the lines of stress were oriented along the axes of the trabeculae.

Hipp et al. (1990) created a 3D finite element model to investigate the structural consequences of transcortical holes through long bones loaded in torsion. They determined that defects with a hole to bone ratio of less than 0.1 have little effect on the strength of the bone, but for a ratio of 0.2, the strength is reduced by 20%. In addition, the cortical wall thickness had a significant effect on strength reductions.

Several finite element analyses have been done to study the effects of fixation plates on bone remodeling. Rybicki and Simonen (1977) created a 2D model of an obliquely fractured bone fixated with a plate in order to study the effect of tension in the plate, the effects of placing bone screws at different angles to the plane of the fracture, and the effect of a uniform end loading to represent weight bearing on the assembly. Results of the model indicated that the stress distributions at the fracture surface were not uniform. This study also showed that stress shielding happened underneath the plate and as a result, the effects of plate and screws extended beyond the ends of the plate.

Firoozbakhsh et al. (1992) created a mathematical model using orthotropic bone properties to study the effects of screw holes on bone remodeling. In this model, the bone remodeling rate was dependant on the volume fraction of adaptive bone, stress field and bone strain. Results showed local compressive stress concentrations lead to bone deposition and local tensile stress concentration lead to bone resorption.

Simon et al. (1977) developed 1D, 2D, 3D models of a 6-hole Ti-6Al-4V plate fixed to a sample human femur created using an aluminum tube with the same bending stiffness. The models were tested in bending and axial compression with bench tests with an identical setup. Results of this study indicated that 1D and 2D models were accurate in regions sufficiently distant from the complex geometry of the plate and screw, but it could only provide a qualitative approximation of the gross behavior of the assembly. This study also showed that a 3D model should be used to obtain information about the stresses around the screw regions and 1D and 2D models should only be used for general stress analysis.

Beaupre et al. (1984) created a 3D model of a plated bone to determine the effects of screw tightness and interface slipping on the stresses in the bone. They determined that screw tightness plays an important role in the relationship between loading and resulting strain. Additionally, they found that disregarding the slippage that occurs between plate and bone physiologic load levels can lead to over prediction of stress shielding. The same model was used to determine the neutral axis shift for plate application and the positions of highest stress in the model.

Ramakrishna et al. (2004) have worked on enhancing bone healing with reduced stress shielding. In this matter, they first represented an analytical solution to determine screw forces in the bone plate assembly under the bending load. Subsequently, they have conducted their research on a non-homogeneous stiffness graded (SG) plate instead of a homogeneous regular stainless steel (SS) plate. Table 2.9 shows the results of analytical solution for a plate reinforced bone model.

**Table 2.9: Design parameters of bone plate and calculated stress values
(Ramakrishna et al., 2004)**

Plate Material	Modulus of Plate (GPa)	Thickness of plate (mm)	Bending Stiffness EI (10^5 Nmm ²)	Stress at fracture site underneath the plate (N/mm ²)	Stress away from second screw and underneath the plate (N/mm ²)
316L Stainless steel	210	2	21.0	0.6780	3.110
		3	70.9	-0.0301	2.004
		4	168.0	-0.1199	1.250
		5	328.1	-0.1051	0.825
Ti-6Al-4V	110	2	11.0	1.4320	3.500
		3	37.1	0.2351	2.695
		4	88.0	-0.0818	1.900
		5	171.8	-0.1327	1.346
CFRP	50	2	5.0	2.4900	3.827
		3	16.8	0.9400	3.352
		4	40.0	0.1974	2.732
		5	78.1	0.0666	2.156

When a beam is subjected to a bending moment, as shown in figure 2.16, the material above the neutral axis is subjected to tensile stress and the material below the neutral axis bears compressive stresses. Based on Gautier et al. (2000) the bone-plate is fixed on the tension side of a fractured bone.

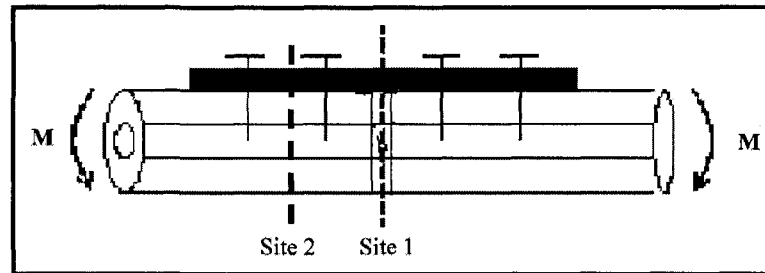


**Figure 2.16: Plate reinforced bone system under pure bending
(Ramakrishna et al., 2004)**

From Table 2.9, it is evident, for stainless steel plate, to have neutral axis inside the plate at site 1, and maximum tensile stress in the top layer of the bone at site 2, the thickness of the plate should be at least 3 mm. Similarly, in a Ti-6Al-4V plate, the plate thickness should be 4 mm. However, for the modulus of plate to be less than 50 GPa, the neutral axis is shifted into the bone and therefore causes some tensile stress in the upper layer of bone, site 1, leading to delayed healing. Hence, the optimal plate should have modulus of elasticity of 210 GPa and thickness of 3 or 4 mm for the cases considered.

Ramakrishna et al. (2004) applied a bending moment of 500 Nm through four point bending. According to them, generally, a 150-200 Nm bending moment is applied to the bone, essentially tibia, in normal gait and this reaches a maximum of 500-600 Nm during running or accidental loads that will cause failure of the fracture fixation.

Their results of the finite element analysis illustrated that using a stiffness graded plate is useful to eliminate the effect of stress shielding in bone fracture fixation

treatment. Additionally, their study showed that implementation of stiffness graded plates enhances the bone healing process compared to the regular stainless steel plates.

Saidpour (2006) conducted a finite element analysis on a novel forearm internal fixation plate made from short carbon fiber reinforced thermoplastic (CFRP) composite material. This study analyzed the stress distribution in the composite plates. Saidpour designed a new plate with a unique geometry and finite element analysis was performed to examine the mechanical performance of different six-hole fracture plate designs under two different loading conditions, bending and torsion. These plates were assumed to have isotropic properties with short carbon fiber reinforced thermoplastic (CFRP) composite materials.

To utilize the full potential of CFRP composites initially a plate was designed which consisted of straight parallel edges.

On the other hand, to provide more movement at the point of bone fracture as a control, a second fracture plate was designed with a reduced waist in the middle. However, the relatively sharp corners in the waisted design (the control case) resulted in higher stress concentration. Figure 2.17 is the final shape of the plate which is optimized in the design by varying the breadth in the waist region from 8 mm to 12 mm in a non-linear fashion, to reduce the stress concentration in the region.

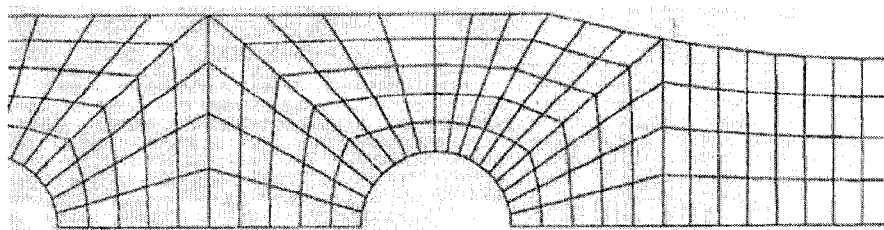


Figure 2.17: Part of a waisted fracture plate (Saidpour, 2006)

Two different load conditions were used to analyze the stress concentration in the two different designs. A load of 800 N applied at the plate end with the plate fixed across the middle section to generate bending moment at the other end. The second loading condition was a twisting moment of 2.8 Nm which was applied to each of the first three screw holes at one end, about the neutral axis of the plate cross section, with half of the plate restrained at the opposite three screw-hole locations. A uniform pressure of 19 kN/m² applied to the top of the screw holes in order to simulate the effect of screw head locking into the holes.

Results showed that for the straight edge model, the maximum stress is 553 MPa which is in the innermost screw holes while for the waisted edge model, the maximum stress is 641 MPa which is around the middle of the span (figure 2.18).

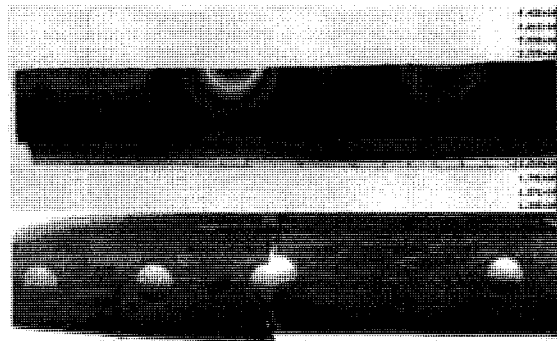


Figure 2.18: Fracture plate under flexural loading. Top: FEA, Bottom: Destructive test (Saidpour, 2006)

For the waisted edge model, next highest stress is 225 MPa which is around the inner screw holes (figure 2.19)

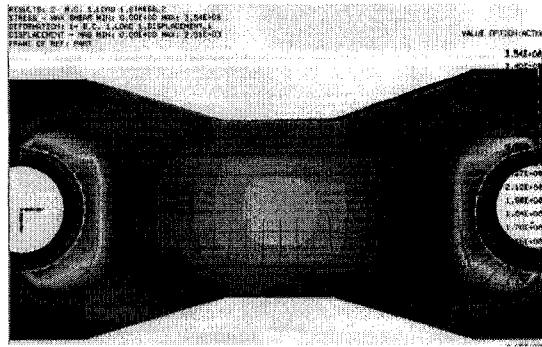


Figure 2.19: Von-Mises stress distribution in waisted fracture plate models loaded in torsion (Saidpour, 2006)

Similar trend was also presented for torsional load case; therefore, the inner screw-hole regions are the most likely areas for plate failure (figure 2.20). Preliminary destructive tests on the fracture plates have confirmed these findings.

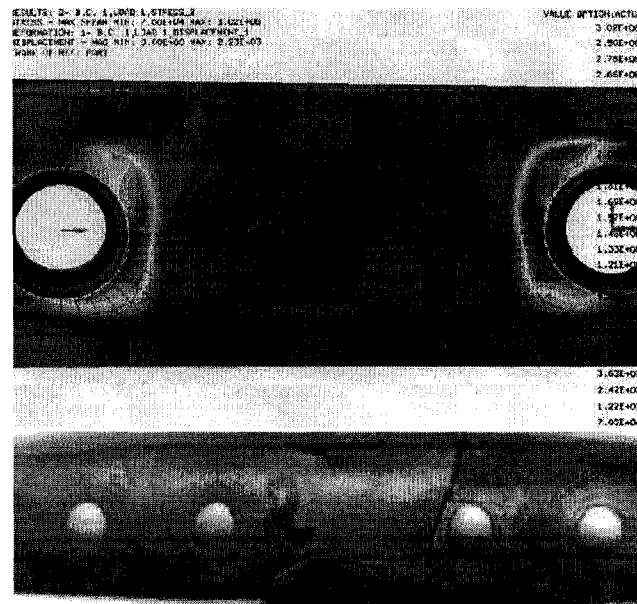


Figure 2.20: Fracture plate under torsional load. Top: FEA, Bottom: Destructive test (Saidpour, 2006)

Gómez-Benito et al. (2006) studied the callus. They assumed this to be isotropic and homogeneous. The material properties of the callus can be approximated as a percentage

of healing, with the greatest deformation occurring with the least healing which is almost 1% of healthy bone properties. Table 2.10 represents the material properties of a compact bone at different stages of healing.

**Table 2.10: Material properties of callus at different stages of healing
(Gómez-Benito et al., 2006)**

Percentage of healing	Young's modulus (GPa)
1% (1 st week of healing)	0.02
50% (3 rd week of healing)	10
75% (6 th week of healing)	15
100% (8 th week of healing)	20

Different researchers have conducted studies on the stress distribution in bone fracture plates to measure the stress concentration in screws and plate regarding the stress shielding phenomenon. Ganesh et al. (2005) proposed to use stiffness graded plates to address this problem. They used ANSYS to compute the stress distribution in the fractured bone. Afterward, they compared the results with a regular stainless steel plate. They assumed that the bone is isotropic.

Results of finite element analysis for stainless steel (SS), stainless graded in thickness (SGT) and stiffness graded in length (SGL) plates are shown in table 2.11.

Table 2.11: Stress variation at the bone fracture-interface for SS, SGT and SGL plate fixations at different stages of bone healing (based on Ganesh et al., 2005)

Plates	Position of neutral Axis		Reason
SS	1st week (1% healing)	In the middle of the plate	The loading bearing cross-section at the fracture interface consists only of the plate
	3rd week (50% healing)	Shifts down into the bone-plate interface	Some callus develops at the fractured interface
	6th week (75% healing)	Shifts into the bone domain	There is more callus consolidation, the modulus of the laid-over bone at fractured interface increases considerably
SGT	1st week (1% healing)	In the middle of the plate	Same as SS plate
	3rd week (50% healing)	The neutral axis shifts down into the bone-plate interface, but a little bit more than SS and SGL plates (~1 mm from bone and plate interface). Therefore, the SGT plate stress shields the bone a little less than the SGL plate, and allows tensile stress in the bone layer underneath the plate.	
	6th week (75% healing)	The neutral axis has moved a bit into the bone (~2 mm from bone and plate interface)	
SGL	1st week (1% healing)	In the middle of the plate	Same as SS plate
	3rd week (50% healing)	Still located inside the plate and continues to stress shield the bone	Some callus develops at the fractured interface
	6th week (75% healing)	The neutral axis has moved a bit into the bone (~1 mm from bone and plate interface)	

From table 2.11 it is evident that stiffness graded plates (both SGT and SGL) provide less stress shielding than SS plate. At the fracture site, the SS plate continues to shield the bone from tensile stress, whereas SGT and SGL plates allow the bone to take on some tensile stress. Once the callus is mature (at 50% healing), tensile stress at this stage of healing is beneficial for enhanced callus formation. Away from the fracture site, SGT and SGL plates allow the bone to take on more tensile stress compared to the SS plate; therefore allowing the bone to retain its tensile strength properties.

Table 2.12 presents the magnitude of stress at different points. The positive sign indicates a tensile stress while the negative sign represents a compressive stress.

Table 2.12: Magnitude of stresses in the fracture plate during the 50% of healing (Ganesh et al., 2005)

Plate type	Top layer of the bone		Bottom layer of the bone	
	Stresses at fracture site (MPa)	Stresses at 20mm away from fracture site (MPa)	Stresses at fracture site (MPa)	Stresses at 20mm away from fracture site (MPa)
SS	-2.0	-0.2	-10	-15
SGT	2.0	4.0	-13	-19
SGL	1.0	6.0	-12	-21

Lovald et al. (2006) compared four plate-screw systems used in mandibular fracture reduction using finite element analysis. The fracture plate configurations are depicted in figure 2.21.

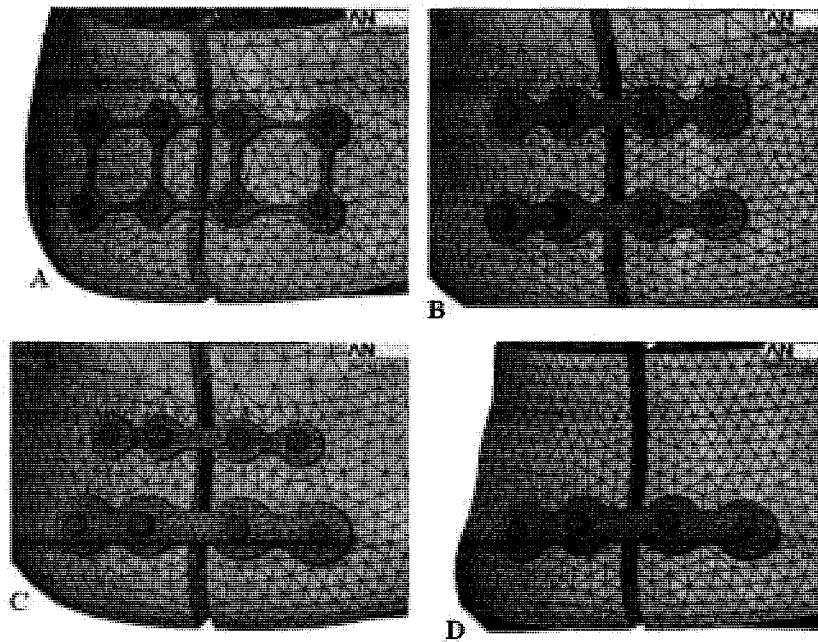


Figure 2.21: Titanium plate configurations used for stress analyses: A: ladder type plate, B: two small plates, C: large/small plates, and D: large plate

This study showed that all plate configurations can be used, depending on the severity of the fracture. Ladder configuration A is ideal due to its flexibility. Large/small plates configuration C showed an advantage in having somewhat smaller stresses and better immobilization, which would make it a good candidate for comminuted fractures (fractures in which bone is crushed into a number of pieces). Large plate configuration D is not suggested for comminuted fractures due to the large separation along the fracture plates.

Lin et al. (2006) investigated the interactions of plate fixation angles in the internal double plating of a distal radius in conjunction with various loading conditions using non-linear finite element analysis with ANSYS. The aim of the study was to investigate the biomechanical interactions of the column angles between two buttressed plates under axial, bending and torsional load conditions using non-linear finite elements stress analysis.

To perform the double-plating fixation method for a distal radius fracture, a 1 mm extra-articular fracture gap, 25 mm from the distal end of the radius was created using an idealized planar cut. Figure 2.22 represents the solid model and fracture plates set-up.

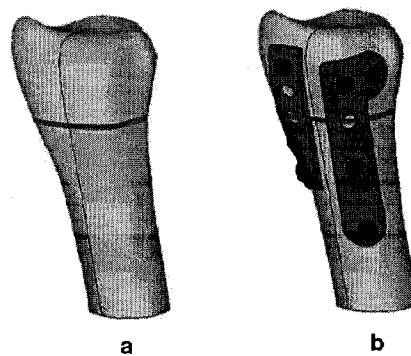


Figure 2.22: a) a solid model of the distal radius, b) L-plate and straight plate profiles (Lin et al, 2006)

Quadratic tetrahedral elements (Solid92) were used to mesh the model. An axial load of 100 N, bending load of 1 Nm and also torsional load of 1 Nm were applied to the center of the articular surface. Cortical bone as well as cancellous bone were considered as a homogeneous elastic linear material. To simulate a more realistic interfacial condition, assumptions about the fixation plate and bone surface were made, and non-linear frictional contact elements (Conta49) were used to generate the frictional condition between different components. It is assumed that the coefficient of friction is 0.3 for all contact surfaces.

Figure 2.23 shows their finite element mesh model with 90° between two buttressed plates and three load conditions applied in the study.

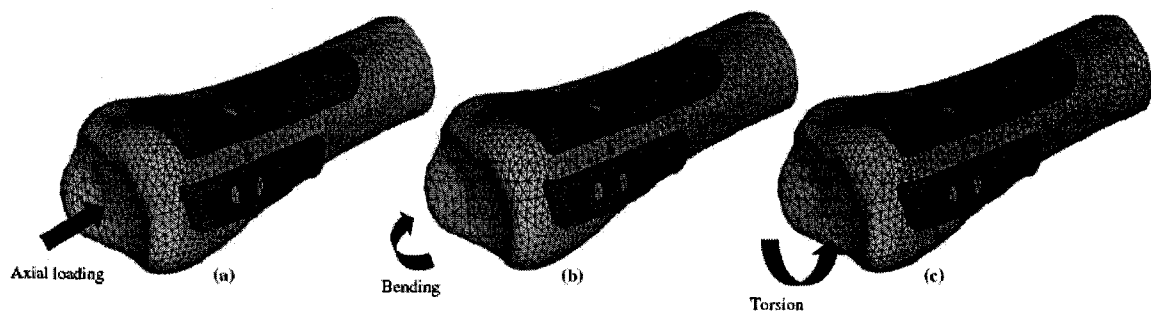


Figure 2.23: a) axial load, b) bending moment, c) torsion (Lin et al, 2006)

The maximum von-Mises stress for axial, bending and torsion load in distal radius, L-plate and straight plate are shown in table 2.13.

Table 2.13: Maximum equivalent von-Mises stress for the bone under different load conditions

	Degree between plates	Axial (MPa)	Bending (MPa)	Torsion (MPa)
Distal radius	50°	90	200	180
	70°	80	200	160
	90°	20	100	110
L-plate	50°	450	605	630
	70°	380	610	605
	90°	240	620	495
Straight plate	50°	215	320	545
	70°	180	295	525
	90°	150	260	300

The displacements at the radius end for all simulated models are represented in table 2.14.

Table 2.14: Displacement at the radius end of the model

	Degree between plates	Axial (mm)	Bending (mm)	Torsion (mm)
Distal radius	50°	0.6	0.88	1.62
	70°	0.45	0.85	1.21
	90°	0.3	0.84	0.65

The approximate maximum strain values on the healing fracture interface for all simulated models are represented in table 2.15.

Table 2.15: The approximate maximum strain on the healing fracture interface

	Degree between plates	Axial	Bending	Torsion
Distal radius	50°	250	298	460
	70°	190	300	410
	90°	80	301	345

Lin et al. (2006) used linear elastic (homogeneous and isotropic) characterization of the bone and plate screw system to simplify the numerical convergence considerations. Both the separation angles and load conditions affected the stress value and stress distribution significantly. Bending and torsion significantly increased the stress values more than the axial load. The radius bone and fixation plate stress values, the displacements at the radius end and strains at the fracture healing interface indicated that increased plate fixation angles could provide better mechanical strength to establish favorable stress transmission and prevent distal fragment dislocation.

3. Development of the finite element model

The main goal of this chapter is to create a finite element model of the bone, fracture plate and screws in order to subject the assembly to various loading conditions. The bone, a humerus, is modeled based on the information taken from Van Dongen (1963) as well as its material properties taken from various studies based on the discussion in chapter two while the approximate dimensions of the fracture plate and screws are taken from their manufacturers. Next, a detailed procedure of mesh generation as well as the modeling of the interfaces are provided, followed by a comprehensive review of the material selection process. Subsequently, the boundary conditions as well as the engineering constraints are discussed. This chapter concludes with an elementary stress analysis of the humerus to define realistic loading conditions for the model. It is necessary to mention that the model had to be designed in the way that allows us to conduct the analysis for different load conditions and also for the changing material properties of the various components.

3.1 Bone model

To create a realistic model of humerus it is necessary to establish normal geometry for the human humerus. The academic version of ANSYS 11.0 is used to create a half symmetry 3D finite element model with symmetry taken around the long axis of the bone. In order to simplify the geometry of the bone and to minimize the computational time, the shaft of the humerus was approximated by a hollow cylinder (Cowin, 1989). Van Dongen (1963) provided morphological and metrical description of

the Australian aboriginal humerus. Descriptive dimensions for the male and female aboriginal humerus are represented in table 3.1.

**Table 3.1: Dimensions of male and female aboriginal humerus (mm)
(Van Dongen, 1963)**

	n	\bar{X}	SD
Left humerus maximum length			
Male	195	323.9	16.22
Female	147	303.5	16.05
Left humerus maximum mid-shaft breadth			
Male	95	19.8	1.72
Female	101	17.1	1.60
Left humerus minimum mid-shaft breadth			
Male	92	15.6	1.49
Female	73	12.8	1.29
Left humerus vertical head diameter			
Male	89	41.6	2.36
Female	88	36.5	2.12
Left humerus distal articular surface breadth			
Male	59	42.0	2.33
Female	73	37.3	2.21

Since the finite element analysis is carried out on the mid-shaft humerus, the average male and female left humerus maximum mid-shaft breadth is considered as the diameter of the bone in the finite element model. Therefore, the inner and outer diameters of the humerus were considered to be 9.5 mm and 18.5 mm respectively. The fracture is considered perpendicular to the shaft and in the mid-shaft of the humerus. The fracture gap in this study was 1 mm.

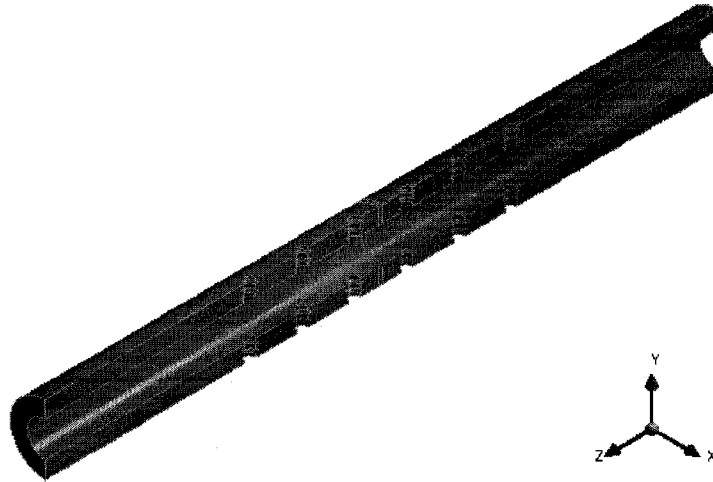


Figure 3.1: Finite element model of the humerus

3.2 Fracture plate model

The plate used in this study is a 6-hole collinear narrow fracture fixation plate with equal spacing between the centers of the holes and the centers of holes in a straight line. The plate is modeled as a bar, with a curved bottom and a flat top. The interior part of the plate which is in contact with the exterior part of the bone is formed in the shape of the bone. The plate measures 9 cm in length and 10 mm in width. The thickness varies from 3 mm in the middle to 4 mm at the edge of the plate. The screw holes are 4.5 mm in diameter and they are placed 14 mm apart.

Figure 3.2 shows a picture of an actual fracture plate and figure 3.3 shows the plate model which was generated by ANSYS 11.0.

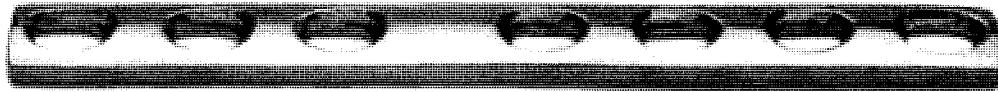


Figure 3.2: Fracture fixation plate (Narang Medical Limited)

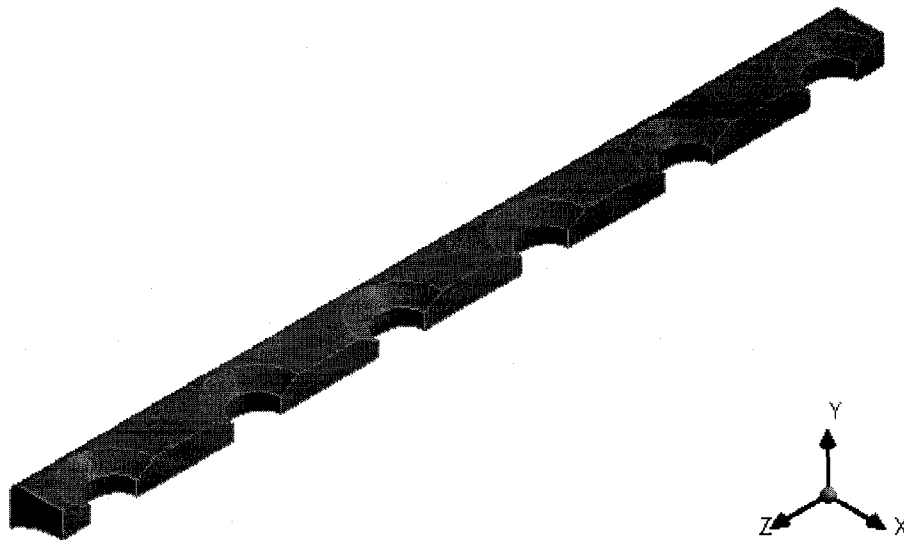


Figure 3.3: Finite element model of the fracture plate

3.3 Screw model

The screws used in the model are 4.5 mm cortical screws. The cortical screw thread diameter is 4.5 mm while its core diameter is 3 mm. The screw head diameter is 8 mm. In order to simplify the geometry and also reduce the calculation time only four threads, two on the upper side and two on the lower side of the screw, were modeled.

The screws pass through the plate and screw heads are in contact with the inside surfaces of plates screw slots. Figure 3.4 shows the real screw and figure 3.5 represents the generated model with ANSYS 11.0.

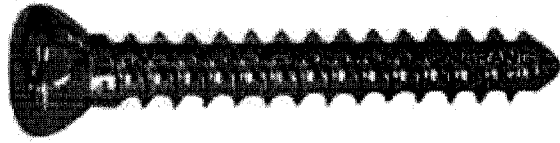


Figure 3.4: Cortical Screw (Fazzini)

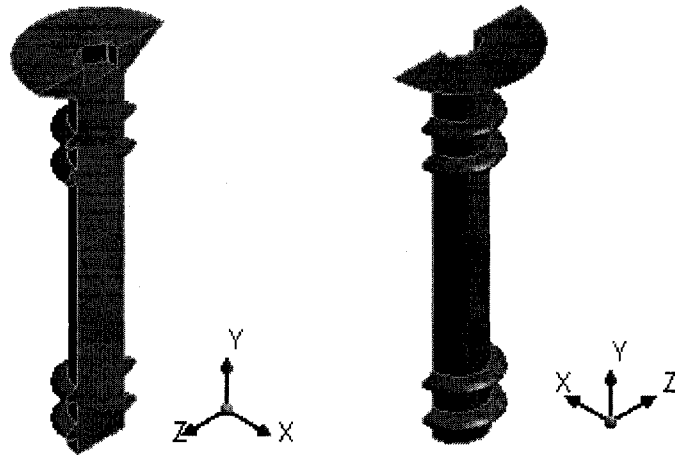


Figure 3.5: Finite element model of the screw

3.4 Mesh generation

ANSYS Workbench 11.0 has an automatic built-in mesh generation package so-called FE Static Structural. This package enables us to generate mesh for a complex 3D structure and also to refine the mesh in specific regions if there is a need for more accuracy such as the fracture gap. Three different elements are used to generate the mesh for the solid parts, namely 10-node quadratic tetrahedron, 20-node quadratic hexahedron

and 20-node quadratic pyramid elements. The following section represents the procedure of mesh generation for the assembly.

3.4.1 Bone

For the both the proximal and the distal parts of the humerus 10-node quadratic tetrahedron elements (Solid187) are used. A tetrahedron element has 4 triangle faces and 6 triangle cross-sections (figure 3.6). Solid187 element is a higher order 3D, 10-node element and has a quadratic displacement behavior and is well suited to modeling irregular meshes such as those produced from various CAD/CAM systems. The element is defined by 10 nodes having three degrees of freedom at each node (figure 3.7).

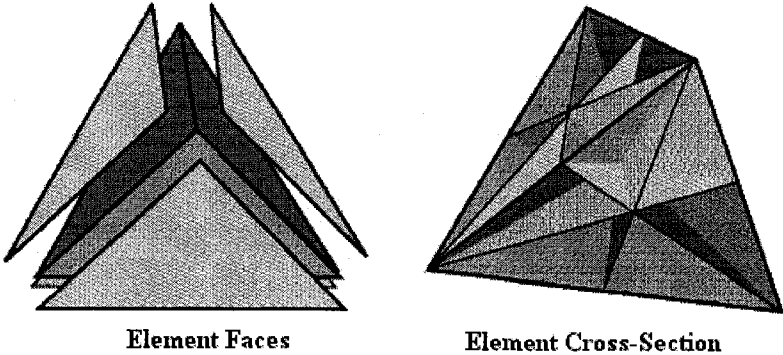


Figure 3.6: Left: Solid187 faces, Right: Solid 187 cross-section (Ansys)

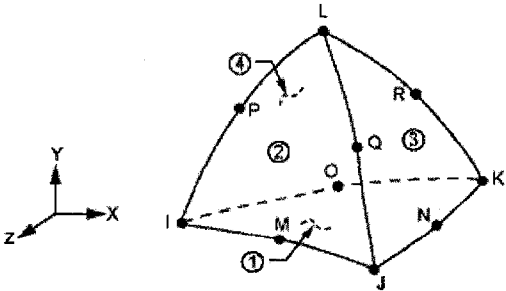


Figure 3.7: Solid187 geometry (Ansys)

Figure 3.8 shows the mesh and element plot of finite element model of the distal humerus. The proximal humerus is the mirror image.

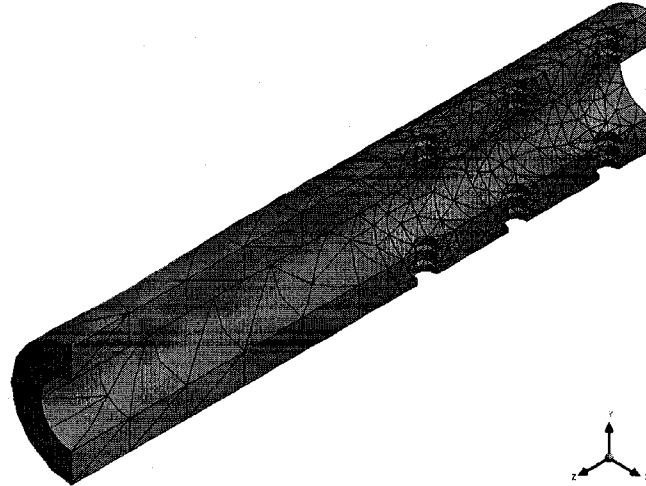


Figure 3.8: Bone model (distal humerus) mesh

A fine mesh is required for an accurate model solution in areas with high stress concentration. Mesh refinement is the process of increasing the mesh density in these areas until a desired level of accuracy is obtained. As can be seen in figure 3.8, a fine mesh was used in the regions of the screw holes and a coarser mesh was used for the regions away from the screw holes, especially at the proximal and distal ends.

3.4.2 Callus

For the callus which is in the mid-shaft humerus, 20-node quadratic hexahedron elements (Solid186) are used. Solid186 is a higher order 3D 20-node solid element that exhibits quadratic displacement behavior. The element is defined by 20 nodes having three degrees of freedom per node. Solid186 is available in two forms of structural solid and layered solid and the former used in this study. Solid186 Structural Solid is also well

suiting to modeling irregular meshes such as those produced by various CAD/CAM systems. Figure 3.9 represents the Solid186 structural geometry.

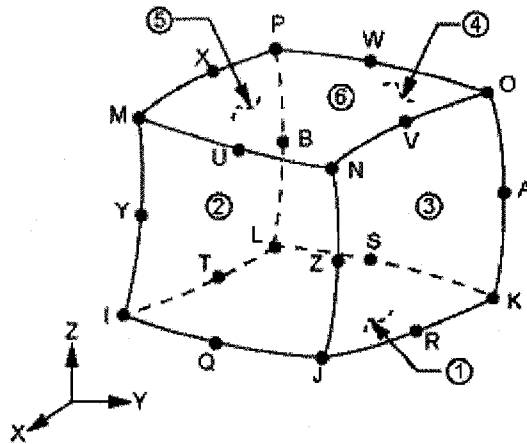


Figure 3.9: Solid187 geometry (Ansys)

These 3D 20-node elements allowed curvature to be displayed within an element and required fewer elements for the same degree of accuracy in the nodal solution. Figure 3.10 illustrates the element plot of callus.

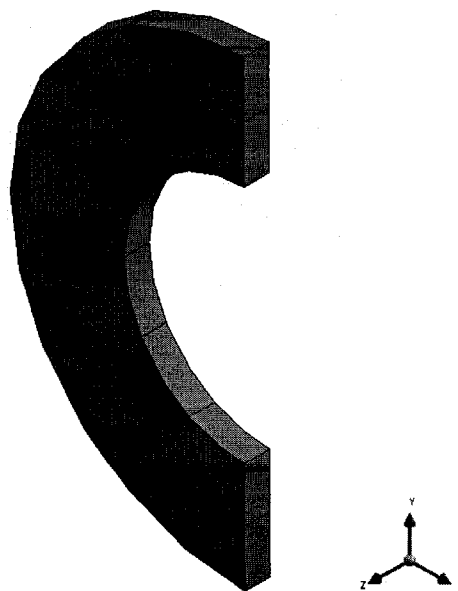


Figure 3.10: Callus mesh

The transition of elements at the surface of callus and both proximal and distal humerus is of great interest. Pyramid transitions happen when a swept or hex dominant body abuts, or shares faces with, a body meshed with tetrahedrons. The FE structural package will try to insert the pyramids into the body meshed with tetrahedrons. If that is not possible, the hexahedron at the boundary will be split into pyramids and tetrahedrons. In this study case, proximal and distal humerus is the dominant body meshed with tetrahedron elements while the callus is meshed with hexahedron elements; therefore, the latter situation occurs and 20-node hexahedron elements on the surface of the callus split into 20-node quadratic pyramid elements and 10-node quadratic tetrahedron. Figure 3.11 represents the 20-node quadratic pyramid elements at the interface of callus and bone.

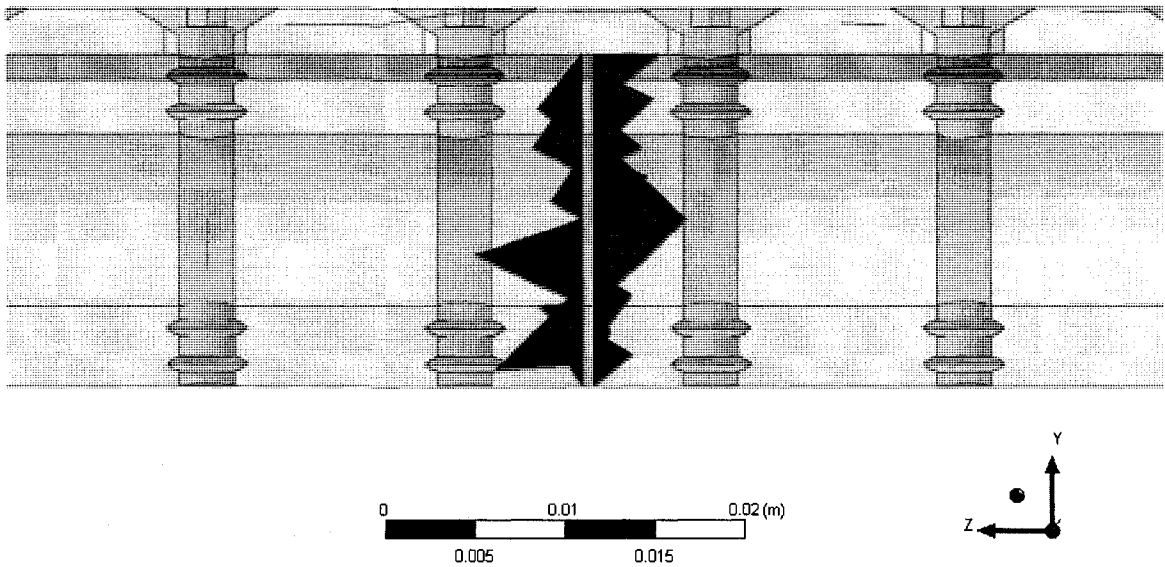


Figure 3.11: 20-node quadratic pyramid elements

3.4.3 Fracture plate and screws

For the fracture plate and screws 10-node quadratic tetrahedron elements are used. The specification of this element is discussed previously. Figures 3.12 and 3.13 show the element plot of fracture plate and screws.

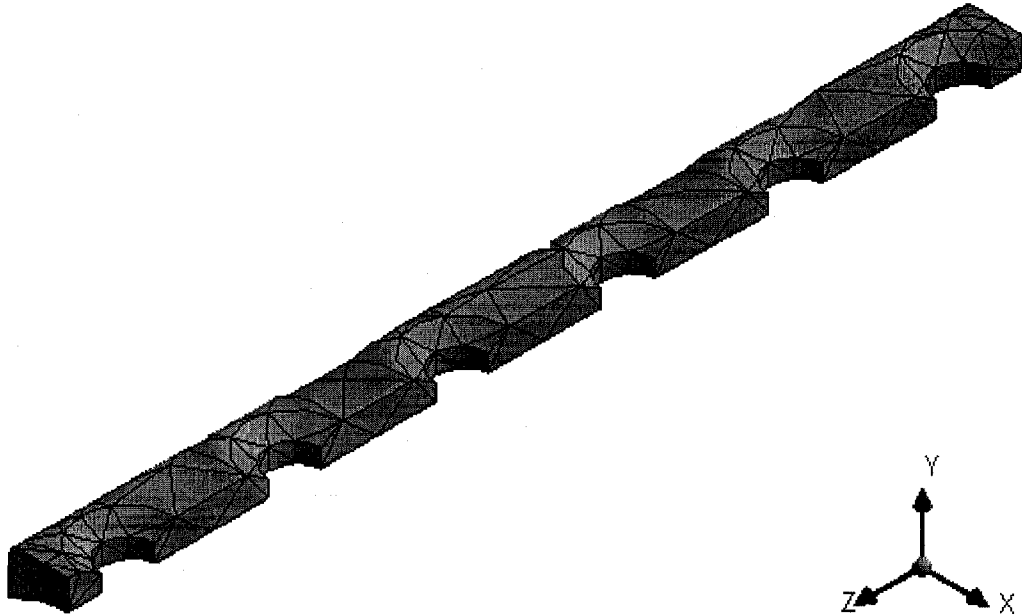


Figure 3.12: Fracture plate mesh

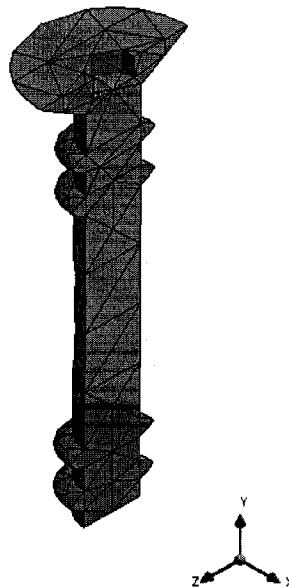


Figure 3.13: Screw mesh

The model's body statistics and element types are summarized in tables 3.2 and 3.3, respectively.

Table 3.2: Finite element model statistics

Body Name	Number of Nodes	Number of Elements	Element Type
Bone	10489	5409	Solid187
Callus	127	12	Solid186
Fracture Plate	733	274	Solid187
Screws	4208	1644	Solid187

Table 3.3: Elements statistics

Generic Element Type Name	ANSYS Name	Description
10 Node Quadratic Tetrahedron	Solid187	10 Node Tetrahedral Structural Solid
20 Node Quadratic Hexahedron	Solid186	20 Node Structural Solid
20 Node Quadratic Pyramid	Solid186	20 Node Structural Solid

3.5 Modeling the interfaces

The interface between two components of an assembly presents a unique problem for finite element analysis. In the common physical sense, two components can transmit compressive normal forces and tangential friction forces, but they often do not transmit tensile normal forces; they are therefore free to separate and move away from each other and a gap opens. ANSYS workbench 11.0 has specific contact elements to model these interfaces in three dimensions. Depending on the type of contact, the analysis can be linear or nonlinear. A nonlinear analysis can increase runtime significantly, as the solver will internally run iterations to arrive at a converged solution. The total load on the model

is subdivided into smaller load sub-steps and the program solves the model until every non-linear element is in equilibrium. At equilibrium, the load step is incremented and the process is repeated. The non-linear behavior can also lead to slow convergence or even non-convergence, as the solving algorithm is very sensitive to the size of the load step, the geometry of the model and the convergence tolerances. The following assumptions are made in the model:

- The screws are connected directly to the bone and the contact type in ANSYS is defined as a bonded contact and there is no sliding.
- The contact type at the interface of screw heads and fracture plate holes is defined as a bonded contact.
- Sliding is allowed between the bone and the fracture plate so the contact type is a frictional contact.

Therefore, for the interface of bone and screws and also for the interface of fracture plate and screw heads, coefficient of friction would be equal to 1. A friction coefficient of 1 would not allow any motion or slippage between the bone-screw as well as fracture plate-screw heads.

3.5.1 Fracture plate – screws head interface

FE structural package designated quadratic triangular contact element (Conta174), which is a 3D 8-node surface to surface contact element, is chosen for the fracture plate while the quadratic triangular target element (Conta170), which is a 3D target segment, is chosen for the screw heads. Figure 3.14 represents the contact pair for the fracture plate and screw heads. Red lines represent contact areas while blue lines represent target areas.

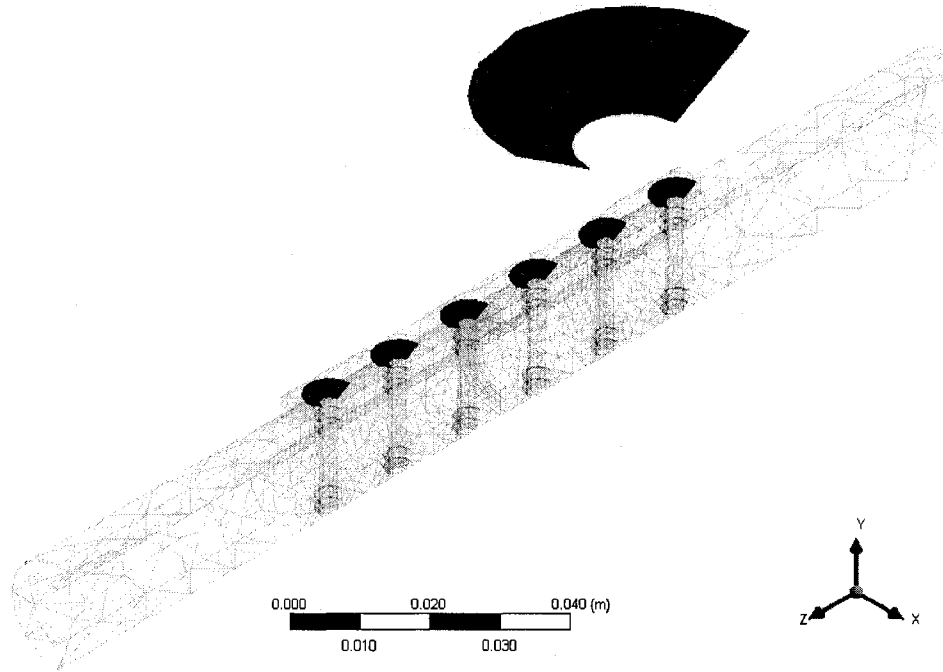


Figure 3.14: Fracture plate – screw heads interface

3.5.2 Bone – screw interface

FE structural package designated quadratic triangular contact element (Conta174), which is a 3D 8-node surface to surface contact element, is chosen for the bone while the quadratic triangular target element (Conta170), which is a 3D target segment, is chosen for the screw. Figure 3.15 represents the contact pair for the bone and the screw. Red lines represent contact areas while blue lines represent target areas.

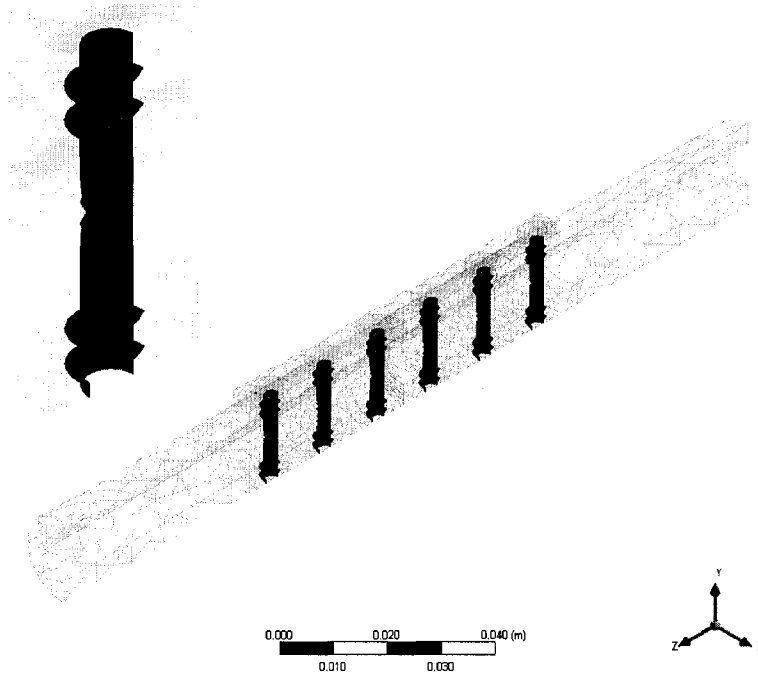


Figure 3.15: Bone – screw interface

The interface between the bone and screw is considered as a rigid structure and the coefficient of friction is chosen as 1. This means that there is no slippage and no pullout of the screw. The angle of screw insertion into the bone is perpendicular to the long axis of the humerus. Based on the Robert et al. (2003) the strongest bone plate interface occurs when the screws are inserted perpendicular to the long axis of the bone.

3.5.3 Bone – fracture plate interface

The relative motion between the fracture plate and the bone plays an important role in fracture healing process; therefore, it is not negligible (Foux et al., 1995). In order to investigate the micro-motion at the interface of bone and fracture plate, the contact type is defined as a frictional contact. In this case, frictional interface elements were used at all interfaces between the plate and the bone. The coefficient of friction at the bone-

plate interface was between 0.2 and 0.3 based on various studies (Beaupre et al., 1988). Since the purpose of having frictional contact pair is to determine the micro-motion in the interface of bone and screw, it is not critical that the frictional coefficient exactly matches its real magnitude; it is important that the friction coefficient be sufficient to allow the bodies to hold together during loading. In addition, in a non-linear contact analysis in ANSYS Workbench 11.0, the stiffness matrix would be asymmetric once the coefficient of friction is more than 0.2. Therefore, to reduce the process time the coefficient of friction is conservatively considered to be 0.2.

FE structural package determined quadratic triangular contact element (Conta174) is chosen for the bone as well as the callus, while quadratic triangular target element (Conta170) is chosen for the fracture plate. Figure 3.16 presents the contact pair for the bone and fracture plate. Red lines represent contact areas whereas blue lines represent target areas.

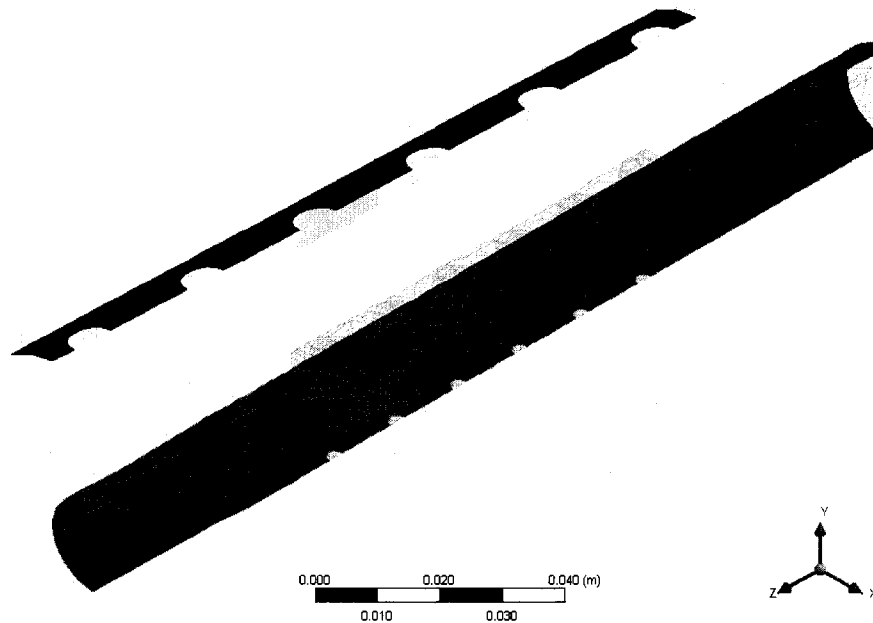


Figure 3.16: Bone – fracture plate interface

3.6 Materials selection

In this part, material properties of bone, fracture plate and screws are discussed.

3.6.1 Bone

As already mentioned in chapter 2, bone is a non-linear, anisotropic, non-homogeneous material with viscoelastic properties. Despite the fact that in most finite element studies bone is considered as a linear isotropic material, it can be modeled as either orthotropic or transversely isotropic. In this study, bone modeled as a transversely isotropic material. There have been several studies on the material properties of cortical bone in humans and animals. Material properties of the bone in this study are taken from Ramakrishna et al. (2004). Table 3.4 presents the material properties of the cortical bone used in this study.

Table 3.4: Material properties of cortical bone (Ramakrishna et al., 2004)

Cortical Bone	
E_1 (GPa)	14.5
E_2	14.5
E_3	19.7
G_{12} (GPa)	7.0
G_{13}	7.0
G_{23}	5.28
γ_{12}	0.285
γ_{13}	0.285
γ_{23}	0.265

3.6.2 Fracture plate and screws

The stiffness of a fracture fixation plate may have the stress shielding effect on the underlying bone, and refracture can happen after the fracture plate is removed (Cordey et al., 2000). Reducing the stiffness of the fixation plate is a way to reduce the shielding effect, but at the same time it may cause pain, discomfort and also non-union

healing. In order to compromise between the stiffness and the strength, two different plates were considered in this study.

It is important to consider the properties of the material before selecting a device for implantation. Two of the most commonly used materials are stainless steel and titanium Ti-6Al-4V. Browner and Edward (1989) suggested that a material for fabrication of a fracture fixation device should have the same material properties as bone, in order to reduce the effect of stress shielding by the device. In order to select the most suitable material for implantation, factors such as the biocompatibility and corrosion resistance should also be taken into account.

The biocompatibility of a material is one of the most important factors which need to be considered in the process of material selection. It determines whether adverse reactions will occur between the implant and surrounding tissues. Both materials have been shown to be biocompatible (Millar, 1997, Van der Elst, 1995, Holzach, 1978); stainless steel is rapidly coated in a bursa, while the Ti alloy may release debris upon metal-metal contact (Bischoff, 1994, La Budde, 1994, Salvati, 1993).

Corrosion resistance is another factor which should be considered in the material selection process. Pitting corrosion is an example in this case. It is a form of localized corrosion that leads to creation of small holes in the metal. The implanted metal is exposed to the salty environment of the body. This may lead to the pitting corrosion in a fracture fixation plate. While the titanium alloys seem to observe no pitting corrosion, this reaction has been seen in stainless steel (Taira and Lautenschlager, 1992). Galvanic corrosion, which may occur if dissimilar metals are used, can easily be avoided by choosing the same metals for all implant components.

The modulus of elasticity is another consideration in the selection of material. The modulus of 316 stainless steel is 193 GPa while the modulus of elasticity of Ti-6Al-4V is 96 GPa (Uthoff et al., 1981). Having a modulus of elasticity close to that of bone increases the load transfer to the bone and stimulates the healing and at the same time reduces the effect of stress shielding.

As the fracture heals, another surgery is necessary to remove the fracture plate, because there would be no need to have a rigid support in the body. In order to avoid this problem, some researchers have suggested the use of bioresorbable polymer screws and plates (Saidpour, 2006).

The experimental and clinical results have so far demonstrated some limitations of these new materials, such as poly-L-lactide (PLLA), carbon fiber composites (Manninen et al., 1992). There are also some disadvantages of using composite plates. For instance, interaction of body fluids with the matrix material may degrade the properties of the composite before bone healing has been completed. In this case, carbon fiber fragments can also move into the neighboring tissues (Suuronen et al., 1992). Another concern is their flexibility compared to stainless steel or titanium. Elasticity of metals helps the surgeon to reshape the plate during the operation while the lack of ductility in composites, compared to metals, prevents reshaping them during the operation (Suuronen et al., 1992).

Claes (1989) conducted an extensive study of the fracture behavior of 6-hole plate design made from carbon fiber reinforced carbon composite (CFRP). CFRP has low density, and high Young's modulus and strength. Various investigators have shown that application of a single metal plate produces a mean reduction in both axial stress and

strain ranging from 28–45% of nonplated values. (Foux et al., 1995) calculated values of P (the fraction of load carried by the bone) of approximately 50% for a standard stainless steel plate and 76% for the axially flexible plate (AFP) system with PLLA inserts.

The screws in this study were modeled as having been made of the same material as the plate in which they were inserted, 316 stainless steel in case of the stainless steel plate and Ti-6Al-4V in the case of the Ti alloy plate. Table 3.5 summarizes the material properties of which are used in this study to model the fracture plate and screws.

Table 3.5: Material properties statistics

Material Properties	316 stainless steel	Ti-6Al-4V
Young's modulus (GPa)	193	96
Poisson's ratio	0.31	0.36
Yield strength (MPa)	207	930
Ultimate strength (MPa)	586	1070

3.7 Boundary conditions

3.7.1 Constraints

Symmetry with reference to the loading and geometry is used to reduce the model size and, hence, maximize the computational efficiency. The model is assumed to be symmetric about the long axis of the bone, as shown in figure 3.17. However, this symmetry plane is only valid for tensile, compressive and bending loads and not for the torsional load. So, for torsion, no symmetry plane is used.

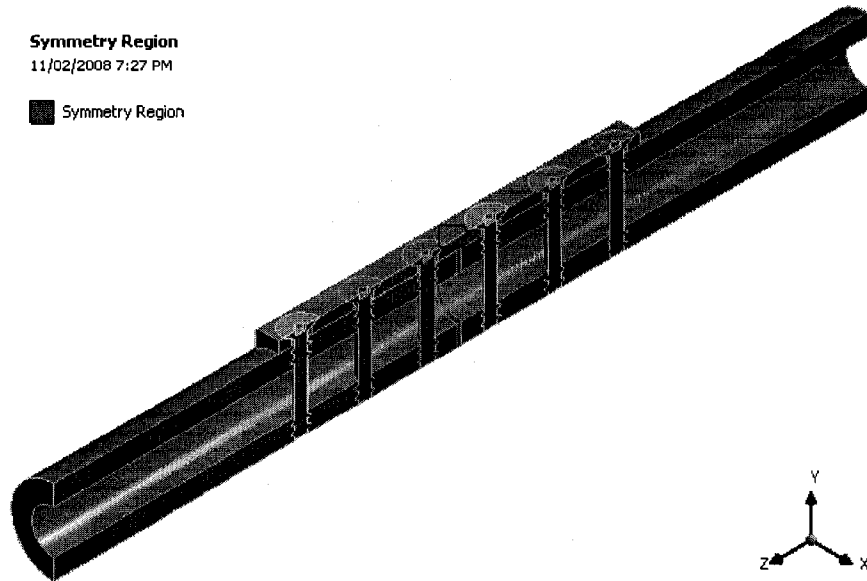


Figure 3.17: Symmetry plane

It is also assumed that displacement at the proximal end of the humerus is zero in any direction. Therefore, in ANSYS Workbench 11.0, a fixed displacement is defined at the proximal end of the bone finite element model, as shown in figure 3.18.

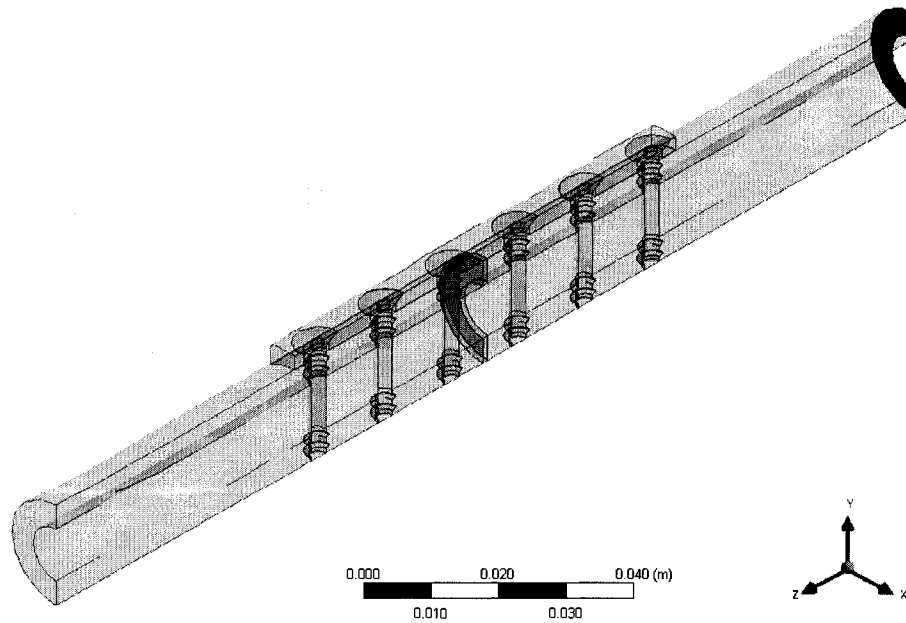


Figure 3.18: Displacement at the proximal end of humerus

3.7.2 Loading conditions

When the orthopedic surgeon mounts the fracture plate, tightening of the screws results in tension in the screws. The pretension element in the Ansys Workbench 11.0 is used to model this. As shown in figure 3.19, the pretension is only applied to part of the screw, namely the section between the head of the screw and bone directly below the plate. The magnitude of this pretension force is 10 N per screw.

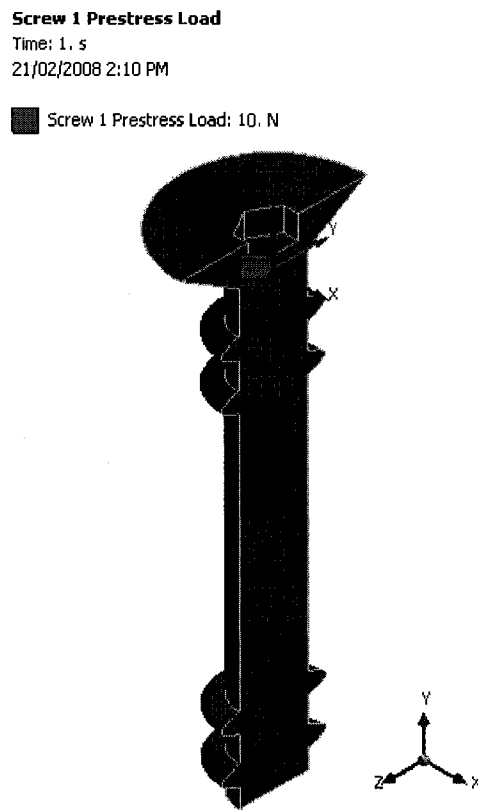


Figure 3.19: Pretension in a screw

Three loading conditions were considered:

1. Getting up from a chair
2. Lifting a suitcase
3. Turning a screw driver

3.7.2.1 Getting up from a chair

In this part, an elementary stress analysis of the humerus is performed to obtain the magnitude of the bending moment as well as the compressive force at the humerus. The stress analysis of the humerus is conducted for a person who is rising from an office chair. In a sitting posture on an office chair about 80% of the body weight is transferred through the chair seat to the ground and the rest by the feet which are touching the ground. As a result, when a person is rising from a chair hands and arms bear about 80% of the body weight once the seat cushion no longer provides any support. This percentage was measured by placing a scale on the seat cushion, measuring the weight carried by the scale, and thus the seat, and expressing this weight as a percentage of body weight. This percentage can also be estimated from anthropometric data. Pheasant (1986) presents the following data:

Table 3.6: Weights and centers of gravity of body segments (Pheasant, 1986)

Segment	Weight (% body weight)	Location of centre of gravity
Head-neck-trunk	58.4	
Upper arm	2.8	48% of distance from shoulder to elbow
Forearm	1.7	41% of distance from elbow to wrist
Hand	0.6	
Thigh	10.0	

It is assumed that 60% of thigh weight is born by the chair seat cushion.

Consequently, the chair weight can be calculated as follows:

$$W_T = 58.4\% + (2 \times 5.1\%) + 0.6 \times (2 \times 10.0\%) = 80.6\% \quad (1)$$

Consider the force acting on the hand of a 75 kg person who is rising up from a chair at the moment his buttocks come off the chair seat. Figure 3.20 shows this in diagrammatic form. It is assumed that the length of upper arm is equal to the distance from elbow to palm. It is further assumed that the palm is located directly below the shoulder.

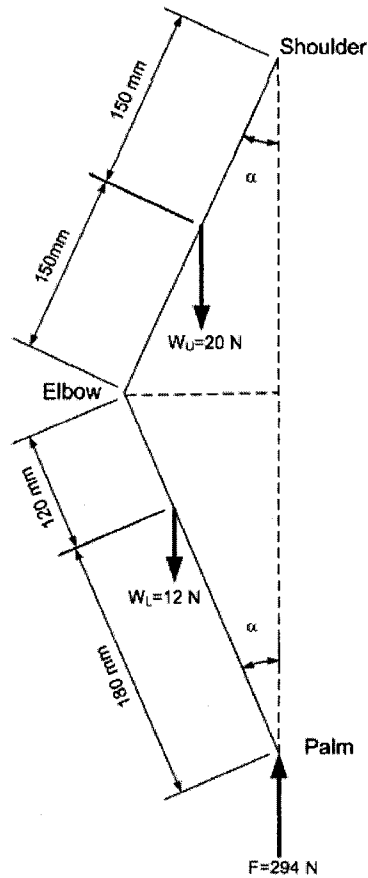


Figure 3.20: Diagram of upper arm and lower arm

The symbol F represents the reaction force that the arm rest exerts on one hand and is calculated as follows:

$$F = 75\text{ kg} \times 0.8 \times 0.5 = 30\text{ kg} \rightarrow F = 30 \times 9.81 \cong 294\text{ N} \quad (2)$$

W_U stands for the weight of upper arm while W_L corresponds to the weight of lower arm.

α is the angle between the lower arm and the armrest.

In order to calculate compressive and shear forces on the elbow for different angles, a free body diagram of the lower arm is drawn (figure 3.21). The force applied to the palm and the weight of the lower arm cause a moment about the elbow. This is counteracted by a force generated by the triceps.

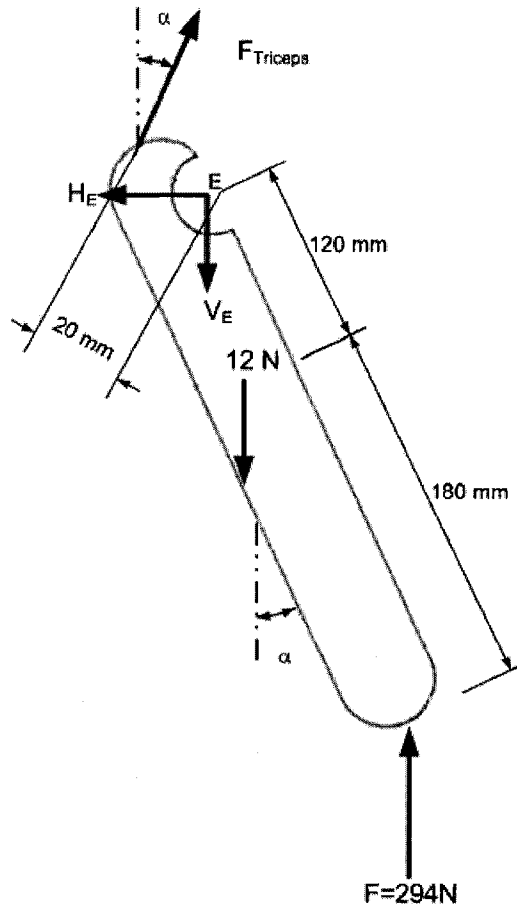


Figure 3.21: Free body diagram of lower arm

Moment equilibrium conditions require that the sum of the moment about the center of the elbow joint be zero. This results in the expression,

$$\sum M_E = 0 \Rightarrow -294 \times 0.3 \sin \alpha + 12 \times 0.12 \sin \alpha + F_{Triceps} \times d = 0$$

$$-88.2 \sin \alpha + 1.44 \sin \alpha + F_{Triceps} \times 0.02 = 0 \Rightarrow F_{triceps} = \frac{86.76 \sin \alpha}{0.02} \quad (3)$$

$$F_{Triceps} = 4350 \sin a$$

The force equilibrium condition requires the sum of the forces in both horizontal and vertical direction be zero. Thus, for the horizontal direction,

$$H_E = F_{Triceps} \sin \alpha \quad (4)$$

And for the vertical direction,

$$V_E = (294 - 12) + F_{Triceps} \cos \alpha \quad (5)$$

Based on the aforementioned calculations, the forces at the elbow joint are,

$$\begin{aligned} F_{Triceps} &= 4350 \sin \alpha \\ H_E &= 4350 \sin^2 \alpha \\ V_E &= 282 + 2175 \sin 2\alpha \end{aligned} \quad (6)$$

Figure 3.22 presents the free body diagram of the humerus and shows the forces and moment acting on it.

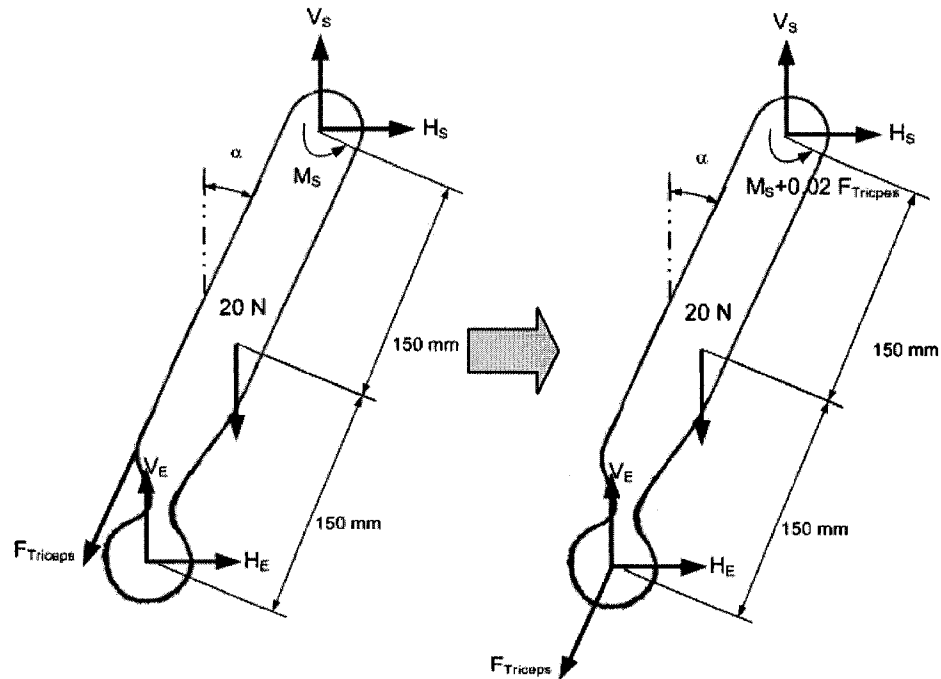


Figure 3.22: Free body diagram of the upper arm

The forces at the elbow need to be expressed as compressive and shear forces.

Figure 3.23 illustrates this conversion.

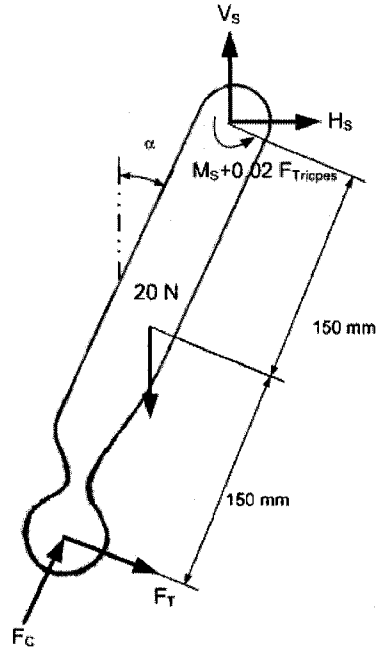


Figure 3.23: Modified free body diagram of the upper arm

Considering the free body diagrams of the humerus in figure 3.22 and 3.23, the value of the compressive and shear forces can be calculated as follows:

$$\begin{aligned} F_C &= -F_{Triceps} + V_E \cos \alpha + H_E \sin \alpha \\ F_T &= -V_E \sin \alpha + H_E \cos \alpha \end{aligned} \quad (7)$$

Substituting equation 6 results in:

$$\begin{aligned} F_C &= -4350 \sin \alpha + (282 + 2175 \sin 2\alpha) \cos \alpha + (4350 \sin^2 \alpha) \sin \alpha \\ F_T &= -(282 + 2175 \sin 2\alpha) \sin \alpha + (4350 \sin^2 \alpha) \cos \alpha \end{aligned} \quad (8)$$

Equation 8 can be used to calculate the magnitude of the compressive and shear forces for the humerus during the rising up from a chair. Therefore, F_C and F_T are calculated for 45° , 30° , 15° , and 0° , as shown in table 3.7 below.

Table 3.7: Compressive and shear force in elbow with respect to the angle of lower arm and armrest

α (degree)	45°	30°	15°	0°
F_C (N)	199.4	244.2	272.4	282.0
F_T (N)	199.4	141.0	73.0	0.0

3.7.2.2 Lifting a suitcase

The standard maximum weight of a suitcase that major airline companies such as Air Canada allow is, 23 kg, or 226 N. This weight is used to study tensile loading of the humerus. It is assumed that the arm is straight.

3.7.2.3 Turning a screw driver

A quick experiment using one male subject was performed to determine the maximum twisting moment applied to the humerus during a simulated activity of turning a screw using a screw driver. This experiment was done using the work simulator at Concordia University's Human Factors laboratory. Upper arm, forearm and screw driver were kept in a straight line. This means that the twisting moment applied to the humerus is the same as that applied to the hand. Table 3.8 shows the result of this experiment.

Table 3.8: Maximum twisting moment applied to the humerus

		Twisting moment (Nm)
Right Hand	Clockwise	6.4
	Counter clockwise	4.4
Left Hand	Clockwise	3.7
	Counter clockwise	4.1

In order to investigate the effect of a twisting moment on the humerus, only the maximum value, 6.4 Nm, is considered.

3.7.2.4 Summary of load cases investigated

Table 3.9 summarizes the types of loads and their magnitudes considered in this research.

Table 3.9: Summary of load cases investigated

Load case No.	Type of load		Value
1	Pure compression ($\alpha=0^\circ$)		-282 N
2	Pure tension ($\alpha=0^\circ$)		226 N
3	Compression and shear (generates bending moment)	($\alpha=15^\circ$)	$F_C = -272.4$ N $F_T = -73.0$ N
		($\alpha=30^\circ$)	$F_C = -244.2$ N $F_T = -141.0$ N
		($\alpha=45^\circ$)	$F_C = -199.4$ N $F_T = -199.4$ N
4	Twisting moment ($\alpha=0^\circ$)		6.4 Nm

Note that α is the angle of the upper and lower arms with the vertical. The corresponding elbow angle is $180^\circ - 2\alpha$.

4. Results and discussion

In this chapter, the results of the finite element analysis of internal states of stress and strain under different load conditions are presented. In addition, the results of bonded contact for the interfaces of bone-screw and fracture plate-screw heads as well as the outcomes of the frictional contact for the interface of the bone and the fracture plate are included. This chapter concludes with detailed summaries of the presented results and their relevant statistical data. It also provides tables in order to compare the mechanical performance of the two fracture plates to determine the advantages and disadvantages of each plate. Figure 4.1 shows the FE model consisting of the distal and proximal humerus, the callus in between, the fracture plate and the six screws, together with the coordinate system used.

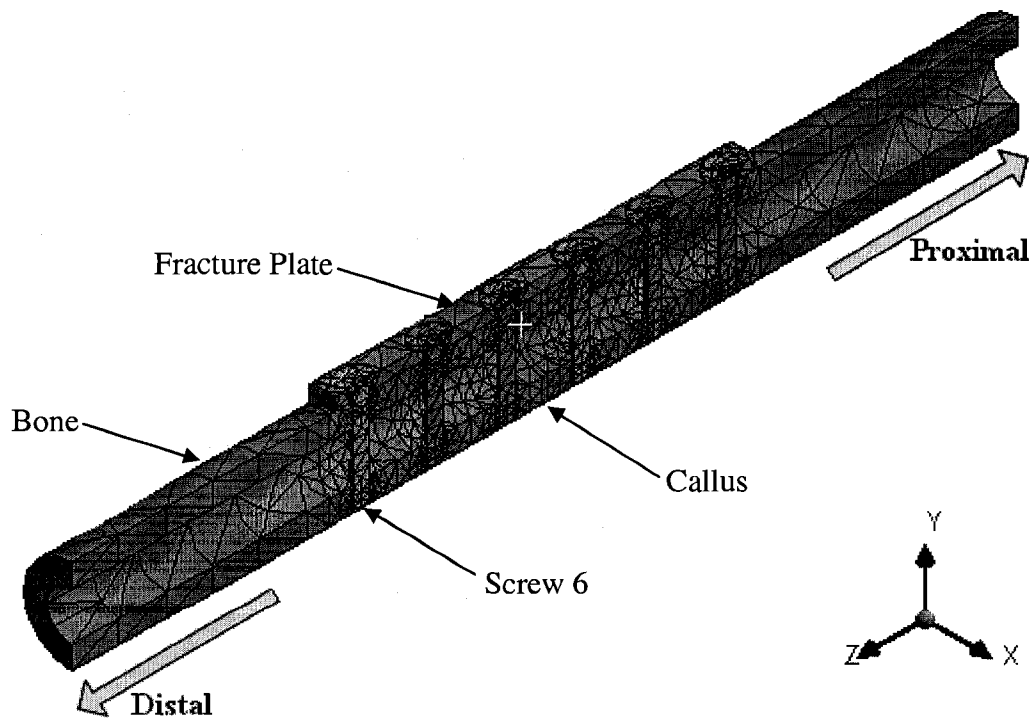


Figure 4.1: Finite element model of bone, plate, screws and callus

The z-axis coincides with the long axis of the bone and the y-axis with the screw axes. The screws and screw holes will be referred by numbers, with the first screw in proximal humerus and the sixth screw in distal humerus. von-Mises equivalent stress is useful for predicting failure in some engineering materials. The von-Mises yields criterion predicts failure in a material under complex loading from the yield strength of that material under simple uniaxial tension. Since the von-Mises failure criterion is usually applied to ductile materials, it is controversial if this is valid for a material such as bone. The von-Mises equivalent stress provides a measure of the total magnitude of stress at a point and can provide some valid information, taken in context with the other calculated stress magnitudes and directions (Ferguson, 1994)

4.1 Load case 1 – pure compression

In this case, a compressive load of 282 N is applied. Two plates, stainless steel and Ti-6Al-4V, are examined and the results of the finite element analysis for different stages of the healing process are presented. Figure 4.2 depicts the stress distribution in the model with a SS plate for the 1st week of fracture healing. For the Ti plate the stress contours are the same. The following sections describe the stress distribution in each of the components and a summary table is presented at the end.

Equivalent Stress

Type: Equivalent (von-Mises) Stress

Unit: Pa

Time: 1

01/03/2008 3:51 PM

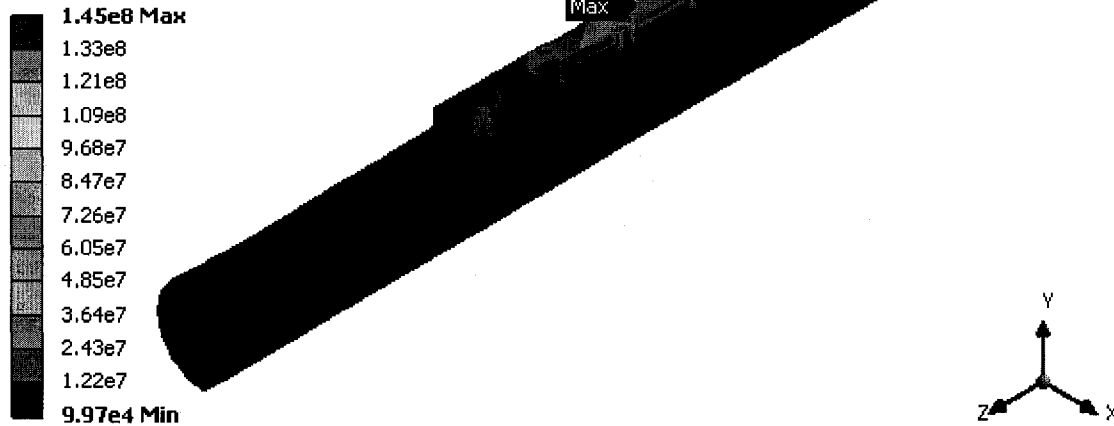


Figure 4.2: Stress distribution in the model with a SS plate for the 1st week of healing

4.1.1 Stress distribution in the bone: pure compression case

The maximum equivalent von-Mises stress in bone with the SS and Ti plates during the 1st week of healing was 13.7 MPa and 13.9 MPa, respectively. In the 3rd week of healing, the magnitude of this stress in bone with the SS plate decreased to 8.3 MPa, and to 8.9 MPa with the Ti plate. During the following weeks of healing, this magnitude remained constant. Maximum stress concentration for both models occurred near the head of the 6th screw in the distal humerus. The magnitude of the maximum equivalent von-Mises stress in the bone with the Ti plate is almost always 6% higher than of that with the SS plate. So, when using the Ti plate, a greater portion of load transmits through the bone and consequently the effect of stress shielding will be reduced. Figure 4.3 illustrates the stress distribution in the bone with a SS plate in the 6th week of healing, while figure 4.4 shows the same but with the Ti plate.

Equivalent Stress - Bone

Type: Equivalent (von-Mises) Stress

Unit: Pa

Time: 1

01/03/2008 3:59 PM

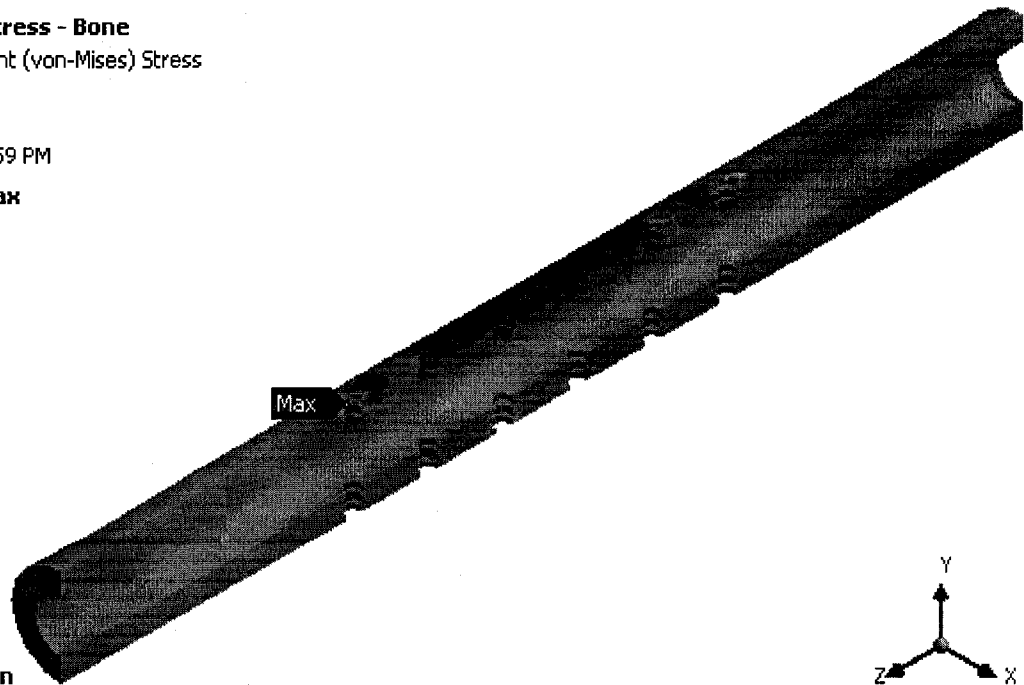
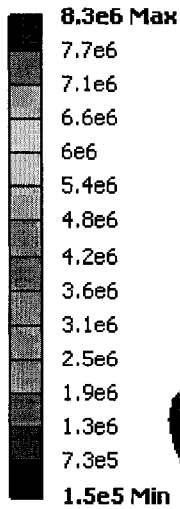


Figure 4.3: Stress distribution in the bone with the SS fracture plate for the 6th week of healing

Equivalent Stress - Bone

Type: Equivalent (von-Mises) Stress

Unit: Pa

Time: 1

01/03/2008 3:59 PM

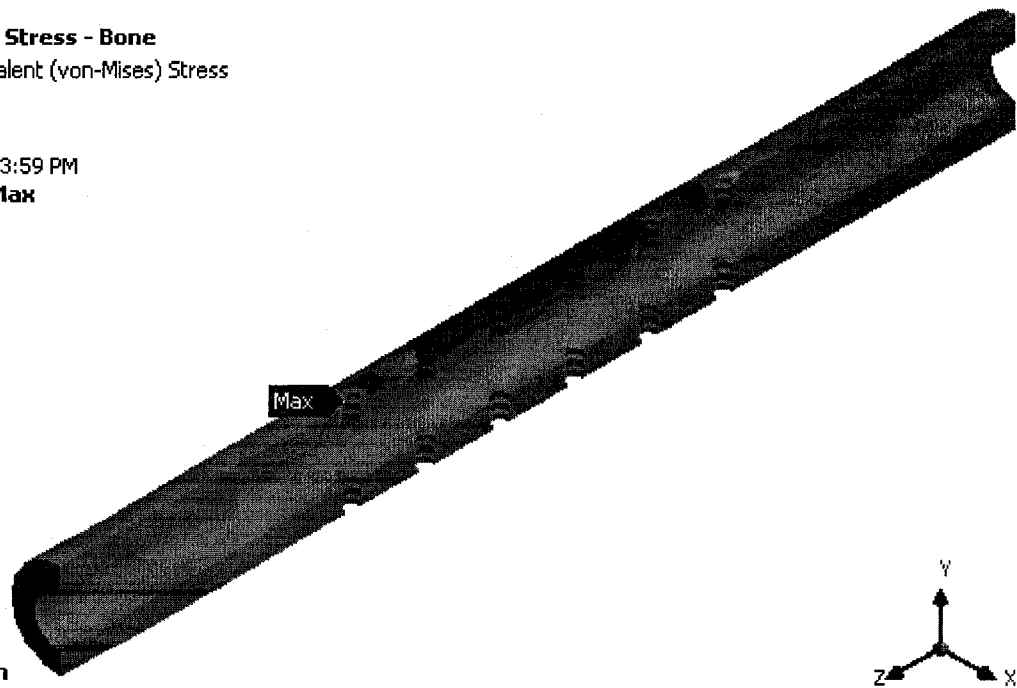
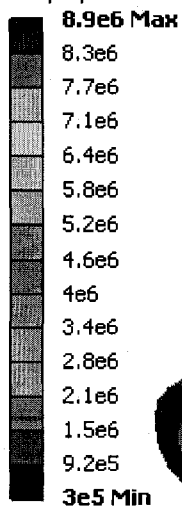


Figure 4.4: Stress distribution in the bone with the Ti fracture plate for the 6th week of healing

4.1.2 Stress distribution in the plate: pure compression case

The maximum equivalent von-Mises stress in the fracture plate followed the same pattern as that shown in the bone. The plate bent under the applied load transferred through the screws. The maximum equivalent von-Mises stress during the 1st week of healing in the SS fracture plate was 145.2 MPa while its magnitude was 95.2 MPa in the Ti plate. In the 3rd week of healing, the magnitude of the maximum equivalent stress in the SS plate reduced by 87.9% to 17.6 MPa and stayed steady for the rest of the period. This trend was the same for the Ti plate and the amount of maximum equivalent stress reduced to 12.6 MPa which is 86.8% less than of that in the 1st week of healing. The maximum equivalent von-Mises stress in both the SS and Ti plates during the 1st week of healing occurred at the interface of plate and bone in the fracture gap (figure 4.5). However, this location changed in the following weeks and transferred to the interface of the 6th screw and hole (figure 4.6).

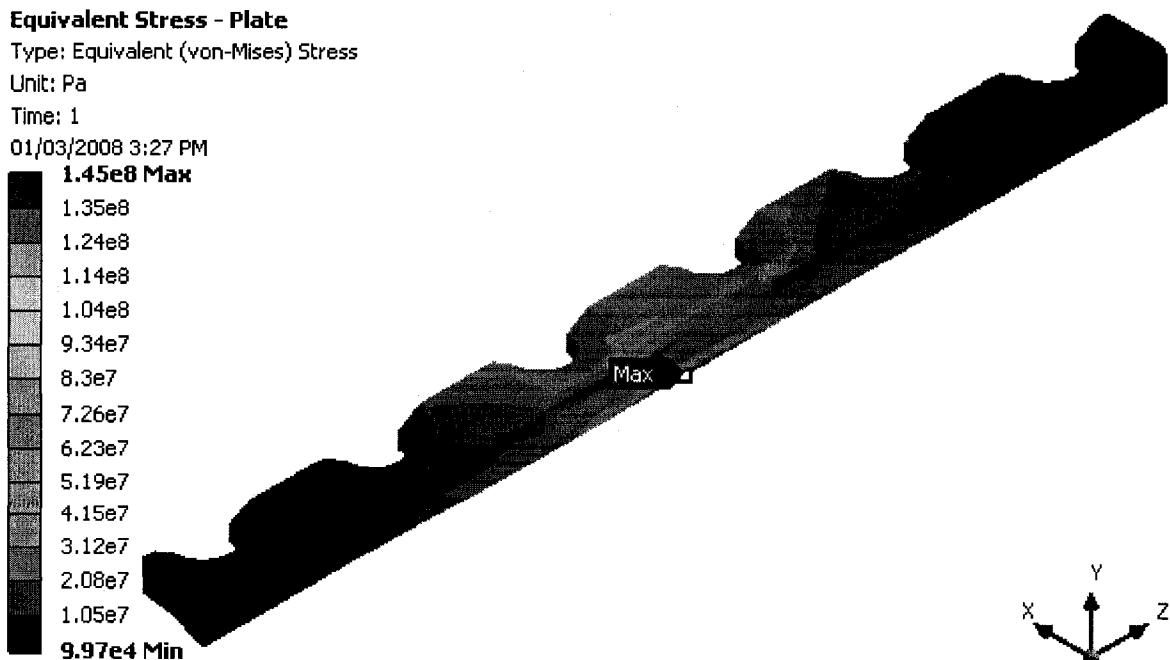


Figure 4.5: Stress distribution in the SS plate for the 1st of week of healing



Figure 4.6: Stress distribution in the SS plate for the 3rd week of healing

4.1.3 Stress distribution in the screws: pure compression case

The maximum equivalent von-Mises stress in the stainless steel screws reduced from 134.8 MPa in the 1st week to 27.7 MPa in the 3rd week of healing and remained constant during the following weeks of healing. For the titanium screws the maximum equivalent von-Mises stress decreased from 73.9 MPa in the 1st week to 20.7 MPa in the 3rd week and stayed steady during the following weeks. In other words, the magnitude of the maximum equivalent stress in the SS screws reduced by 79.5% during the healing process. This was 72.0% for the Ti screws.

The maximum equivalent stress in the SS screws during the 1st week of healing occurred in the 4th screw which is located in the distal humerus close to the fracture gap. For the Ti screws it occurred in the 3rd screw located in the proximal humerus near to the fracture gap. Figure 4.7 shows the stress distribution in the stainless steel screws, and figure 4.8 illustrates the stress distribution in the titanium screws.

Equivalent Stress - Screws

Type: Equivalent (von-Mises) Stress
Unit: Pa
Time: 1
01/03/2008 4:04 PM

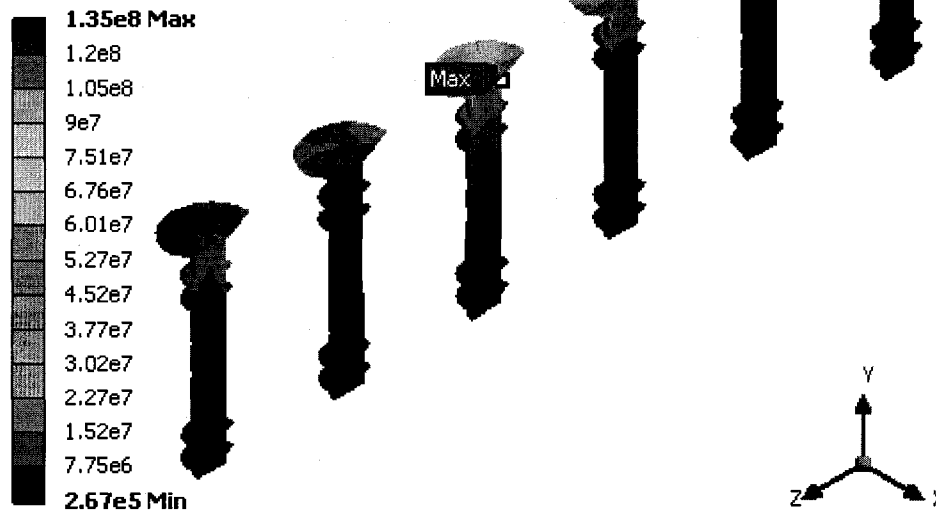


Figure 4.7: Stress distribution in the stainless steel screws for the 1st week of healing

Equivalent Stress

Type: Equivalent (von-Mises) Stress
Unit: Pa
Time: 1
01/03/2008 4:09 PM



Figure 4.8: Stress distribution in the titanium screws for the 1st week of healing

Figures 4.7 and 4.8 show that the screws closest to the fracture gap have the highest stress. During the 8th week of healing, the screws farthest away from the fracture gap have the highest stress. Figure 4.9 illustrates the stress distribution in the stainless steel screws during the last week of healing.

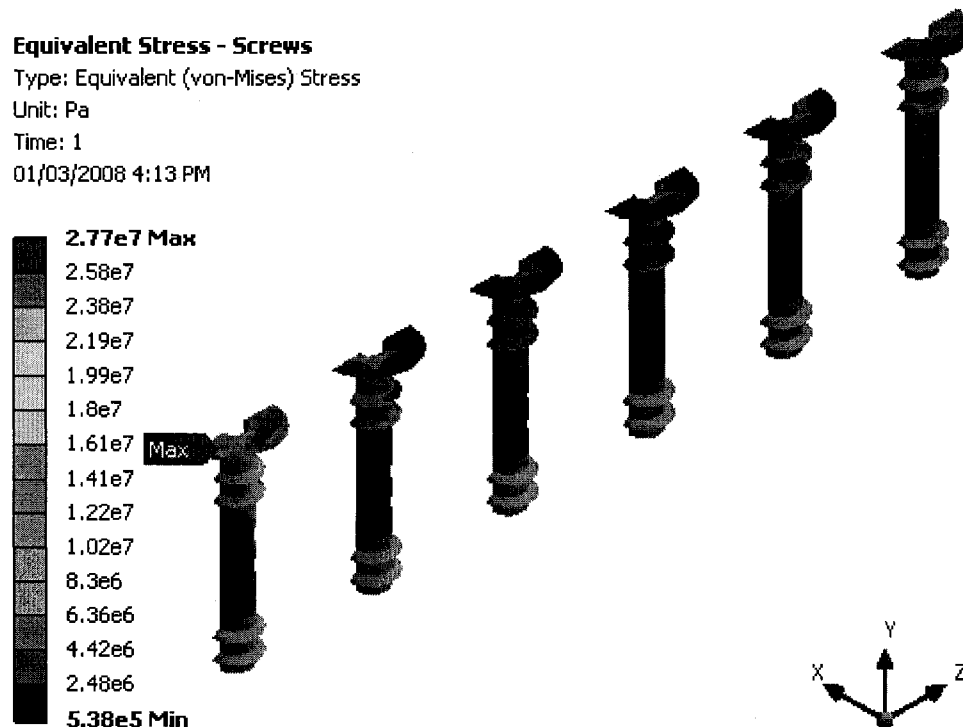


Figure 4.9: Stress distribution in the stainless steel screws for the 8th week of healing

4.1.4 Stress distribution in the callus: pure compression case

When the SS plate is used, the maximum equivalent von-Mises stress in the callus during the 1st week of healing is 2.6 MPa and occurred at the bottom of the bone, farthest away from the plate. In the 3rd week of healing, this maximum equivalent stress increased by 50% to 3.9 MPa. This means that a larger portion of load is transmitted through the newly-formed callus. The magnitude of this stress in 6th and 8th weeks of healing was 4.3 MPa and 4.6 MPa, respectively. Figure 4.10 shows the stress distribution in the callus at

different stages of healing in case of the SS plate. The same behavior in the callus is observed if a Ti plate is used.

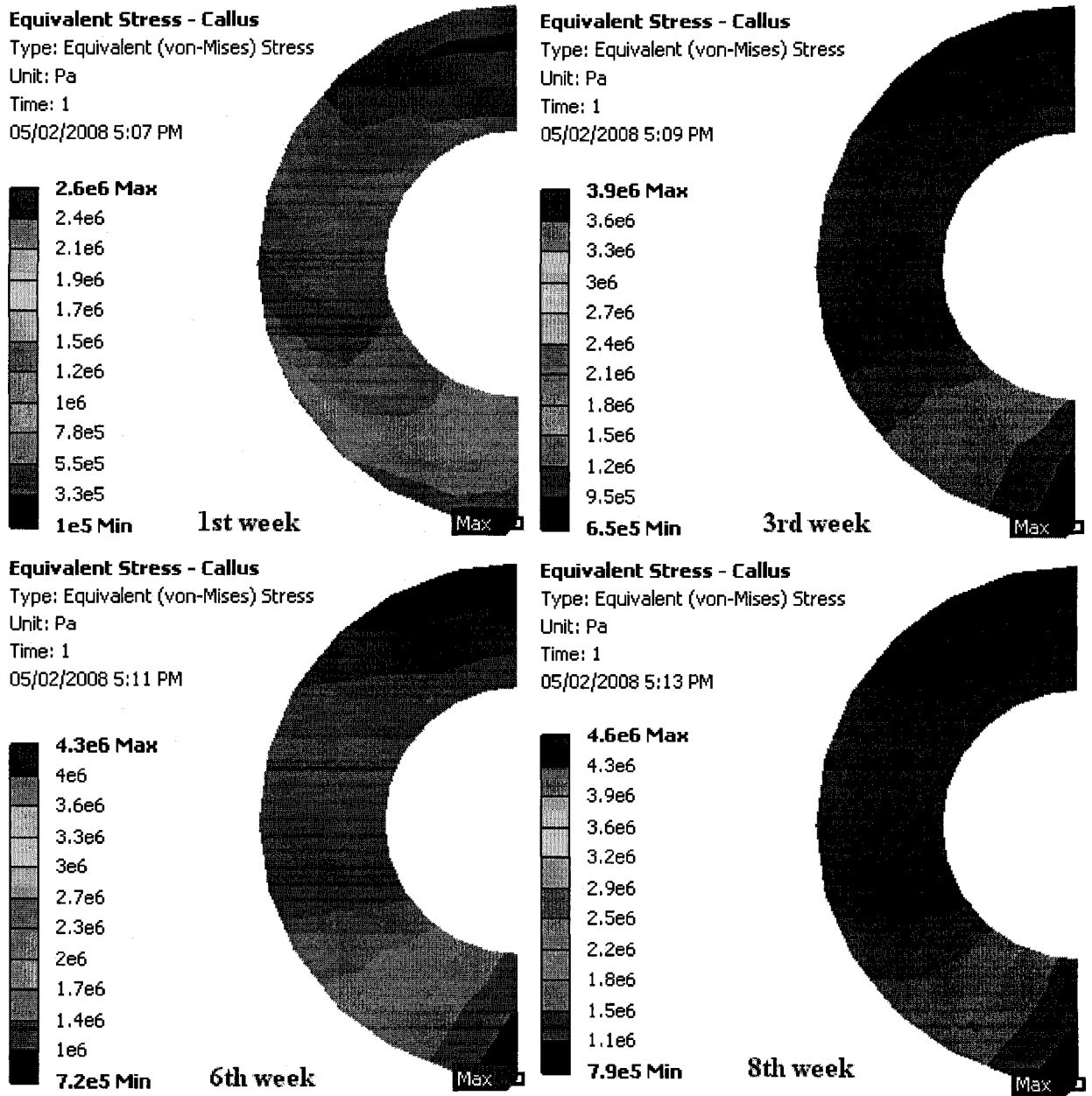


Figure 4.10: Stress distribution in the callus during different stages of the healing process in case of a SS plate

4.1.5 Summary and discussion of the stresses: pure compression case

Table 4.1 presents the magnitude of the maximum equivalent von-Mises stress in each of the parts, namely bone, fracture plate, screws and callus, at different stages of fracture healing.

Table 4.1: Maximum equivalent von-Mises stresses in different parts of the assembly

		Maximum equivalent stress (MPa)			
		1 st week	3 rd week	6 th week	8 th week
Bone	SS	13.7	8.3	8.3	8.3
	Ti	13.9	8.9	8.9	8.8
Plate	SS	145.2	17.6	17.6	17.6
	Ti	93.2	12.6	12.6	12.6
Screw	SS	134.8	27.7	27.7	27.7
	Ti	73.9	20.7	20.7	20.7
Callus	SS	2.6	3.9	4.3	4.6
	Ti	2.9	3.7	4.0	4.4

The maximum equivalent von-Mises stress in the assembly during the 1st week of healing for both SS and Ti plates occurs in the fracture plate. The magnitude of this stress is 145.2 MPa in the SS plate and 93.2 MPa in the Ti plate. Based on Gomez et al. (2006), having such a high stress in the plate is due to the Young's modulus of the callus which is 1% of that of healthy bone. It means that during the 1st week of healing, almost no callus has been formed in the fracture gap. Therefore, a greater portion of the load is transmitted through the fracture plate and the stress concentration will be higher in the fracture area. In the 3rd week of fracture healing, the Young's modulus of the callus is almost 50% of that of healthy bone (Gomez et al., 2006). As a result, the callus starts transmitting the load and the stress concentration in the fracture plate reduces. The Young's modulus of

the callus increases to 75% and 100% of that of healthy bone in the 6th and 8th week, respectively. Even though the Young's modulus increases, the maximum equivalent von-Mises stress remains steady during this period. This trend is the same for both the SS plate and the Ti plate.

4.1.6 Elastic strains: pure compression case

The equivalent von-Mises elastic strains in these models also follow the same patterns as the equivalent stresses. Due to the low Young's modulus of the callus in the assembly during the healing process, the maximum equivalent von-Mises elastic strain is always at the bottom side of the bone. Table 4.2 shows the amount of these elastic strains in the assembly.

Table 4.2: Maximum equivalent elastic von-Mises strains in different parts of the assembly

		Maximum equivalent elastic strain			
		1 st week	3 rd week	6 th week	8 th week
Bone	SS	0.13	0.00046	0.00044	0.00044
	Ti	0.14	0.00048	0.00048	0.00048
Plate	SS	0.00075	0.00009	0.00009	0.00009
	Ti	0.00097	0.00013	0.00013	0.00013
Screw	SS	0.00069	0.00014	0.00014	0.00014
	Ti	0.00077	0.00022	0.000224	0.00022
Callus	SS	0.13	0.00046	0.00033	0.00027
	Ti	0.14	0.00043	0.00031	0.00025

4.1.7 Contact analysis of the bone-plate interface: pure compression case

As previously mentioned (section 3.5), there exists frictional contact at the interface of the bone and the fracture plate. Therefore, it is of great interest to investigate the frictional contact in this area. Since the interfaces of fracture plate - screw head and

bone - screw were defined as bonded contacts, there is no relative motion at these interfaces. However, this situation is different at the interface of the bone and the fracture plate. As a result, there exists relative motion between the bone and the fracture plate (figure 4.11). The maximum sliding between the fracture plate and the bone occurred at the distal end of the contact area for both the SS and Ti plates. Figure 4.12 depicts the sliding distance of the SS fracture plate relative to the bone during the 3rd week of healing process. The magnitude of these relative motions is presented in table 4.3.

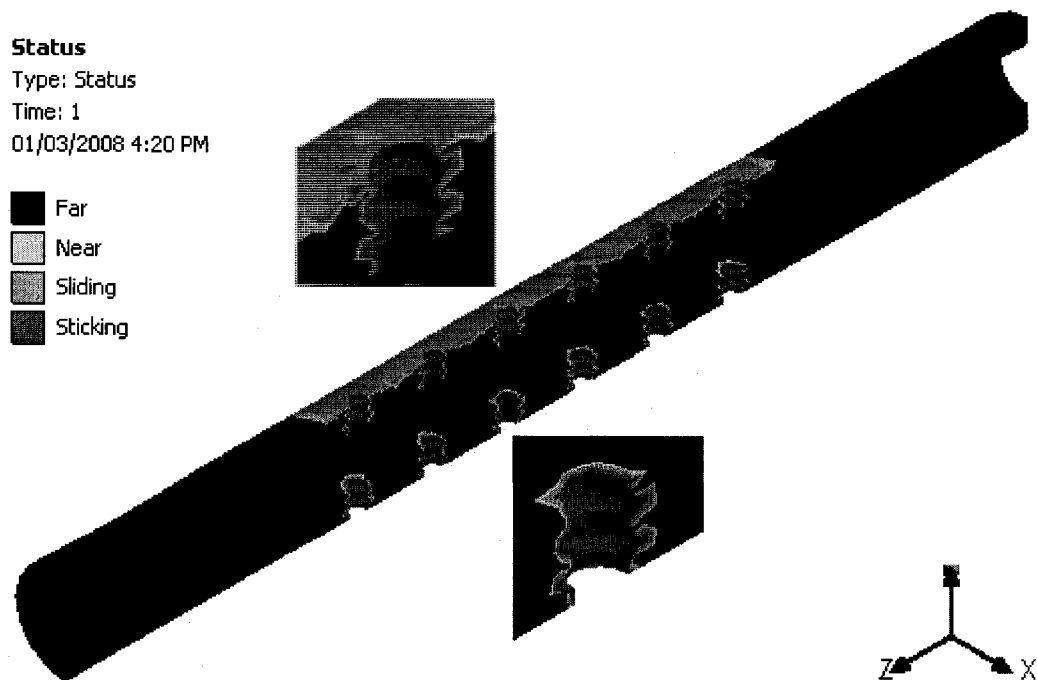


Figure 4.11: Contact at the bone and the SS plate interface for the 3rd week of healing

Sliding Distance

Type: Sliding Distance

Unit: m

Time: 1

01/03/2008 4:23 PM

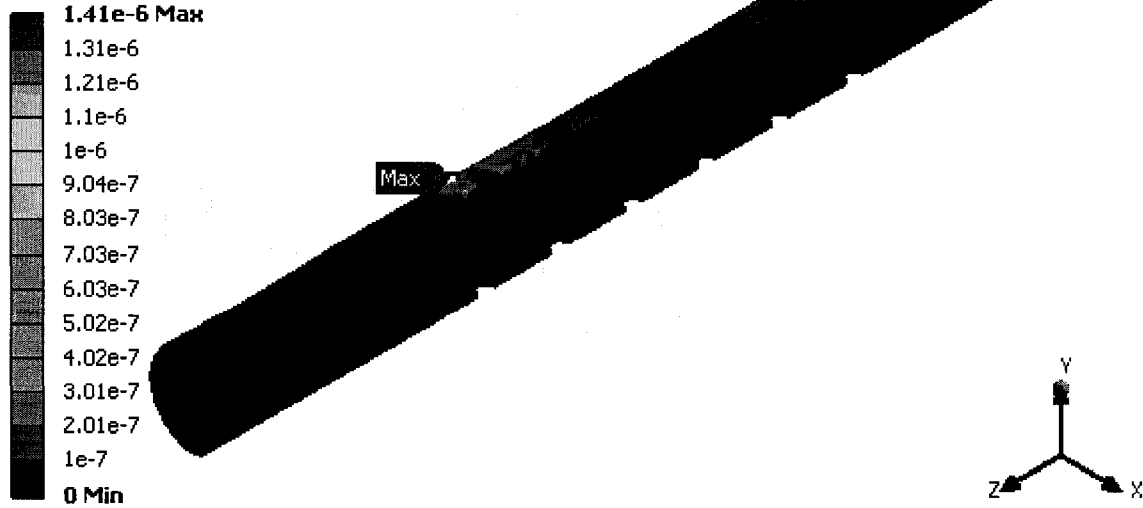


Figure 4.12: Relative motion between the bone and the SS plate for the 3rd week of healing

Table 4.3: Maximum relative motions at the interface of bone and fracture plate

	Maximum relative motion (μm)			
	1 st week	3 rd week	6 th week	8 th week
SS	2.17	1.41	1.41	1.40
Ti	2.66	1.54	1.54	1.54

As can be seen in table 4.3, the magnitude of relative motion in the contact area for SS plate model was 2.17 μm during the 1st week of healing, which reduced by 35% to 1.41 μm in the 3rd week, then stayed steady for the rest of the healing period. In the case of the Ti plate model the reduction was 42%.

4.2 Load case 2 – pure tension

As mentioned in the previous chapter, a 226 N tensile load was applied. The following sections describe the stress distribution in each of the components and a summary table is presented at the end.

4.2.1 Stress distribution in the bone: pure tension case

The maximum equivalent von-Mises stress in bone with the SS and Ti plates during the 1st week of healing was 10.9 MPa and 9.9 MPa, respectively. In the 3rd week of healing, the magnitude of this stress in bone with the SS plate decreased to 8.8 MPa and to 9.3 MPa with the Ti plate. During the following weeks of healing, this magnitude remained constant. It is evident from table 4.4 that, except for the 1st week of healing, bone fixed with the Ti plate transmits a larger portion of the load compared to bone with the SS plate.

For the model with the SS plate, the maximum equivalent von-Mises stress occurred in the 4th screw hole near the fracture gap. This location with the Ti plate was in the 6th screw hole in the distal humerus. Figure 4.13 illustrates the stress distribution in the bone with a SS plate in the 1st week of healing, while figure 4.14 shows the same but with the Ti plate. The stress shielding effect throughout the bone is clearly presented.

Equivalent Stress - Bone

Type: Equivalent (von-Mises) Stress
Unit: Pa
Time: 1
01/03/2008 6:12 PM

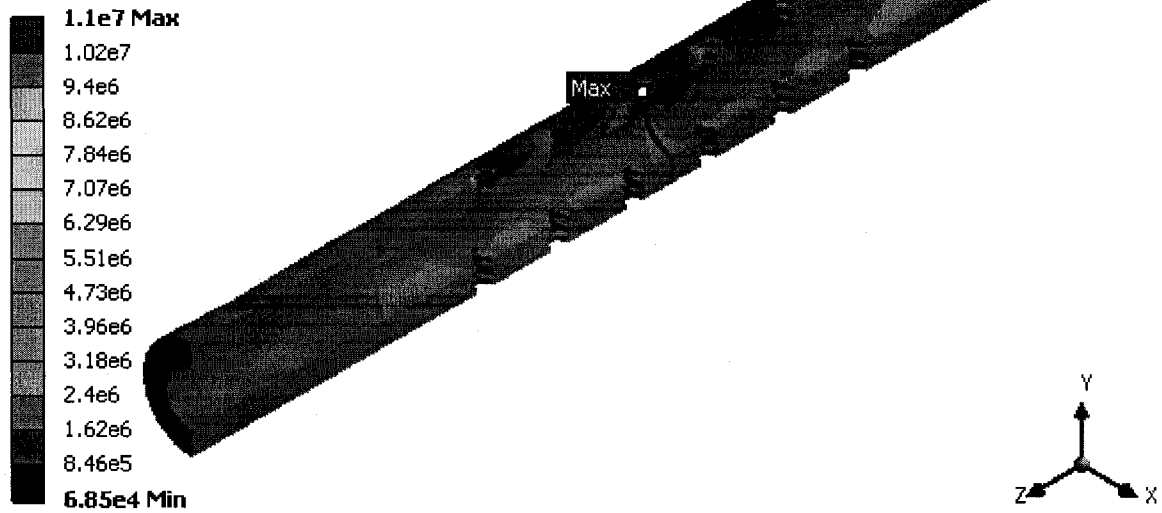


Figure 4.13: Stress distribution in bone with the SS fracture plate for the 1st week of healing

Equivalent Stress - Bone

Type: Equivalent (von-Mises) Stress
Unit: Pa
Time: 1
01/03/2008 6:15 PM

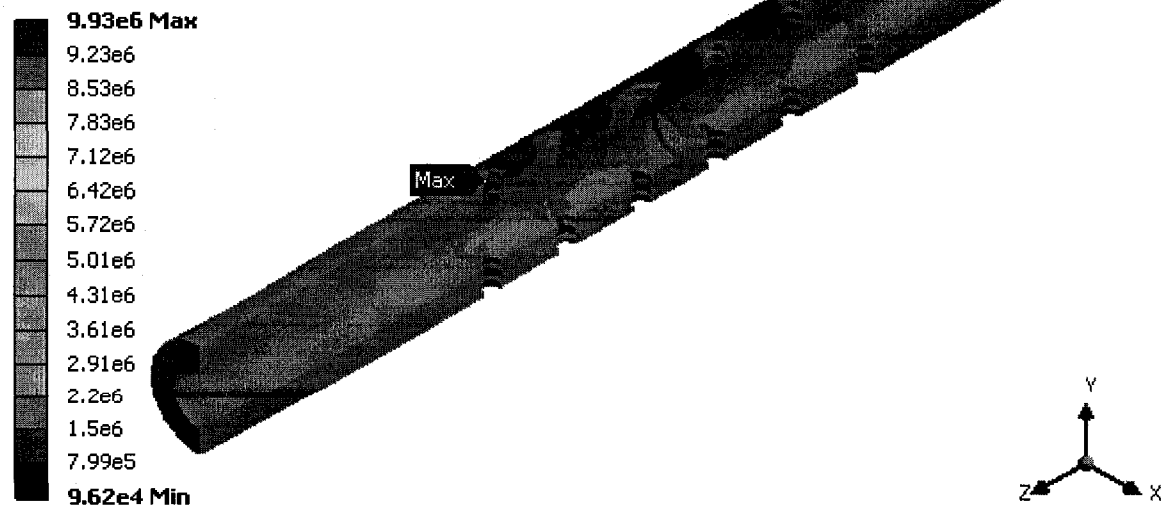


Figure 4.14: Stress distribution in bone with the Ti fracture plate for the 1st week of healing

4.2.2 Stress distribution in the plate: pure tension case

The maximum equivalent von-Mises stress in the fracture plate followed the same pattern as shown in load case 1. As mentioned before, the fracture plate is fixed to the bone using screws. When a tensile load is applied to the bone, the fracture gap may open up. However, the screws transfer the load to the rigid plate, which prevents the gap from opening.

The maximum equivalent von-Mises stress during the 1st week of healing in the SS fracture plate was 100.1 MPa while this was 61.7 in the Ti plate. In the 3rd week of healing, the magnitude of the maximum equivalent stress reduced to 17.3 MPa and stayed steady for the rest of the period. This trend was the same for the Ti plate, where the amount of the maximum equivalent stress reduced to 13.1 MPa. The maximum equivalent von-Mises stress in both the SS and Ti plates during the 1st week of healing occurred at the interface of plate and bone in the fracture gap (figure 4.15). However, this location changed in the following weeks and transferred to the interface of the 6th screw and the hole in the distal humerus (figure 4.16).



Figure 4.15: Stress distribution in the SS plate for the 1st of week of healing

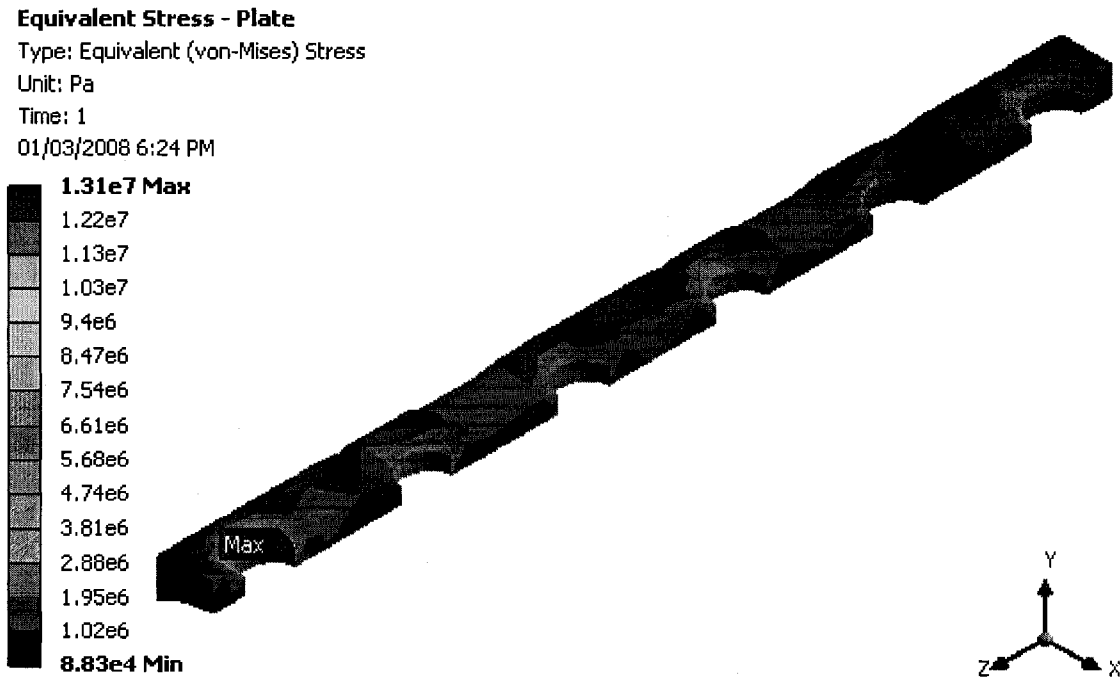


Figure 4.16: Stress distribution in the SS plate for the 3rd week of healing

4.2.3 Stress distribution in the screws: pure tension case

The maximum equivalent von-Mises stress in the stainless steel screws reduced from 152.3 MPa in the 1st week to 26.4 MPa in the 3rd week of healing and remained constant during the following weeks of healing. For the titanium screws, the maximum equivalent von-Mises stress decreased from 89.9 MPa in the 1st week to 19.4 MPa in the 3rd week and stayed steady during the following weeks of healing.

The maximum equivalent stress in both the stainless steel and titanium screws during the 1st week of healing happened in the 3rd screw located in the proximal humerus close to the fracture gap (figure 4.17). On the other hand, for both plates, the majority of transferred load from the bone to the plate occurred at the 1st screw in proximal humerus for the rest of the healing period (figure 4.18).

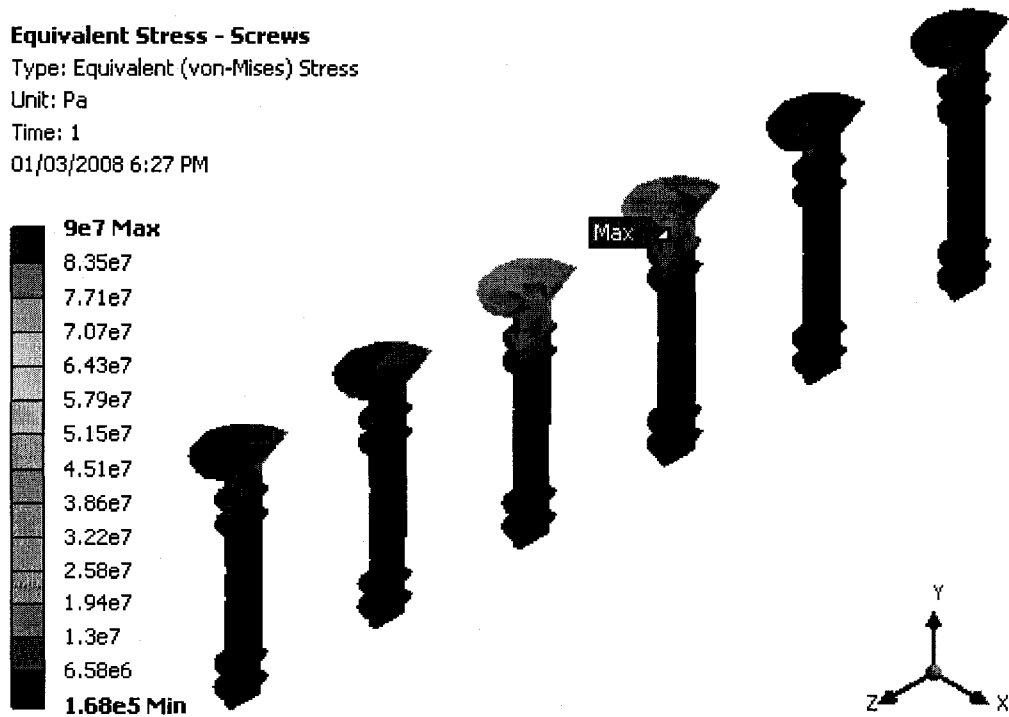


Figure 4.17: Stress distribution in the titanium screws for the 1st week of healing

Equivalent Stress - Screws

Type: Equivalent (von-Mises) Stress
Unit: Pa
Time: 1
01/03/2008 6:29 PM

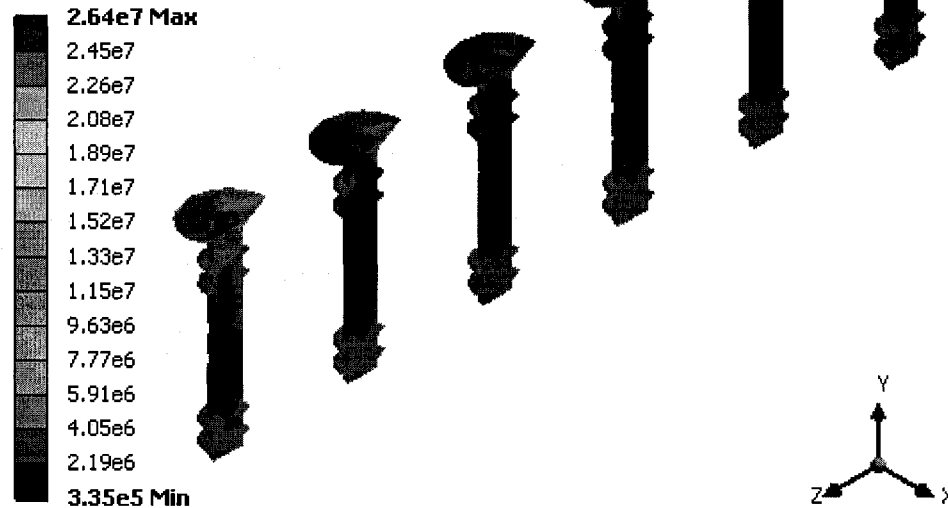
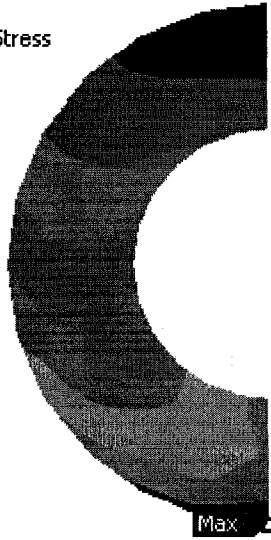
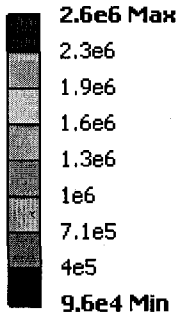


Figure 4.18: Stress distribution in the stainless steel screws for the 3rd week of healing

4.2.4 Stress distribution in the callus: pure tension case

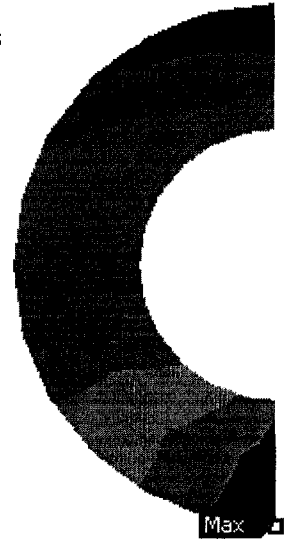
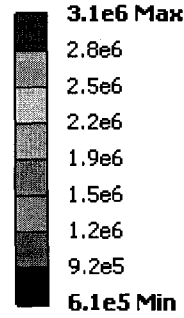
When the Ti plate is used, the maximum equivalent von-Mises stress in the callus during the 1st week of healing was 2.6 MPa and occurred at the bottom of the bone, farthest away from the bone. In the 3rd week of healing, this maximum equivalent stress increased by 20% to 3.1 MPa. This means that a larger portion of load is transmitted through the newly-formed callus. The magnitude of this stress in the 6th and 8th week of healing was 3.4 MPa and 3.7 MPa, respectively. Figure 4.19 shows the stress distribution in the callus at different stages of healing in case of the Ti plate. The same behavior in the callus is observed if a SS plate is used.

Equivalent Stress - Call
 Type: Equivalent (von-Mises) Stress
 Unit: Pa
 Time: 1
 06/02/2008 8:28 PM



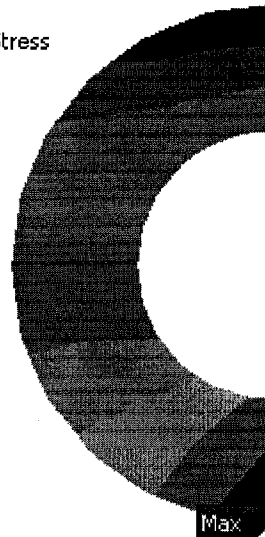
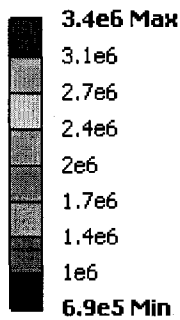
1st week

Equivalent Stress - Callus
 Type: Equivalent (von-Mises) Stress
 Unit: Pa
 Time: 1
 06/02/2008 8:30 PM



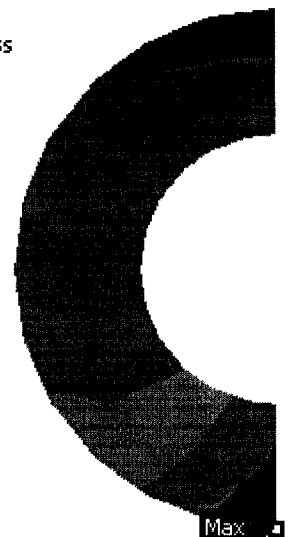
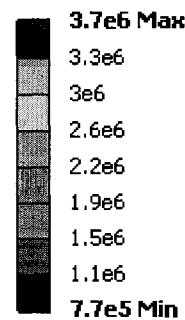
3rd week

Equivalent Stress - Callus
 Type: Equivalent (von-Mises) Stress
 Unit: Pa
 Time: 1
 06/02/2008 8:32 PM



6th week

Equivalent Stress - Callus
 Type: Equivalent (von-Mises) Stress
 Unit: Pa
 Time: 1
 06/02/2008 8:33 PM



8th week

Figure 4.19: Stress distribution in the callus at different stages of healing in case of a Ti plate

4.2.5 Summary and discussion of the stresses: pure tension case

Table 4.4 provides the magnitude of the maximum equivalent von-Mises stress in each of the parts, namely bone, fracture plate, screws and callus at different stages of fracture healing.

Table 4.4: Maximum equivalent von-Mises stresses in different parts of the assembly

		Maximum equivalent stress (MPa)			
		1 st week	3 rd week	6 th week	8 th week
Bone	SS	10.9	8.8	8.8	8.8
	Ti	9.9	9.3	9.3	9.3
Plate	SS	100.1	17.3	17.3	17.3
	Ti	61.7	13.1	13.1	13.1
Screw	SS	152.3	26.4	26.3	26.3
	Ti	89.9	19.4	19.4	19.4
Callus	SS	2.3	3.3	3.6	3.9
	Ti	2.6	3.1	3.4	3.7

In the pure tension load case, the majority of the load transfers through the fracture plate and screws. Also, the screws always carry a higher load compared to the fracture plate. Since the stainless steel has a higher Young's modulus compared to the titanium alloy, a greater portion of load transfers through the stainless steel components of the assembly. In other words, the bone with the Ti fracture plate and screws transfers a greater portion of load compared to the bone with the SS plate and screws. Bone, plate and screws all exhibit the same behavior that there is no change in the maximum stress after the 3rd week of healing.

4.2.6 Elastic strains: pure tension case

The equivalent von-Mises elastic strains in these models follows the same patterns as shown in the pure compression case. Due to the low Young's modulus of callus in the assembly during the healing process, and also due to the location of the fracture plate, the maximum equivalent von-Mises elastic strain is always in the fracture

gap, farthest away from the fracture plate. Table 4.5 presents the amounts of these elastic strains in the assembly.

Table 4.5: Maximum equivalent elastic von-Mises strains in different parts of the assembly

		Maximum equivalent elastic strain			
		1 st week	3 rd week	6 th week	8 th week
Bone	SS	0.12	0.00048	0.00048	0.00048
	Ti	0.13	0.0005	0.0005	0.0005
Plate	SS	0.00052	0.00009	0.0009	0.0009
	Ti	0.00094	0.00014	0.00014	0.00014
Screw	SS	0.00079	0.00014	0.00014	0.00014
	Ti	0.00094	0.0020	0.0020	0.0020
Callus	SS	0.12	0.00038	0.00028	0.00023
	Ti	0.13	0.00036	0.00026	0.00021

4.2.7 Contact analysis of the bone-plate interface: pure tension case

Similar to the pure compression load case, there exists frictional contact at the interface of the bone and the fracture plate. As a result, there is relative motion between the bone and the fracture plate. In the 1st week of healing, the maximum sliding between the SS fracture plate and the bone occurred at the proximal end of contact area (figure 4.20). This location for the Ti fracture plate was at the distal end of the contact area (figure 4.21). Figure 4.22 illustrates the contact at the bone and the SS plate interface in the 3rd week of healing.

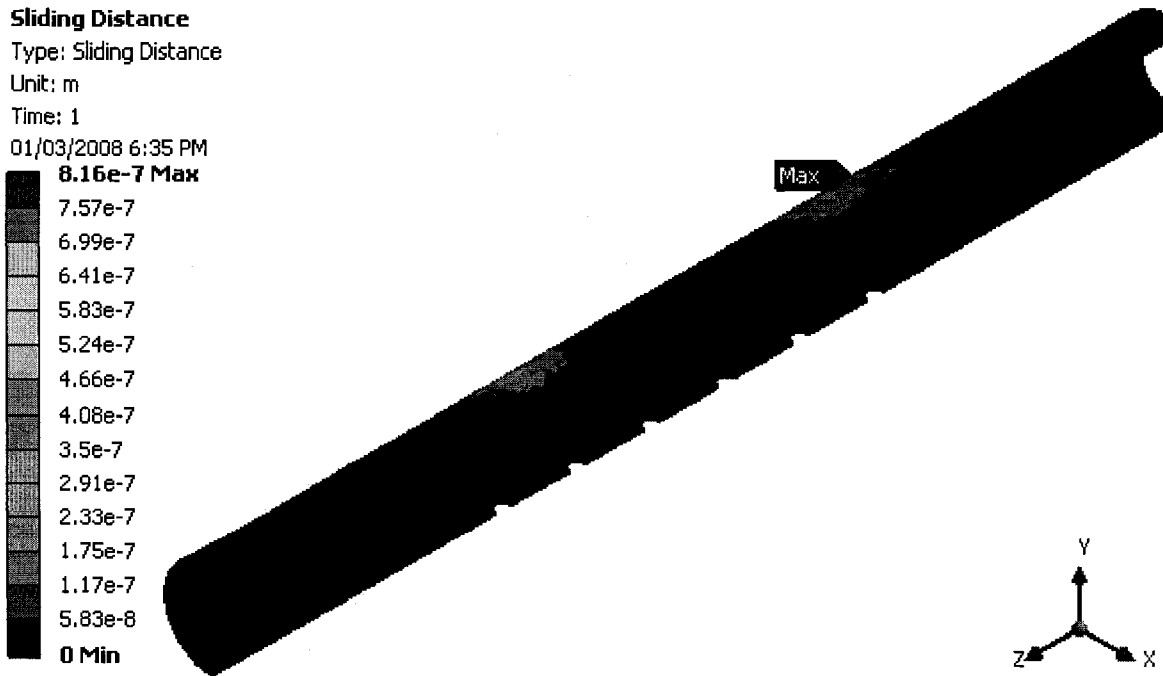


Figure 4.20: Relative motion between the bone and the SS plate for the 1st week of healing

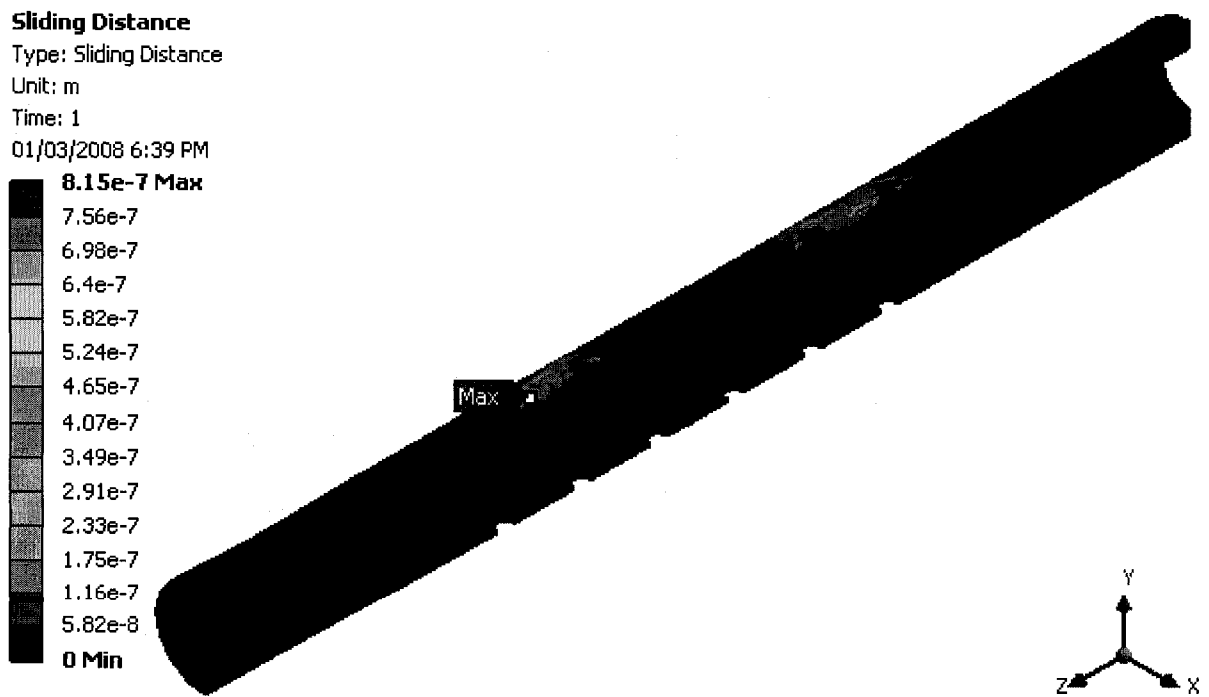


Figure 4.21: Relative motion between the bone and the Ti plate for the 1st week of healing

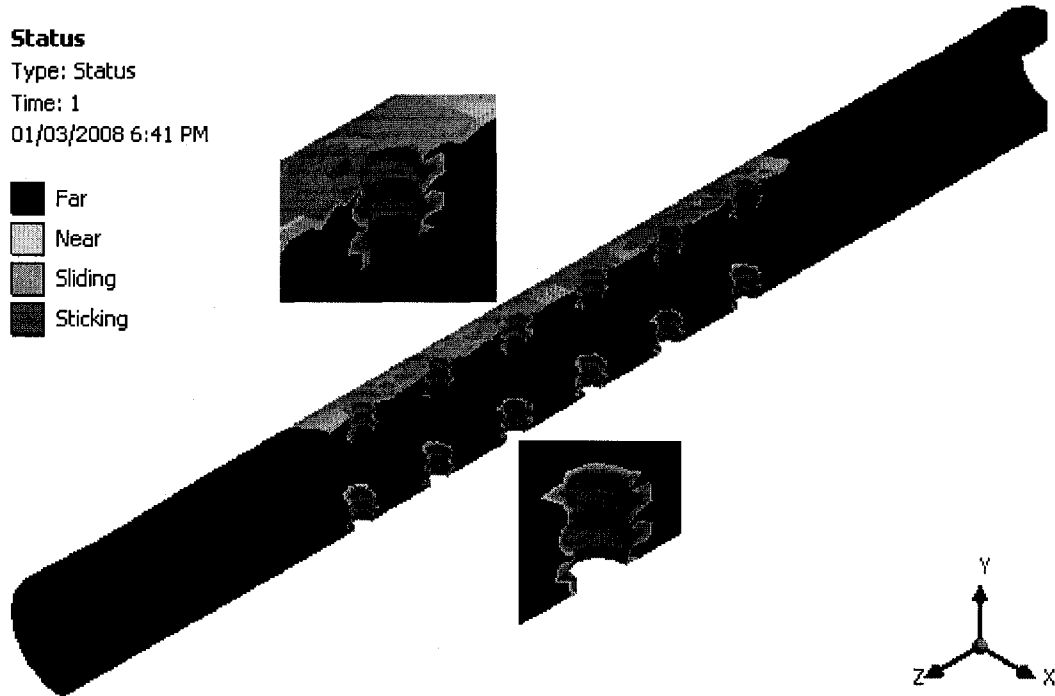


Figure 4.22: Contact at the bone and the SS plate interface for the 3rd week of healing

The magnitude of these relative motions during the rest of the healing process is presented in table 4.6.

Table 4.6: Maximum relative motions at the bone and the fracture plate interface

	Maximum relative motion (μm)			
	1 st week	3 rd week	6 th week	8 th week
SS	81.6	55.6	55.6	55.6
Ti	81.4	71.1	71.1	71.1

As can be seen in table 4.6, the magnitude of relative motion in the contact area for SS plate model was 81.6 μm during the 1st week of healing and reduced by 31.9% to 55.6 μm in the 3rd week, then stayed steady for the rest of the healing period. In the case of the Ti plate model, the reduction was 12.7%

4.3 Load case 3 – combined compression and shear force

In this case, a compressive force in combination with a shear force, which generates a bending moment, was applied to two models. The magnitude of the applied loads is presented in table 4.7 where α is the angle between the upper and lower arms with the vertical. This means that the elbow angle is $180^\circ - 2\alpha$.

Table 4.7: Compressive and shear forces

α (degree)	45°	30°	15°	0°
F_C (N)	-199.4	-244.2	-272.4	-282.0
F_T (N)	-199.4	-141.0	-73.0	0.0

Unlike the previous load cases, the results of this load case were categorized for each of the SS and Ti plates with respect to various α .

4.3.1 Assembly with the stainless steel plate

The following sections describe the stress distribution in each of the components in model with the SS plate and screws. A summary table and comparison of the assemblies with the SS and Ti plates is presented in section 4.4.

4.3.1.1 Stress distribution in the bone: compression and shear case

Figure 4.23 shows a typical stress distribution for $\alpha=45^\circ$ in the 3rd week of healing. As can be seen from the figure, the maximum von-Mises stress occurs directly under the plate at the 1st screw.

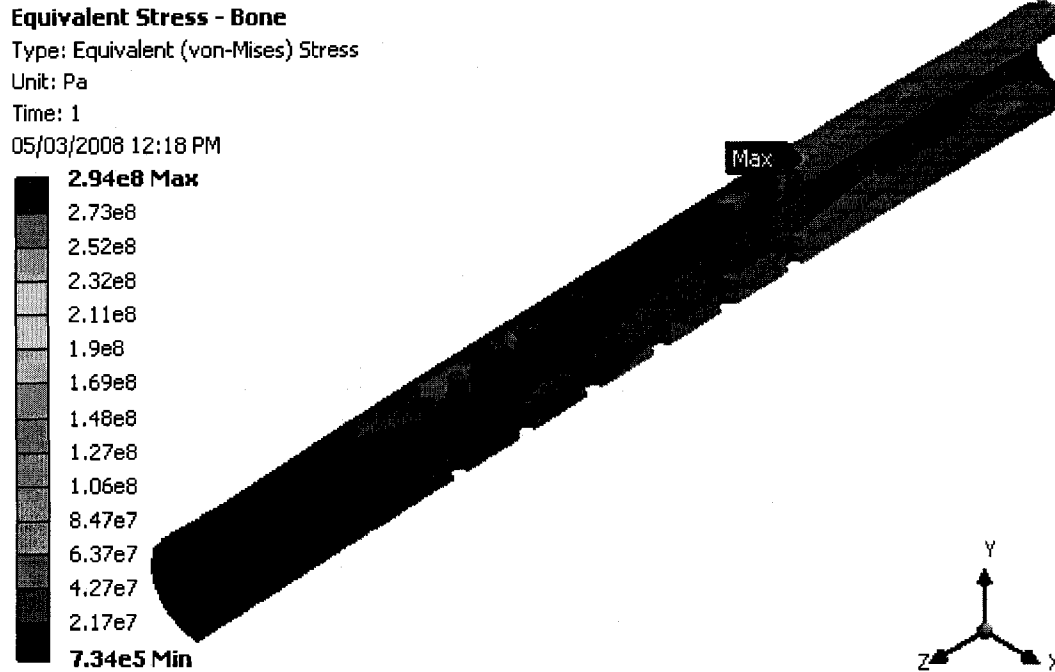


Figure 4.23: Stress distribution in the bone for the 3rd week of healing (SS, $\alpha=45^\circ$)

When α decreases, the maximum equivalent von-Mises stress in the bone declines. The largest value of the equivalent von-Mises stress in the bone occurs in the 1st week for $\alpha=45^\circ$. Table 4.8 below shows how these stresses change with varying angles and at different stages of healing.

Table 4.8: Maximum equivalent von-Mises stresses in the bone at different stages of healing

α (degree)	Maximum equivalent stress (MPa)			
	1 st week	3 rd week	6 th week	8 th week
45°	339.3	294.4	294.4	294.2
30°	236.0	203.1	203.0	202.9
15°	116.1	98.3	98.2	98.2

4.3.1.2 Stress distribution in the SS plate: compression and shear case

Figure 4.24 shows the stress distribution in the stainless steel plate during the 1st week of healing with $\alpha=45^\circ$.

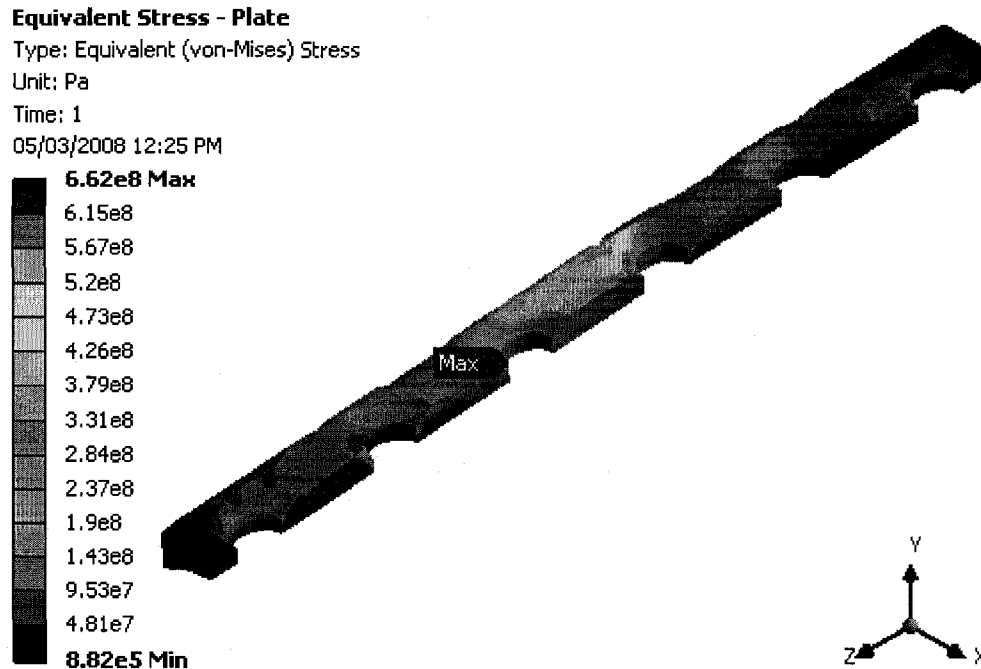


Figure 4.24: Stress distribution in the SS fracture plate for the 1st week of healing ($\alpha=45^\circ$)

The highest stresses occur in the section of plate closest to the fracture gap. The maximum equivalent von-Mises stress occurred at the interface of the 4th screw and the hole. In the 3rd week of healing and thereafter the stresses in the middle of the plate decrease while those at the ends increase and the maximum stress location shifted to the 1st hole (figure 4.25). The same behavior was observed for $\alpha=30^\circ$ and $\alpha=15^\circ$.

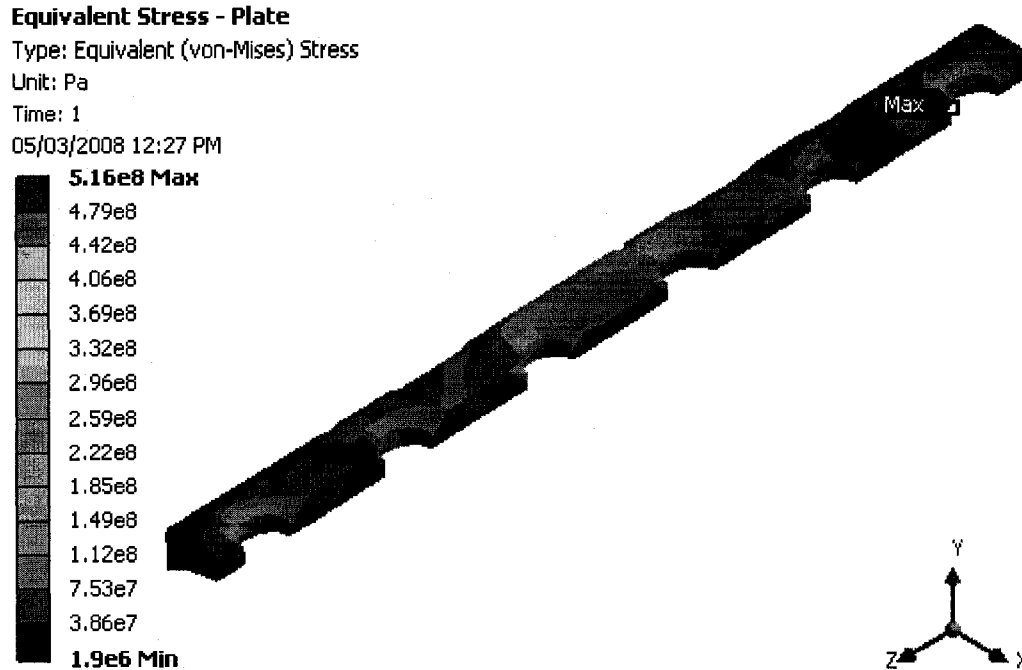


Figure 4.25: Stress distribution in the SS fracture plate for the 3rd week of healing ($\alpha=45^\circ$)

Table 4.9 shows the maximum equivalent von-Mises stresses in the SS plate at different stages of healing.

Table 4.9: Maximum equivalent von-Mises stresses in the SS plate at different stages of healing

α (degree)	Maximum equivalent stress (MPa)			
	1 st week	3 rd week	6 th week	8 th week
45°	661.9	515.8	515.9	515.7
30°	492.2	361.9	361.7	361.5
15°	307.4	182.5	182.4	182.4

The maximum equivalent von-Mises stress, 661.9 MPa for $\alpha= 45^\circ$ during the 1st week of healing, is almost 11.5% more than the ultimate strength of stainless steel (586 MPa) and is likely to result in failure. Therefore, excessive loading should be avoided to prevent possible failure during the 1st week of healing. Please note that the ultimate strength of

the screw is also exceeded in this case, as is shown in the next section. The high stresses, also result in comparatively high deflections, especially for $\alpha=45^\circ$ (table 4.10)

Table 4.10: Maximum deflections in the SS fracture plate

α (degree)	Maximum deflection (mm)			
	1 st week	3 rd week	6 th week	8 th week
45°	5.3	3.7	3.7	3.7
30°	3.9	2.7	2.7	2.7
15°	2.2	1.4	1.4	1.4

The results show that by reducing the α , the maximum deflection of the fracture plate decreases as well.

4.3.1.3 Stress distribution in the SS screws: compression and shear case

Figure 4.26 shows the stress distribution in the stainless steel screws during the 1st week of healing with $\alpha=45^\circ$.

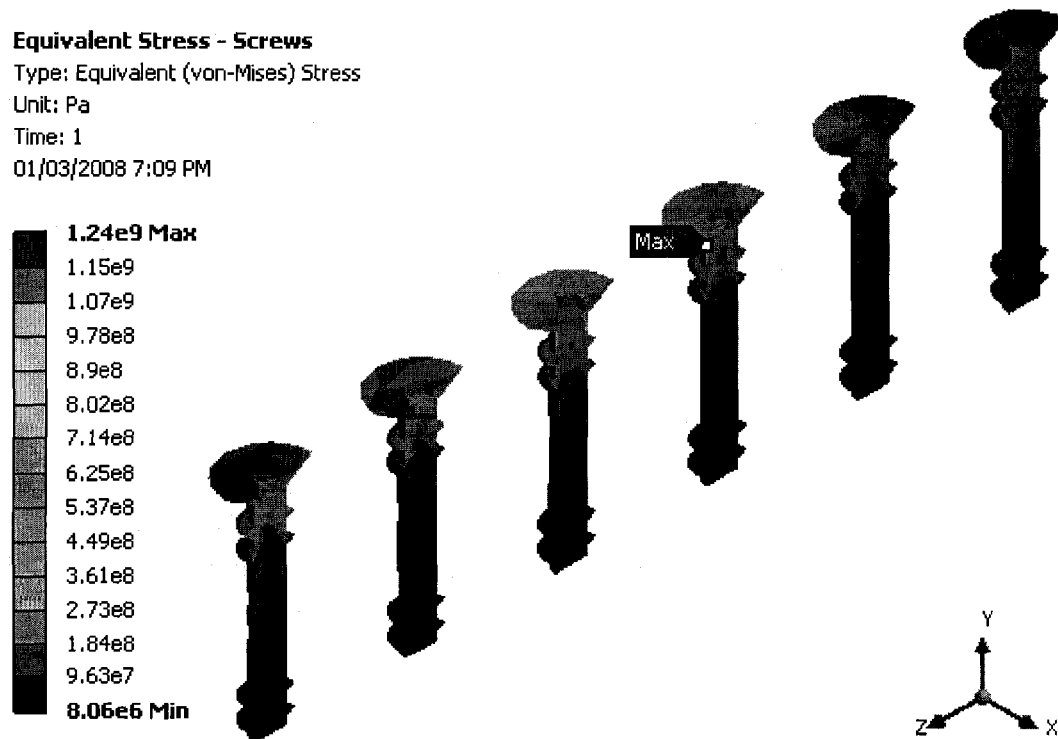


Figure 4.26: Stress distribution in the stainless steel screws for the 1st week of healing ($\alpha=45^\circ$)

The maximum equivalent von-Mises stress occurred at the interface of the 3rd screw and the hole. In the 3rd week of healing and thereafter the stresses in the middle screws decrease while those at the proximal end increase (figure 4.27). The same happens when $\alpha=30^\circ$ and $\alpha=15^\circ$.

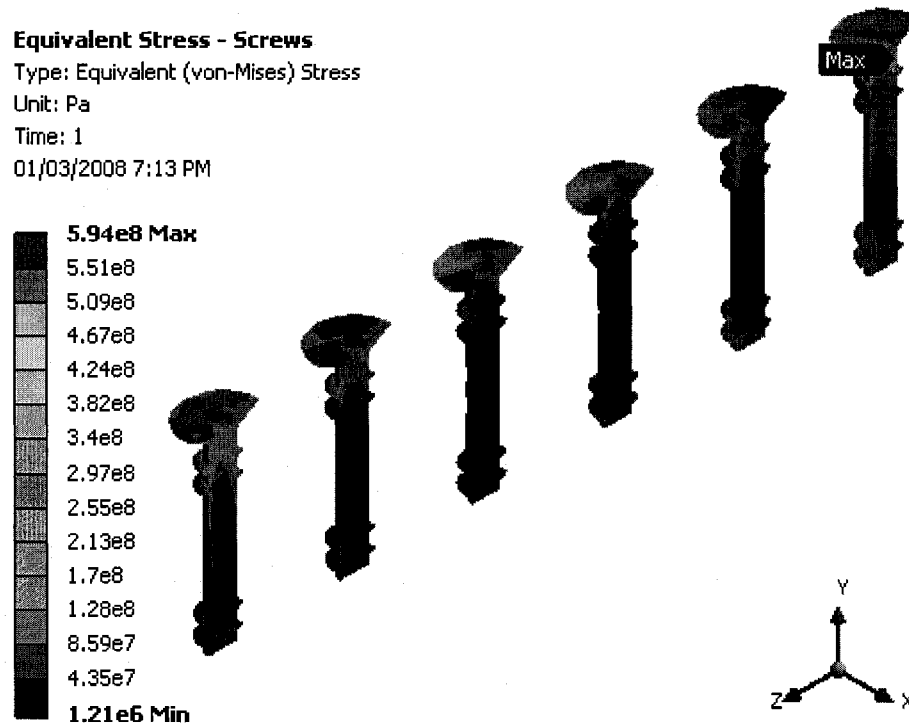


Figure 4.27: Stress distribution in the stainless steel screws for the 3rd week of healing ($\alpha=45^\circ$)

The maximum stresses in the screws occur in the same location as in the plates. Table 4.11 shows the maximum equivalent von-Mises stresses in the stainless steel screws at different stages of healing.

Table 4.11: Maximum equivalent von-Mises stresses in the screws at different stages of healing

α (degree)	Maximum equivalent stress (MPa)			
	1 st week	3 rd week	6 th week	8 th week
45°	1242.7	593.7	593.6	593.3
30°	932.2	409.4	409.2	409.0
15°	553.5	198.0	197.9	197.9

The maximum equivalent von-Mises stress for $\alpha= 45^\circ$ are always more than the ultimate strength of stainless steel (586 MPa) and may result in failure. Therefore, excessive loading should be avoided. The same scenario is also valid during the 1st week of healing for $\alpha=30^\circ$. As is shown in the table 4.11, for $\alpha=15^\circ$, there is no excessive force in the assembly during the healing period.

4.3.1.4 Stress distribution in the callus: compression and shear case

In the model with the stainless steel plate, the maximum equivalent von-Mises stress in the callus increased from 22.9 MPa in the 1st week to 38.2 MPa in the 3rd week of healing for $\alpha=45^\circ$, an increase of 40%. This stress continued to increase, but at a smaller rate reaching a maximum of 45.2 MPa. The same trend was observed for $\alpha=30^\circ$ and $\alpha=15^\circ$ as shown in table 4.12 below.

Table 4.12: Maximum equivalent von-Mises stresses at different stages of healing

α (degree)	Maximum equivalent stress (MPa)			
	1 st week	3 rd week	6 th week	8 th week
45°	22.9	38.2	41.9	45.2
30°	17.0	28.2	30.9	33.9
15°	9.9	16.5	18.0	19.6

4.3.1.5 Elastic strain: compression and shear case

Due to the low Young's modulus of the callus in the assembly during the healing process, and also due to the location of the fracture plate, the maximum equivalent von-Mises elastic strain is at the bottom side of the bone, farthest away from the plate. Table 4.13 presents the amounts of these elastic strains in the assembly.

Table 4.13: Maximum equivalent elastic von-Mises strains in different parts of the assembly

	α (degree)	Maximum equivalent strain			
		1 st week	3 rd week	6 th week	8 th week
Bone	45°	1.14	0.016	0.016	0.016
	30°	0.85	0.0011	0.0011	0.0011
	15°	0.49	0.0052	0.0052	0.0052
Plate	45°	0.0034	0.0027	0.0027	0.0027
	30°	0.0026	0.0019	0.0019	0.0019
	15°	0.0016	0.0009	0.0009	0.0009
Screw	45°	0.0064	0.0031	0.0031	0.0031
	30°	0.0048	0.0021	0.0021	0.0021
	15°	0.0029	0.0010	0.0010	0.001
Callus	45°	1.14	0.0044	0.0032	0.0026
	30°	0.85	0.0033	0.0024	0.0019
	15°	0.5	0.0019	0.0014	0.0011

Section 4.4 presents a comparison and discussion of the assembly with the SS plate and the Ti plate.

4.3.1.6 Contact analysis at the bone-SS plate interface: compression and shear case

There exists frictional contact, sliding, at the interface of the bone and the fracture plate (figure 4.28).

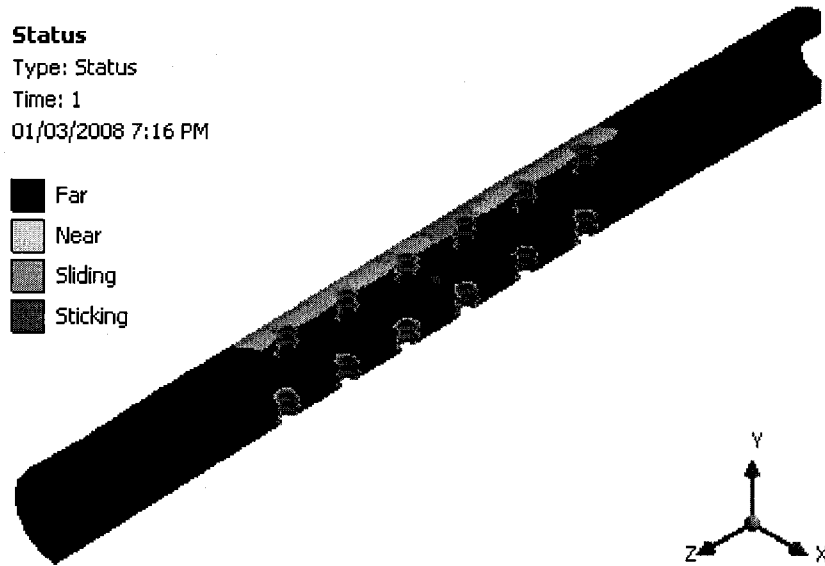


Figure 4.28: Contact at the bone and the SS fracture plate interface for the 3rd week of healing ($\alpha=30^\circ$)

In the 1st week of healing for $\alpha=15^\circ$, the maximum sliding between the bone and the fracture plate occurred in the callus (figure 4.29).

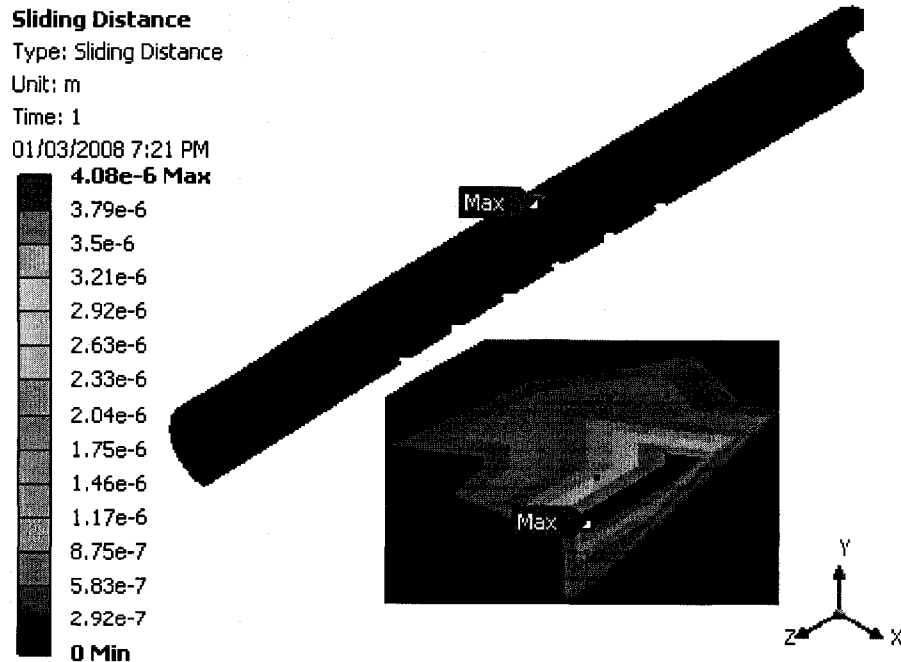


Figure 4.29: Relative motion between the bone and the fracture plate for the 1st week of healing ($\alpha=15^\circ$)

For the rest of the healing period, this location was at the 5th screw hole close to the lateral edge of the fracture plate (figure 4.30).

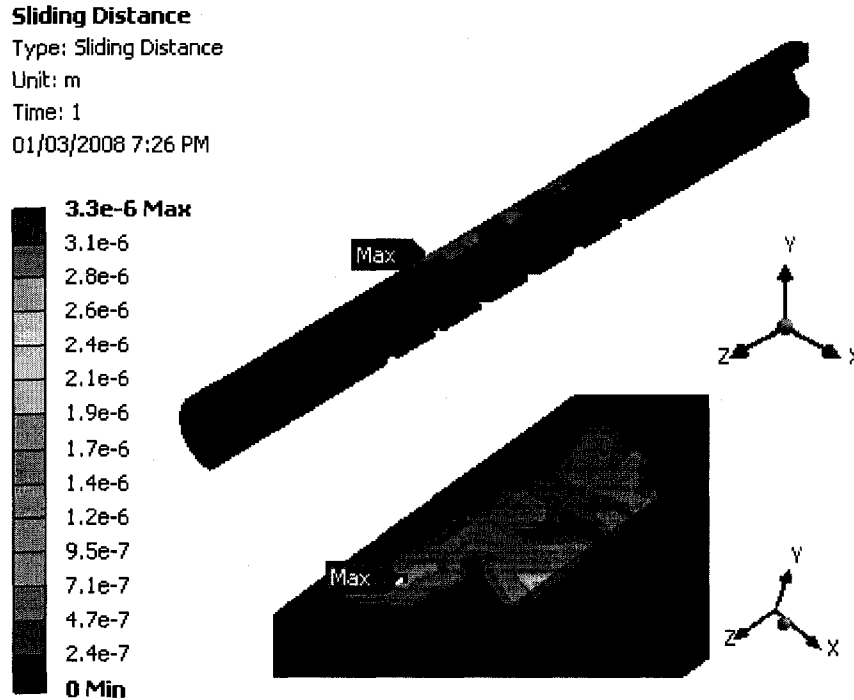


Figure 4.30: Relative motion between the bone and the fracture plate for the 6th week of healing ($\alpha=15^\circ$)

The magnitude of these relative motions during the healing process for various angles is provided in table 4.14.

Table 4.14: Maximum relative motions at the bone - SS plate interface

α (degree)	Maximum relative motion (μm)			
	1 st week	3 rd week	6 th week	8 th week
45°	1.22	3.04	4.79	4.82
30°	1.88	2.69	3.19	3.56
15°	4.08	3.33	3.31	3.30

As presented in the table, the maximum relative motion increases with the healing period for $\alpha=45^\circ$ and $\alpha=30^\circ$. The reverse is true for $\alpha=15^\circ$.

4.3.2 Assembly with the titanium plate

The following sections describe the stress distribution in each of the components in the model with the titanium plate and screws. A summary table and comparison of the assemblies with the SS and Ti plates is presented in section 4.4.

4.3.2.1 Stress distribution in the bone: compression and shear case

Figure 4.31 shows a typical stress distribution for $\alpha=45^\circ$ in the 3rd week of healing. As can be seen from the figure, the maximum stress occurs directly under the plate at the 1st screw.

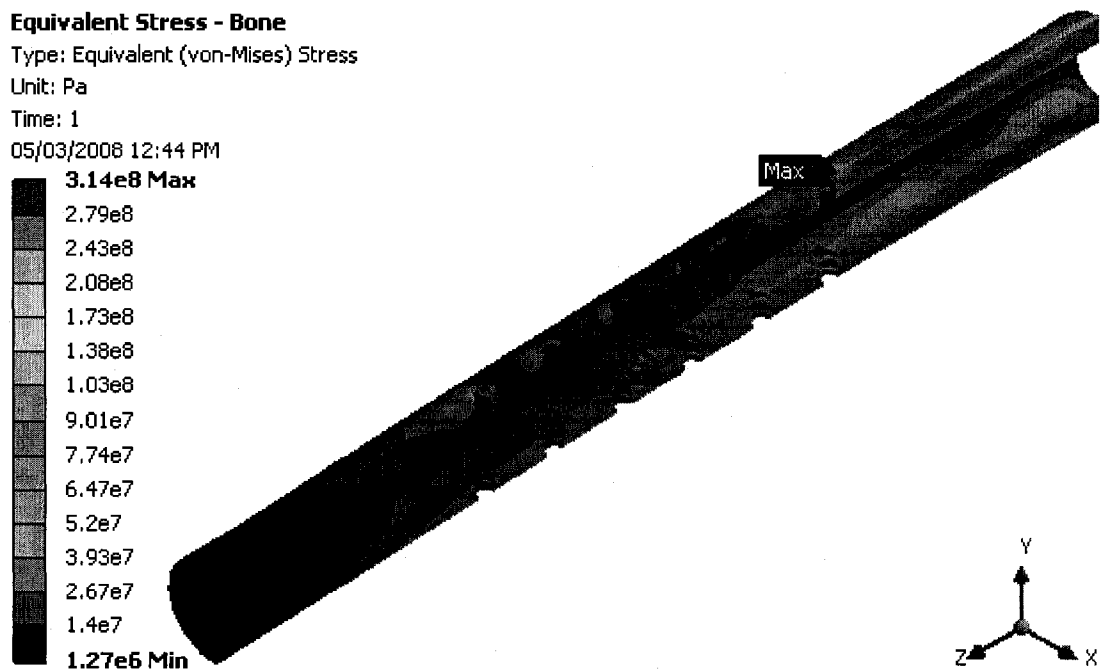


Figure 4.31: Stress distribution in the bone for the 3rd week of healing ($\alpha=45^\circ$)

When α decreases, the maximum equivalent von-Mises stress in the bone declines. The largest value of the equivalent von-Mises stress in the bone occurs in the 1st week for $\alpha=45^\circ$. Table 4.15 below shows how these stresses change with varying angles

and at different stages of healing. All stresses are well below the ultimate strength of Ti-6Al-4V (1080 MPa).

Table 4.15: Maximum equivalent von-Mises stresses in the bone at different stages of healing

α (degree)	Maximum equivalent stress (MPa)			
	1 st week	3 rd week	6 th week	8 th week
45°	361.8	313.7	313.3	313.1
30°	250.2	216.4	216.2	216.1
15°	120.7	104.6	104.6	104.6

4.3.2.2 Stress distribution in the Ti plate: compression and shear case

Figure 4.32 shows the stress distribution in the titanium plate during the 1st week of healing with $\alpha=15^\circ$

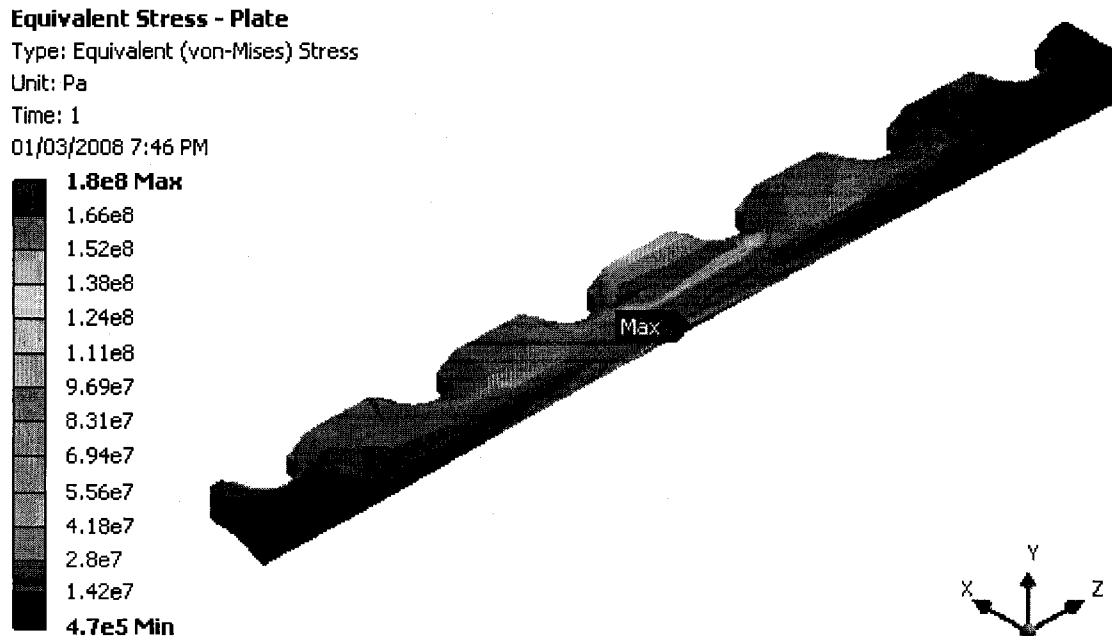


Figure 4.32: Stress distribution in the Ti fracture plate for the 1st week of healing ($\alpha=15^\circ$)

The highest stresses occur in the section of plate closest to the fracture gap. The maximum equivalent von-Mises stress occurred at the interface of the bone and the fracture plate underneath the fracture plate. Figure 4.33 shows the stress distribution in the titanium plate during the 1st week of healing with $\alpha=30^\circ$.

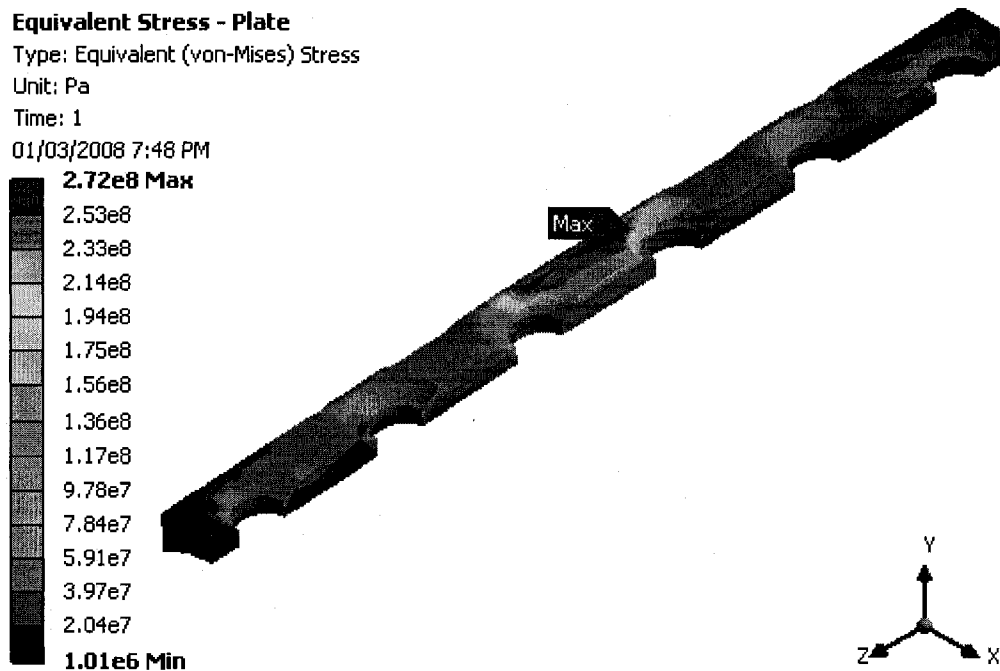


Figure 4.33: Stress distribution in the Ti fracture plate for the 1st week of healing ($\alpha=30^\circ$)

The highest stresses occur in the section of plate closest to the fracture gap. The maximum equivalent von-Mises stress occurred at the interface of 3rd screw and the hole further to the edge of the fracture plate

Figure 4.34 shows the stress distribution in the titanium plate during the 1st week of healing with $\alpha=45^\circ$

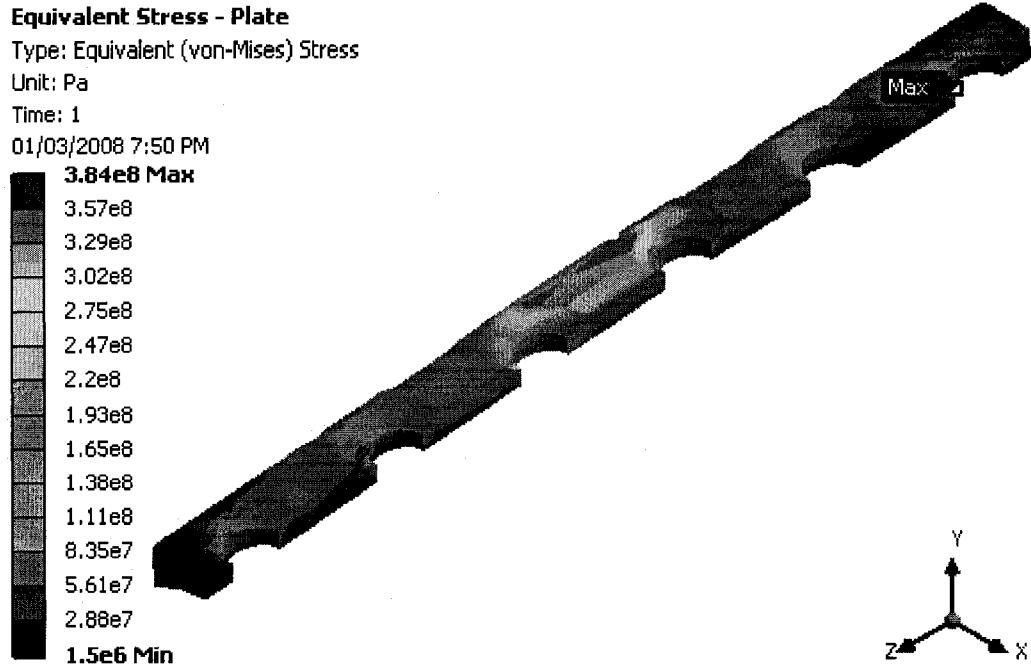


Figure 4.34: Stress distribution in the Ti fracture plate for the 1st week of healing ($\alpha=45^\circ$)

There is a region of high stresses at the middle of the plate. The maximum equivalent von-Mises stress occurred at the interface of 1st screw and the hole. Table 4.16 shows the maximum equivalent von-Mises stresses in the Ti plate at different stages of healing.

Table 4.16: Maximum equivalent von-Mises stresses in the Ti plate at different stages of healing

α (degree)	Maximum equivalent stress (MPa)			
	1 st week	3 rd week	6 th week	8 th week
45°	384.1	379.6	379.1	378.8
30°	271.9	266.3	266.0	265.8
15°	179.6	135.0	135.0	135.0

The stresses result in comparatively high deflections in the plate, especially for $\alpha=45^\circ$ (table 4.17)

Table 4.17: Maximum deflections in the Ti fracture plate

α (degree)	Maximum deflection (mm)			
	1 st week	3 rd week	6 th week	8 th week
45°	5.6	3.9	3.9	3.9
30°	4.1	2.7	2.7	2.7
15°	2.3	1.4	1.4	1.4

The results show that by reducing the α , the maximum deflection of the fracture plate decreases as well.

4.3.2.3 Stress distribution in the Ti screws: compression and shear case

The maximum equivalent von-Mises stress in titanium screws reduced from 697.8 MPa in the 1st week to 419.3 MPa in the 3rd week of healing for $\alpha=45^\circ$ and remained constant within the following weeks of healing. The same trend was observed for $\alpha=30^\circ$ and $\alpha=15^\circ$ as shown in the table 4.18 below.

Table 4.18: Maximum equivalent von-Mises stresses in the screws at different stages of healing

α (degree)	Maximum equivalent stress (MPa)			
	1st week	3rd week	6th week	8th week
45°	697.8	419.3	418.6	418.2
30°	515.9	295.1	294.7	294.3
15°	297.3	151.6	151.6	151.6

4.3.2.4 Stress distribution in the callus: compression and shear case

In the model with the titanium alloy, the maximum equivalent von-Mises stress in the callus increased from 24.7 MPa in the 1st week to 41.2 MPa in the 3rd week of healing for $\alpha=45^\circ$, an increase of 40%. This stress continued to increase, but at a smaller rate reaching a maximum of 48.9 MPa. The same trend was observed for $\alpha=30^\circ$ and $\alpha=15^\circ$ as shown in the table 4.19 below.

Table 4.19: Maximum equivalent von-Mises stresses in the callus at different stages of healing

α (degree)	Maximum equivalent stress (MPa)			
	1 st week	3 rd week	6 th week	8 th week
45°	24.7	41.2	45.2	48.9
30°	18.4	30.4	33.4	36.0
15°	10.8	17.6	19.2	20.8

Figure 4.35 depicts the stress distribution in the callus at the different stages of healing in the case of a Ti plate.

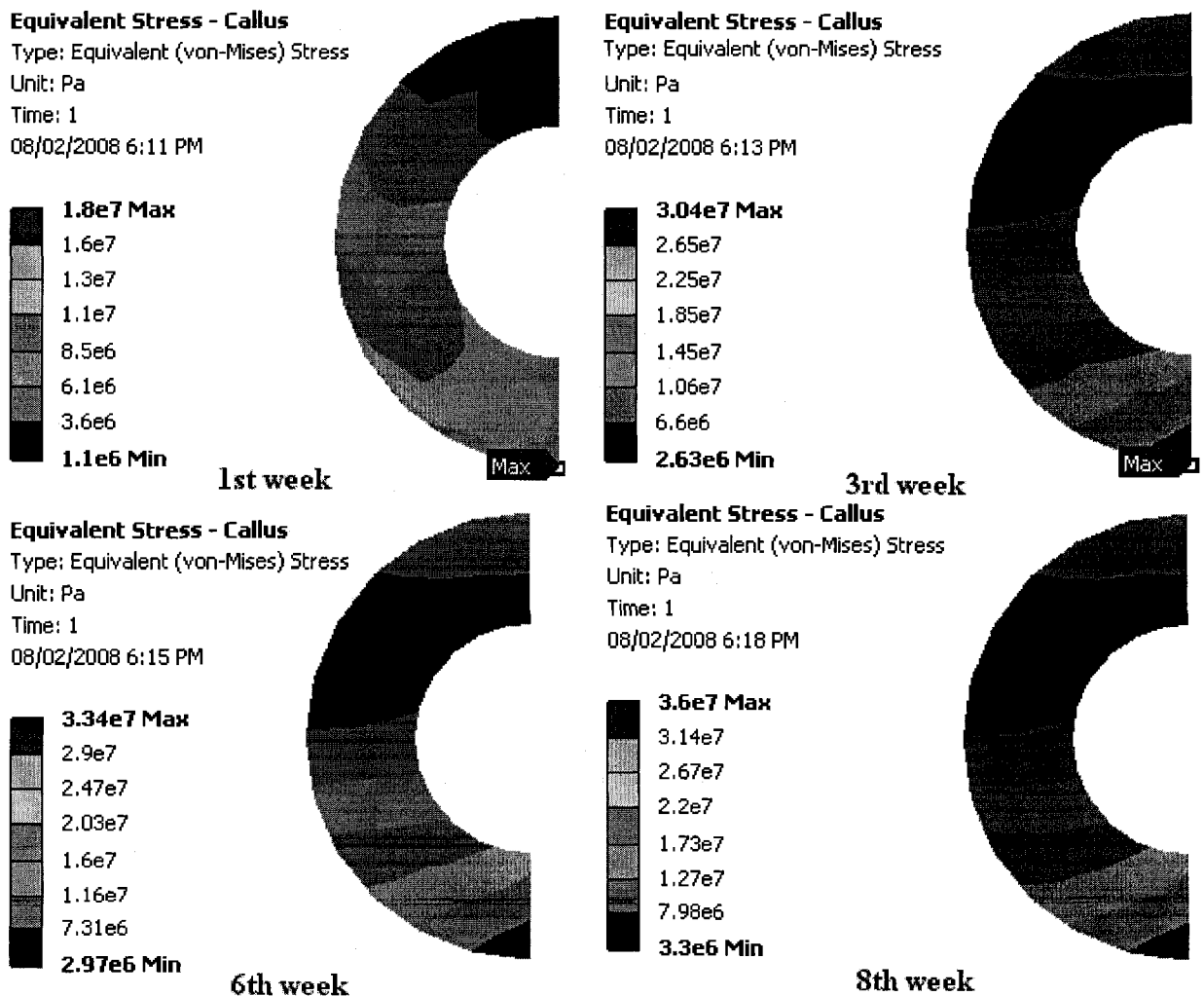


Figure 4.35: Stress distribution in the callus at different stages of healing in the case of a Ti plate ($\alpha=30^\circ$)

4.3.2.5 Elastic strain: compression and shear case

Due to the low Young's modulus of the callus in the assembly during the healing process, and also due to the location of the fracture plate, the maximum equivalent von-Mises elastic strain is at the bottom side of the bone, farthest away from the plate. Table 4.20 presents the amounts of these elastic strains in the assembly.

Table 4.20: Maximum equivalent elastic Von Mises strains in different parts of the assembly

	α (degree)	Maximum equivalent strain			
		1 st week	3 rd week	6 th week	8 th week
Bone	45	1.23	0.017	0.017	0.017
	30	0.92	0.011	0.011	0.011
	15	0.54	0.0056	0.0056	0.0056
Plate	45	0.004	0.0039	0.0039	0.0039
	30	0.0028	0.0027	0.0027	0.0027
	15	0.0019	0.0014	0.0014	0.0014
Screw	45	0.0073	0.0043	0.0043	0.0043
	30	0.0054	0.0031	0.0031	0.0031
	15	0.0031	0.0016	0.0016	0.0016
Callus	45	1.24	0.0048	0.0035	0.0028
	30	0.92	0.0035	0.0026	0.0021
	15	0.54	0.0020	0.0015	0.0012

Section 4.4 presents a comparison and discussion of the assembly with the SS plate and the Ti plate.

4.3.2.6 Contact analysis of the bone-Ti plate interface: compression and shear case

Similar to the SS plate, there exists frictional contact, sliding, at the interface of the bone and the fracture plate (figure 4.36).

Status
Type: Status
Time: 1
01/03/2008 7:59 PM

- Far
- Near
- Sliding
- Sticking

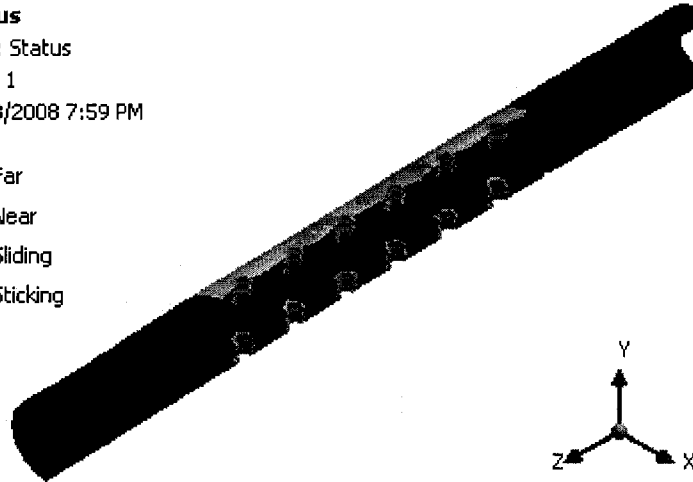


Figure 4.36: Contact at the bone and the Ti fracture plate interface for the 3rd week of healing ($\alpha=30^\circ$)

In the 1st week of healing for $\alpha=45^\circ$, the maximum sliding between the bone and the fracture plate occurred in the callus (figure 4.37).

Sliding Distance
Type: Sliding Distance
Unit: m
Time: 1
01/03/2008 8:02 PM

- 1.6e-6 Max
- 1.5e-6
- 1.4e-6
- 1.3e-6
- 1.2e-6
- 1.1e-6
- 9.4e-7
- 8.2e-7
- 7e-7
- 5.8e-7
- 4.7e-7
- 3.5e-7
- 2.3e-7
- 1.2e-7
- 0 Min

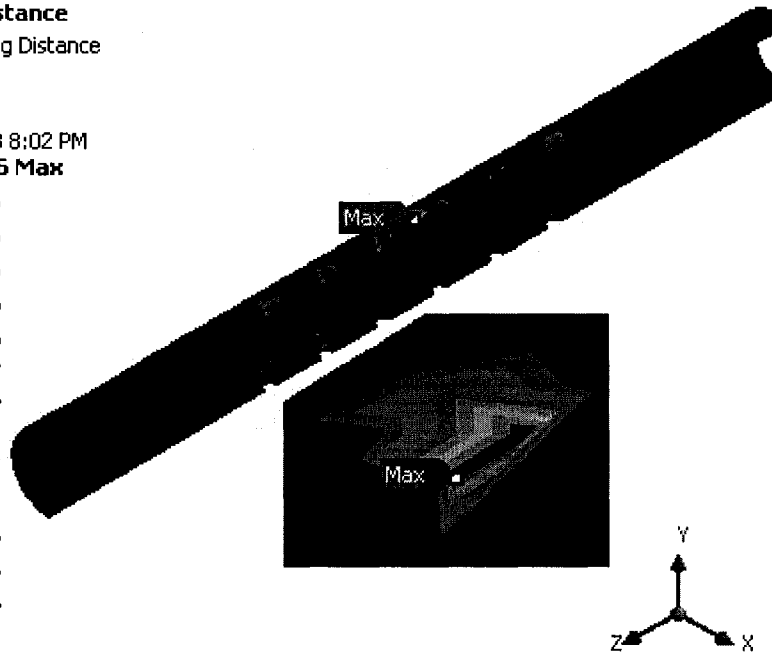


Figure 4.37: Relative motion between the bone and the Ti fracture plate for the 1st week of healing ($\alpha=45^\circ$)

For the rest of the healing period, this location was at the 4th screw hole close to the edge of the fracture plate (figure 4.38)

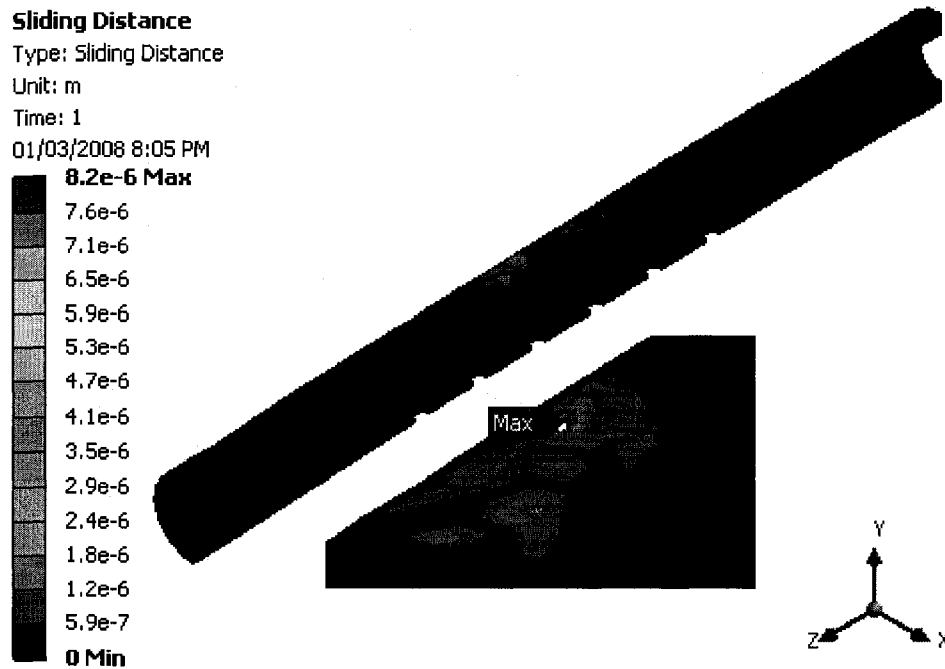


Figure 4.38: Relative motion between the bone and the Ti fracture plate for the 6th week of healing ($\alpha=45^\circ$)

The magnitude of these relative motions during the healing process for various angles is provided in table 4.21.

Table 4.21: Maximum relative motions at the interface of the bone and the Ti plate

α (degree)	Maximum relative motion (μm)			
	1 st week	3 rd week	6 th week	8 th week
45°	1.6	8.4	8.2	5.9
30°	2.7	8.2	8.0	8.0
15°	3.8	4.5	4.5	4.5

As presented in table 4.21, the maximum relative motion increases with the healing period for various angles except in the last week for $\alpha=45^\circ$ which decreases.

4.4 Summary and discussion: compression and shear case

In section 4.3 the results for the assembly with the SS plate and Ti plate were presented separately. This section presents a comparison of these two assemblies.

4.4.1 Summary and discussion of the stresses for both plates: compression and shear case

The maximum equivalent von-Mises stresses in each of the components of the assemblies at different stages of healing is given in table 4.22.

Table 4.22: Maximum equivalent von-Mises stresses at different stages of healing

		α (degree)	Maximum equivalent stress (MPa)			
			1 st week	3 rd week	6 th week	8 th week
Bone	45°	SS	339.3	294.4	294.4	294.2
		Ti	361.8	313.7	313.3	313.1
	30°	SS	236.0	203.1	203.0	202.9
		Ti	250.2	216.4	216.2	216.1
	15°	SS	116.1	98.3	98.2	98.2
		Ti	120.7	104.6	104.6	104.6
Plate	45°	SS	661.9	515.8	515.9	515.7
		Ti	384.1	379.6	379.1	378.8
	30°	SS	492.2	361.9	361.7	361.5
		Ti	271.9	266.3	266.0	265.8
	15°	SS	307.4	182.5	182.4	182.4
		Ti	179.6	135.0	135.0	135.0
Screw	45°	SS	1242.7	593.7	593.6	593.3
		Ti	697.8	419.3	418.6	418.2
	30°	SS	932.2	409.4	409.2	409.0
		Ti	515.9	295.1	294.7	294.3
	15°	SS	553.5	198.0	197.9	197.9
		Ti	297.3	151.6	151.6	151.6
Callus	45°	SS	22.9	38.2	41.9	45.2
		Ti	24.7	41.2	45.2	48.9
	30°	SS	17.0	28.2	30.9	33.9
		Ti	18.4	30.4	33.4	36.0
	15°	SS	9.9	16.5	18.0	19.6
		Ti	10.8	17.6	19.2	20.8

In all components, except for the callus, the maximum equivalent von-Mises stress remains the same after the 3rd week of healing.

The maximum equivalent von-Mises stress in the bone with the SS plate is always less than of that in the bone with the Ti plate. Conversely, the SS plate always has a higher stress than the Ti plate. Based on Wolff's law, in every composite system made by two materials in which one material is stiffer than the other, the stiffer material transmits the greater portion of the load. Since the titanium alloy is softer than the stainless steel, it helps the bone to bear a higher load. Therefore, it boosts the remodeling phase of the fracture healing.

Screws always have higher maximum stresses than the plates of the same material.

The callus always shows an increase in maximum stresses with longer healing periods, with the biggest increase in the first weeks. When a Ti fracture plate is used, callus transfers a higher portion of load compared to when a SS plate is used.

4.4.2 Summary and discussion of the strains for both plates: compression and shear case

The maximum equivalent von-Mises strain in the assembly for both the SS plate and the Ti plates at different stages of healing is given in table 4.23.

Table 4.23: Maximum equivalent von-Mises strains at different stages of healing

		α (degree)	Maximum equivalent elastic strain			
			1 st week	3 rd week	6 th week	8 th week
Bone	45°	SS	1.14	0.016	0.016	0.016
		Ti	1.23	0.017	0.017	0.017
	30°	SS	0.85	0.011	0.011	0.011
		Ti	0.92	0.011	0.011	0.011
	15°	SS	0.49	0.0052	0.0052	0.0052
		Ti	0.54	0.0056	0.0056	0.0056
Plate	45°	SS	0.0034	0.0027	0.0027	0.0027
		Ti	0.004	0.0039	0.0039	0.0039
	30°	SS	0.0026	0.0019	0.0019	0.0019
		Ti	0.0028	0.0027	0.0027	0.0027
	15°	SS	0.0016	0.0009	0.0009	0.0009
		Ti	0.0019	0.0014	0.0014	0.0014
Screw	45°	SS	0.0064	0.0031	0.0031	0.0031
		Ti	0.0073	0.0043	0.0043	0.0043
	30°	SS	0.0048	0.0021	0.0021	0.0021
		Ti	0.0054	0.0031	0.0031	0.0031
	15°	SS	0.0029	0.0010	0.0010	0.0010
		Ti	0.0031	0.0016	0.0016	0.0016
Callus	45°	SS	1.14	0.0044	0.0032	0.0026
		Ti	1.24	0.0048	0.0035	0.0028
	30°	SS	0.85	0.0033	0.0024	0.0019
		Ti	0.92	0.0035	0.0026	0.0021
	15°	SS	0.50	0.0019	0.0014	0.0011
		Ti	0.54	0.0020	0.0015	0.0012

The maximum equivalent von-Mises strains in the bone with both the SS plate and Ti plate follow the same pattern as shown in the maximum equivalent von-Mises stress, except for the callus.

During the healing period and for the various α , the Young's modulus of the newly-formed callus increases. Therefore, the magnitude of strains reduces during the healing period. For example, during the 1st week of healing and when $\alpha=30^\circ$, the

maximum equivalent von-Mises strain in the model with SS plate is 0.85. It reduces to 0.0019 at the end of healing period and the trend is completely downward. In case of a Ti plate, It is 0.92 in the 1st week and reduces to 0.0021 at the end of the healing period.

4.4.3 Summary and discussion of the contact analysis at the interface of bone-fracture plate

Sliding at the interface of the bone and the fracture plate does not follow a specific trend. The magnitudes of these relative motions are presented in table 4.24.

Table 4.24: Maximum relative motions at the interface of bone and fracture plate

α (degree)		Maximum relative motion (μm)			
		1 st week	3 rd week	6 th week	8 th week
45°	SS	1.22	3.04	4.79	4.82
	Ti	1.67	8.40	8.24	5.96
30°	SS	1.88	2.69	3.19	3.56
	Ti	2.71	8.16	8.02	8.02
15°	SS	4.08	3.33	3.31	3.30
	Ti	3.79	4.50	4.47	4.45

Figure 4.39 illustrated the changes of relative motion for various α in the model with a SS plate.

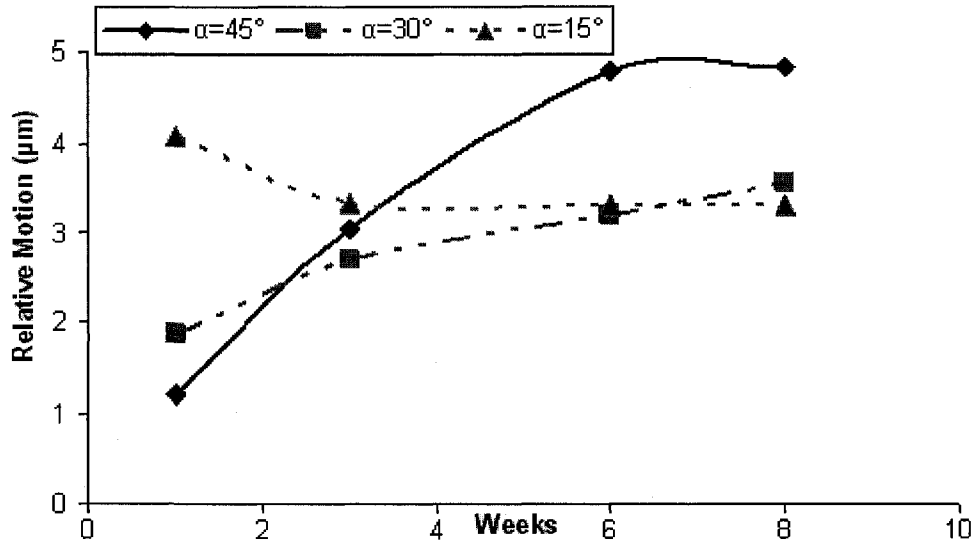


Figure 4.39: Relative motion changes with respect to the stage of healing in the model with the SS plate

As shown in figure 4.39, the trend for $\alpha=30^\circ$ and $\alpha=45^\circ$ is upward and it is downward for $\alpha=15^\circ$. This trend is different in the case of a Ti plate. Figure 4.40 shows the changes of the maximum relative motion at the interface of the bone and the Ti plate.

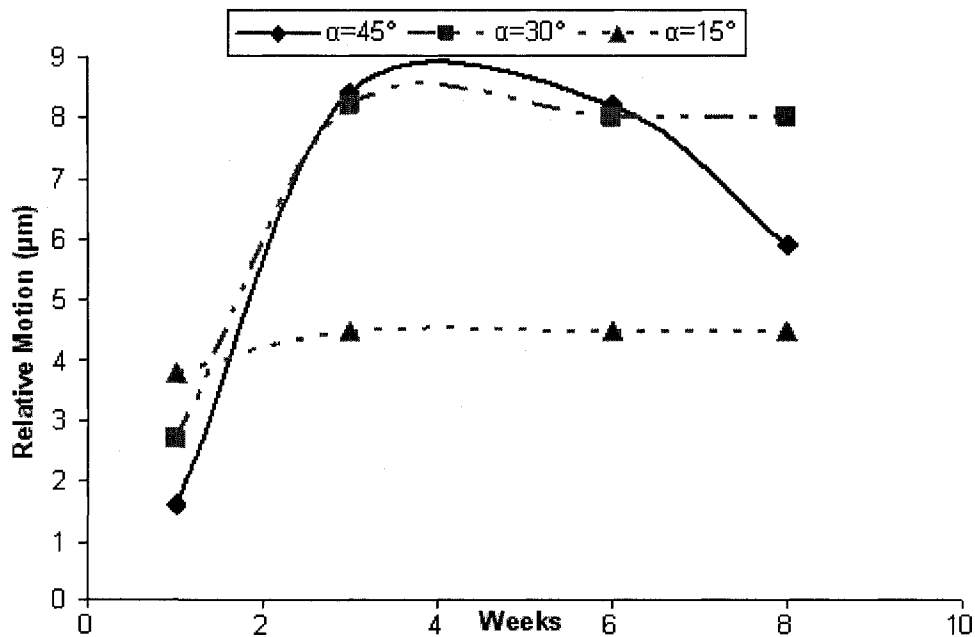


Figure 4.40: Relative motion changes with respect to the stage of healing in the model with the Ti plate

In this case, the trend of changes for various α until the 3rd week of healing is upward. After the 3rd week, for $\alpha=15^\circ$ and $\alpha=30^\circ$, the maximum relative motion remains steady with very slight changes during the rest of the healing period. For $\alpha=30^\circ$, sliding reduces in the following weeks of healing. The magnitude of these relative motions is already presented in table 4.24.

4.5 Load case 4 – twisting moment

In this case, a twisting moment of 6.4 Nm is applied to the assembly along the long axis of the bone. The following sections describe the stress distribution in each of the components in both models and a summary table is presented at the end.

4.5.1 Stress distribution in the bone: twisting moment case

The maximum equivalent von-Mises stress in the bone with the SS and Ti plates during the 1st week of healing was 210.6 MPa and 269.1 MPa, respectively. In the 3rd week of healing, the magnitude of this stress in the bone with the SS plate decreased by 50.4% to 104.5 MPa. This stress in the bone with the Ti plate reduced by 56.2% to 117.8 MPa. During the following weeks of healing, this magnitude remained nearly constant for the Ti plate with very minor changes while for the SS plate it stayed constant until the 6th week and then increased to 133.7 MPa in the last weeks of healing. Except for the last week of healing, the bone fixed with the Ti plate transfers a larger portion of load compared to the bone fixed with the SS plate. Figure 4.41 illustrates the stress distribution in the bone with the SS plate for the 3rd week of healing.

Equivalent Stress - Bone

Type: Equivalent (von-Mises) Stress

Unit: Pa

Time: 1

01/03/2008 8:12 PM

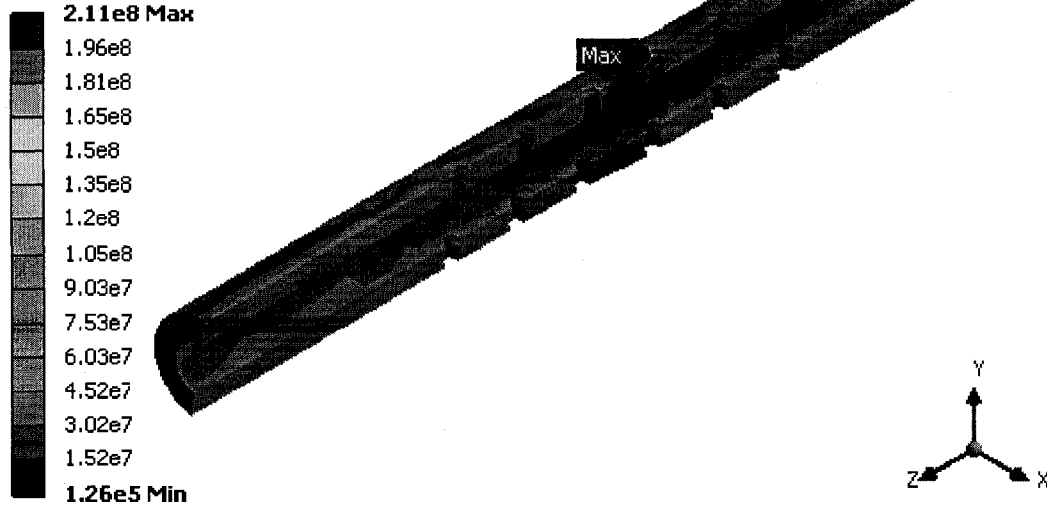


Figure 4.41: Stress distribution in the bone with the SS plate for the 3rd week of healing

For both the SS and Ti plates, the maximum equivalent von-Mises stress during the 1st week of healing occurred at the interface of the 6th screw and the hole (Figure 4.42). This location shifted to the interface of 1st screw and the hole for the rest of the healing period (figure 4.43).

Equivalent Stress - Plate

Type: Equivalent (von-Mises) Stress

Unit: Pa

Time: 1

01/03/2008 8:14 PM

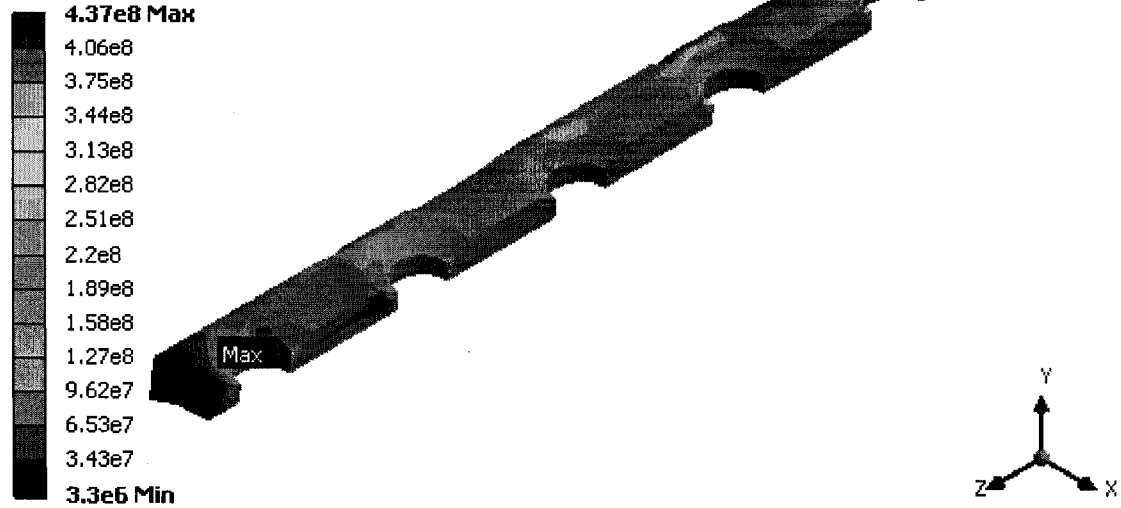


Figure 4.42: Stress distribution in the Ti fracture plate for the 1st week of healing

Equivalent Stress - Plate

Type: Equivalent (von-Mises) Stress

Unit: Pa

Time: 1

01/03/2008 8:16 PM

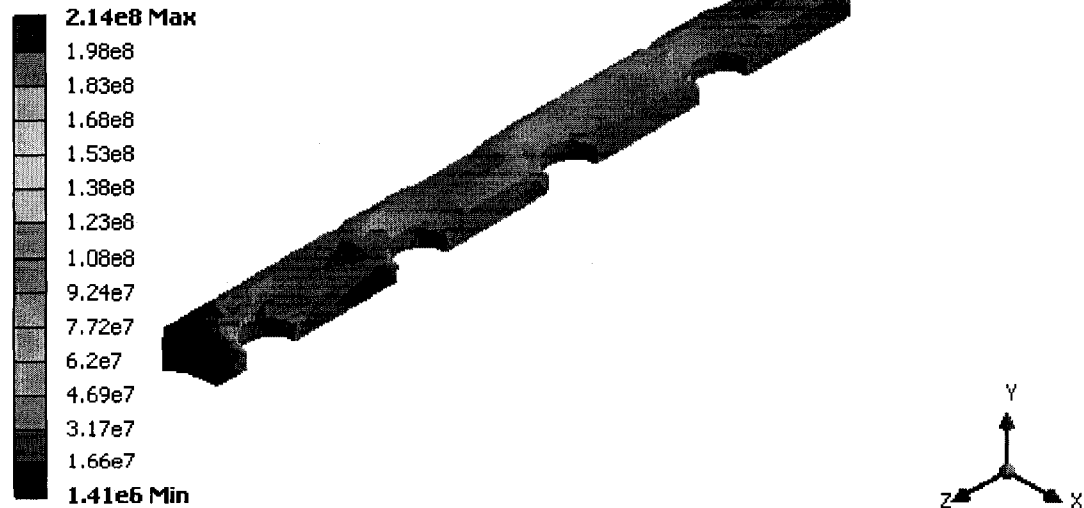


Figure 4.43: Stress distribution in the Ti fracture plate for the 6th week of healing

4.5.2 Stress distribution in the plate: twisting moment case

The maximum equivalent von-Mises stress during the 1st week of healing in the SS and the Ti plates was 452.9 MPa and 437.1 MPa, respectively. In the 3rd week of healing, this magnitude in the SS plate reduced to 213.2 MPa and stayed constant in the 6th week of healing and then increased to 283.9 MPa in the 8th week of healing. This trend was downward for the Ti plate and the amount of maximum equivalent stress reduced to 214.9 MPa in the 3rd week of healing and remained constant for the rest of healing period.

4.5.3 Stress distribution in the screws: twisting moment case

The maximum equivalent von-Mises stress in the stainless steel screws during the 1st week of healing was 1032.6 MPa. Since this amount is higher than the ultimate tensile strength of stainless steel (586 MPa), there is a failure in the screws. The stresses in the Ti screws are always less than the ultimate tensile stress of Ti-6Al-4V (1070 MPa). For the Ti screws the maximum stress was 858.2 MPa, which occurred in the 1st week of healing. This magnitude reduced to 499.5 MPa in the 3rd week for SS screws and with slight changes reduced to 487.1 MPa in the last week. For the Ti screws, this magnitude reduced to 386.3 MPa in the 3rd week and then reduced to 380.5 MPa in the last week of healing. The maximum equivalent von-Mises stress in the titanium screws during the entire healing period occurred in the 6th screw in the distal humerus (figure 4.44).

Equivalent Stress - Screws

Type: Equivalent (von-Mises) Stress

Unit: Pa

Time: 1

01/03/2008 8:20 PM

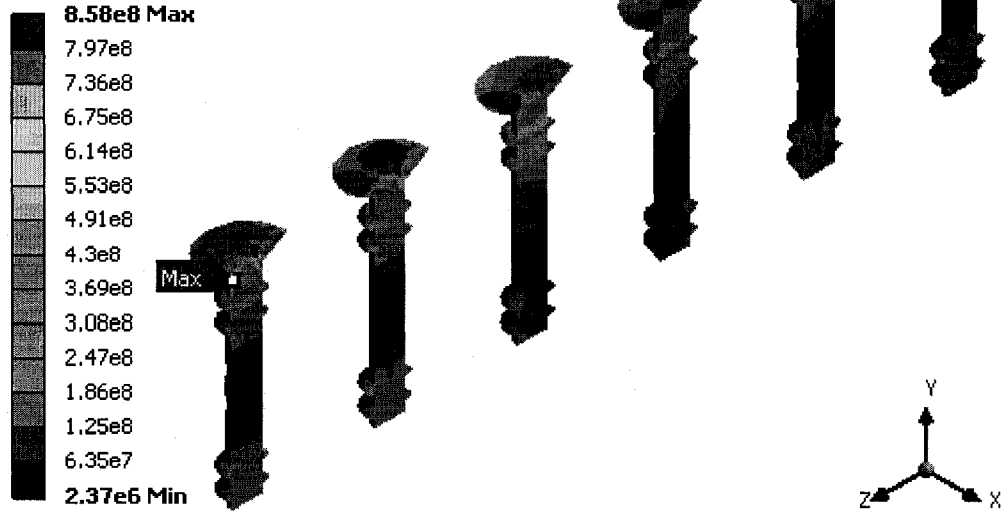


Figure 4.44: Stress distribution in the titanium screws for the 1st week of healing

In the model with the SS plate, the head of the 6th screw transferred the majority of load during most of the healing period, while this changed to the bottom of the 5th screw in the 8th week of healing (figure 4.45).

Equivalent Stress - Screws

Type: Equivalent (von-Mises) Stress

Unit: Pa

Time: 1

01/03/2008 8:23 PM

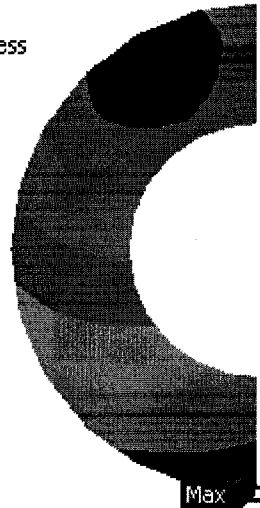
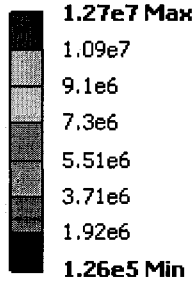


Figure 4.45: Stress distribution in the stainless steel screws for the 8th week of healing

4.5.4 Stress distribution in the callus: twisting moment case

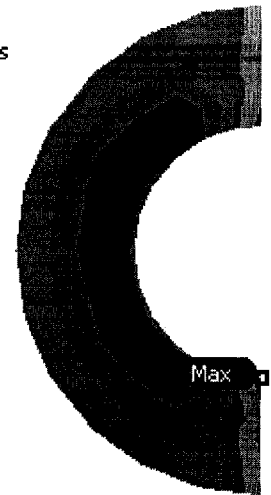
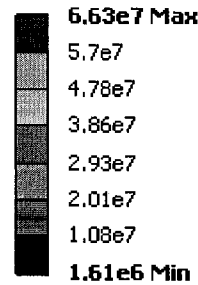
The maximum equivalent von-Mises stress was 12.7 MPa in the callus of the model with the SS plate during the 1st week of healing. This maximum stress was located at the bottom side of the callus farthest away from the fracture plate. For the Ti plate model, this was 14.2 MPa. In the 3rd week of healing, the maximum equivalent stress increased to 66.2 MPa with the SS plate model and then again went up by 28% to 85.2 MPa at the end of the healing period. The trend was the same with the Ti plate model, but with a peak of 93.1 MPa in the 8th week of healing. This means that a larger portion of load is transmitted through the newly-formed callus. The callus in the model with the Ti plate transfers more load than that with the SS plate. Figure 4.46 shows the stress distribution in the callus at different stages of healing in case of the SS plate.

Equivalent Stress - Callus
 Type: Equivalent (von-Mises) Stress
 Unit: Pa
 Time: 1
 10/02/2008 3:39 PM



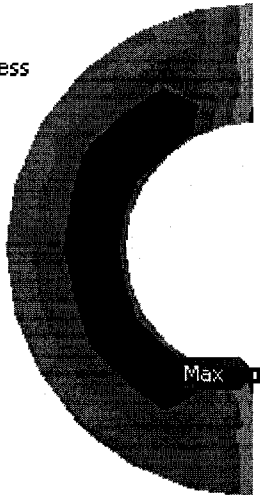
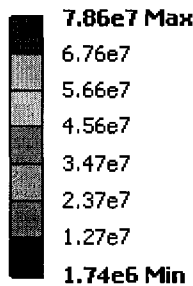
1st week

Equivalent Stress - Callus
 Type: Equivalent (von-Mises) Stress
 Unit: Pa
 Time: 1
 10/02/2008 3:40 PM



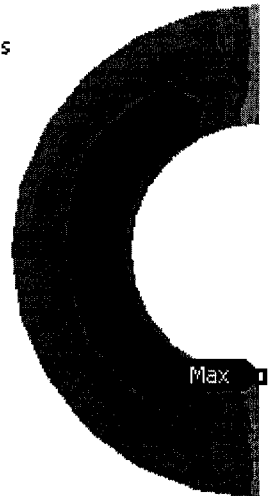
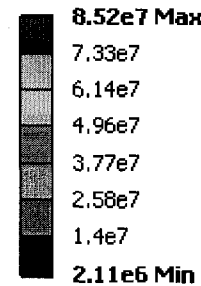
3rd week

Equivalent Stress - Callus
 Type: Equivalent (von-Mises) Stress
 Unit: Pa
 Time: 1
 10/02/2008 3:41 PM



6th week

Equivalent Stress - Callus
 Type: Equivalent (von-Mises) Stress
 Unit: Pa
 Time: 1
 10/02/2008 3:41 PM



8th week

Figure 4.46: Stress distribution in the callus at different stages of healing in case of the SS plate

4.5.5 Summary and discussion of the stresses: twisting moment case

Table 4.25 provides the maximum equivalent von-Mises stresses for different parts of the assembly, namely the bone, fracture plate, screws and callus at different stages of healing.

Table 4.25: Maximum equivalent von-Mises stresses in different parts of the assembly

		Maximum equivalent stress (MPa)			
		1 st week	3 rd week	6 th week	8 th week
Bone	SS	210.6	104.5	104.4	133.7
	Ti	269.1	117.8	111.6	111.5
Plate	SS	452.9	213.2	212.1	283.9
	Ti	437.1	214.9	213.6	212.9
Screw	SS	1032.6	499.5	495.1	487.1
	Ti	858.2	386.3	382.6	380.5
Callus	SS	12.7	66.3	78.5	85.2
	Ti	14.2	69.6	82.5	93.1

The maximum equivalent von-Mises stress in the assembly during the 1st week of healing for both the SS and Ti plates occurs at the 6th screw. The magnitude of this stress is 1032.6MPa with the SS plate and 858.2 MPa with the Ti plate. As already discussed in previous load cases, since the maximum equivalent von-Mises stress with the SS plate exceeds the ultimate strength of stainless steel, fracture happens in the screw. Therefore, excessive loading should be avoided. On the other hand, this amount for the bone with the Ti plate is 858.2 MPa which is less than the ultimate strength of Ti-6Al-4V, so that there is no failure in the titanium screws.

4.5.6 Elastic strain: twisting moment case

The maximum equivalent von-Mises elastic strains in these models in the 1st week of healing occurred in the callus farthest away from the plate. However, for the rest of the healing period, this location shifted to the interior side. Table 4.26 presents the amount of these elastic strains for different parts of the assembly.

Table 4.26: Maximum equivalent elastic von-Mises strains in different parts of the assembly

		Maximum equivalent elastic strain			
		1 st week	3 rd week	6 th week	8 th week
Bone	SS	0.63	0.0077	0.0062	0.0093
	Ti	0.71	0.0081	0.0068	0.0068
Plate	SS	0.0023	0.011	0.011	0.015
	Ti	0.0023	0.011	0.011	0.011
Screw	SS	0.0054	0.0026	0.0026	0.0026
	Ti	0.0089	0.0040	0.0040	0.0040
Callus	SS	0.63	0.0077	0.0061	0.0049
	Ti	0.71	0.0081	0.0064	0.0054

4.5.7 Contact analysis of the bone-plate interface: twisting moment case

For the entire healing period, the maximum sliding distance between the bone and the fracture plate occurred at the proximal end of the contact area for both the SS and Ti plates (figure 4.47).

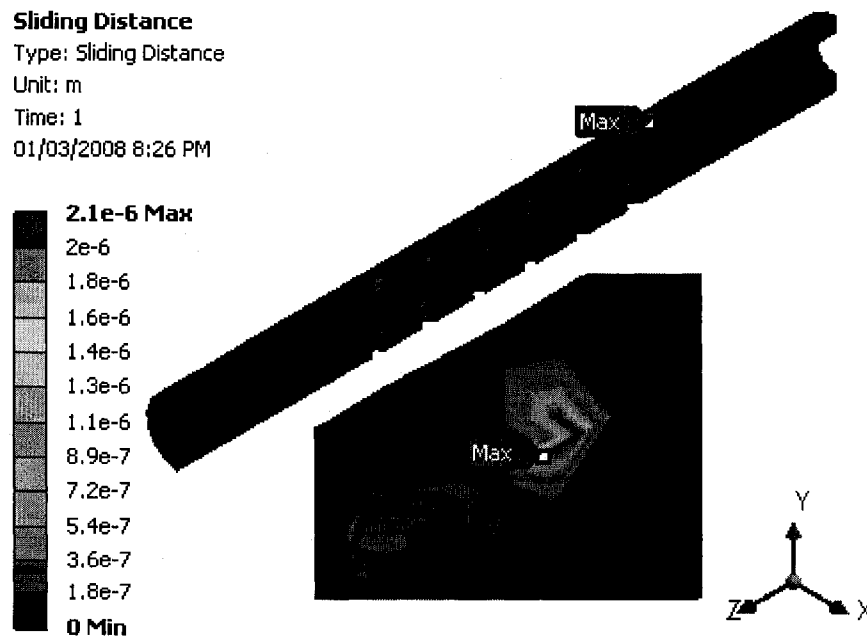


Figure 4.47: Relative motion between the bone and the Ti plate for the 3rd week of healing

Figure 4.48 illustrates the contact at the interface of the bone and the Ti plate in the 3rd week of healing.

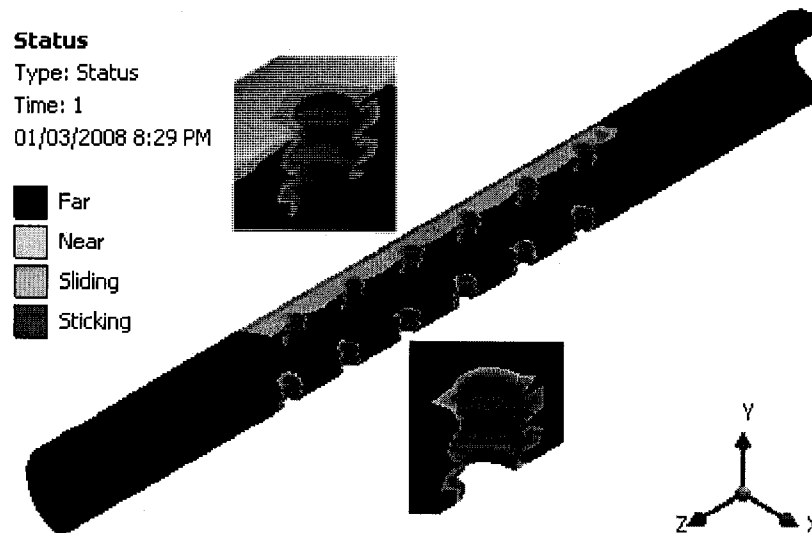


Figure 4.48: Contact at the bone and the Ti plate interface for the 3rd week of healing

The magnitude of the relative motions is presented in table 4.27.

Table 4.27: Maximum relative motions at the interface of bone-fracture plate

	Maximum relative motion (μm)			
	1 st week	3 rd week	6 th week	8 th week
SS	4.72	1.46	1.42	2.79
Ti	8.96	2.15	2.06	2.00

As can be seen in the table 4.18, the magnitude of the relative motion in the contact area with the SS plate was 4.72 μm during the 1st week of healing and then reduced to 1.46 μm in the following week and stayed steady by the end of the 6th week. Again, in the 8th week of healing, the amount of sliding increased by about 46.7% to 2.79 μm . This magnitude with the Ti plate was 8.96 μm in the 1st week and decreased to 2.15 μm in the 3rd week of healing and then reduced again to 2.00 μm at the end of the healing period.

5. Conclusion and future work

In this research, a three dimensional finite element model of a mid-shaft fracture of the humerus with different internal fracture fixation plates was generated. This model was used to calculate the internal states of stress and strain in the assembly and also to evaluate the performance of the fracture plates under different load conditions. The model consists of bone, callus, fracture plate and screws. The FE Static Structural package of Ansys Workbench 11.0 was used to mesh the parts. Three different element types were used to generate the mesh for the solid parts.

Interfaces of bone-screw and fracture plate-screw head were defined as bonded contact which means there was no slippage between these two parts while the interface of bone and fracture plate was defined as frictional contact, allowing for slippage between bone and fracture plate.

The model was considered to be half-symmetry about the long axis of the bone. The loads applied to the model were static. Four types of loading were applied to the model: pure compression, pure tension, twisting, and a combination of compressive and shear forces which also generate a bending moment.

The analysis shows that the maximum equivalent von-Mises stresses under pure compression and pure tension loads are less than those under bending and torsion loads.

The titanium fracture plate with titanium screws always shows a better performance compared to stainless steel. In the case of bending or twisting loads, stainless steel plate and screws show failure in some cases, while the titanium plate and

screws do not. For the same load conditions, the stainless steel plate carries more load and the bone carries less load compared to the case with a titanium plate. Thus, the use of a titanium fracture plate enhances the performance of the system by reducing the amount of stress shielding in the underlying bone.

The screws play a key role in transferring the load. For compression, tension and bending loads the majority of load transfers through the 1st screw, in the proximal humerus, and through the 6th screw, in the distal humerus, for the twisting load case, Similar to the fracture plate case, stainless steel screws showed failure under bending and twisting loads while titanium screws did not.

The maximum equivalent von-Mises stress and strain in the callus always occur farthest away from the fracture plate. Maximum equivalent stress in the callus always increases and maximum equivalent von-Mises strain always decreases during the healing period.

In the case of micro-motion between the bone and fracture plate, the maximum sliding occurs under tension load while the smallest amount of relative motion occurs under compressive load.

The following are some suggestions for future work:

1. Investigation of the effect of different bone material properties to simulate e.g. brittle bones.
2. Incorporation of a shape of the bone that more closely resembles the actual humerus.

3. Investigation of frictional contact at the interface of bone-screw and fracture plate-screw heads based on the values of friction coefficients extracted from mechanical tests.
4. Investigation of oblique and butterfly fractures of the bone and also different angles of the screws with respect to the long axis of the bone.
5. Redesign the fracture plate to have rounded edges and corners.
6. Study the application of a composite material in design of the fracture plate.
7. Experimental validation of the stress and strain results in the assembly.

6. References

Ansys (www.ansys.com)

Ashman, R. B. and van Buskirk, W. C. (1987) The elastic properties of a human mandible, *Advances in Dental Research*, **1**, pp. 64-67

Beaupre, G. S., Schneider, E. and Perren, S. M. (1984) Stress analysis of a partially slotted intramedullary nail, *Journal of Orthopaedic Research*, **2**, pp. 369-376

Beaupre, G. S., Carter, D.R., Orr, T.E. and Csongradi, J. (1988) Stresses in plated long-bones: The role of screw tightness and interface slipping, *Journal of Orthopaedic Research*, **6**, pp. 39-50

Boeree, N. R., Dove, J., Cooper, J. J., Knowles, J. and Hastings, G. W. (1993) Development of a degradable composite for orthopaedic use: mechanical evaluation of a hydroxyapatite-polyhydroxybutyrate composite material, *Biomaterials*, **14**, pp. 793-796

Browner, B. D. and Edwards, C. C. (1996) *The Science and Practice of Intramedullary Nailing*, Lippincott Williams & Wilkins, 2nd edition

Carter, D. R., Vasu, R. and Harris, W. H. (1981) The plated femur: relationships between the changes in bone stresses and bone loss. *Acta Orthopaedica Scandinavica*, **52**, pp. 241-248

Chao, E. Y. S. and Aro, H. T. (1997) Biomechanics of Fracture Fixation, *Basic Orthopaedic Biomechanics*, Lippincott-Raven Publishers, Philadelphia

Claes, L. (1989) The mechanical and morphological properties of bone beneath internal fixation plates of differing rigidity, *Journal of Orthopaedic Research*, **7**, pp. 170-177

Clavert, P., Zerah, M., Krier, J., Mille, P., Kempf, J. F. and Kahn, J. L. (2006) Finite element analysis of the strain distribution in the humeral head tubercles during abduction: comparison of young and osteoporotic bone, *Surgical and Radiologic Anatomy*, **28**, pp. 581-587

Cordey, J., Perren, S. M. and Steinemann, S. G. (2000) Stress protection due to plates: myth or reality? A parametric analysis made using the composite beam theory, *Injury*, **31**, pp. 1-13

Cowin, S.C. (1989) *Bone Mechanics*, CRC Press Inc., New York.

Einhorn, T. A. (1998) The cell and molecular biology of fracture healing, *Clinical Orthopaedics and Related Research*, **355**, pp. 7-21

Fazzini (www.fazzini.it)

Ferguson, S. J., Wyss, U. P. and Pichora, D. R. (1996) Finite element stress analysis of a hybrid fracture fixation plate, *Medical Engineering and Physics*, **18**, pp. 241-250

Ferguson, S. J., (1994) A three-dimensional finite element analysis of an axially flexible fracture fixation plate, M.Sc. thesis, Queen's University, Kingston, Ontario

Firoozbakhsh, K., Aleyaasin, M. and Moneim, M. S. (1992) Evolution of bone inhomogeneity around a hole in an orthotropic plate of bone: theoretical predictions, *Journal of Biomechanics*, **25**, pp. 387-94

Foux, A., Uthoff, H. K. and Black, R. C. (1993) Healing of plated femoral osteotomies in dogs. A mechanical study using a new test method, *Acta Orthopaedica Scandinavica*, **64**, pp. 345-353

Foux, A., Yeadon A., and Uthoff H. K. (1995) Improved fracture healing with less rigid plate: a biomechanical study in dogs, *Clinical Orthopaedics and Related Research*, **339**, pp. 232-245

Ganesh, V. K., Ramakrishna, K. and Ghista, D. N. (2005) Biomechanics of bone-fracture fixation by stiffness-graded plates in comparison with stainless-steel plates, *BioMedical Engineering OnLine*, **4**:46

Gautier, E., Perren, S. M. and Cordey, J. (2000) Effect of plate position relative to bending direction on the rigidity of a plate osteosynthesis. A theoretical analysis, *Injury*, **31**, pp. 14-20

Gómez-Benito, M. J., Garcia-Aznar, J. M., Kuiper, J. H. and Doblaré, M. (2006) A 3D Computational Simulation of Fracture Callus Formation: Influence of the Stiffness of the External Fixator, *Journal of Biomechanical Engineering*, ASME, **128**, pp. 290-299

Hart, R. T. and Davy, D. T. (1989) Theories of Bone Modeling and Remodeling. In Cowin, S.C.: *Bone Mechanics*. New York, CRC Press, pp. 253-277

Hayes W. C., and Mow, V. C. (1991) Biomechanics of cortical and trabecular bone: Implications for assessment of fracture risk, *Basic Orthopaedic Biomechanics*, Raven Press, New York, pp. 93-142

Hayes, W. C., Swenson Jr, L. W. and Schurman, D. J. (1978) Axisymmetric finite element analysis of the lateral tibial plateau, *Journal of Biomechanics*, **11**, pp. 21-33

Hipp, J. A., Edgerton, B. C., An, K. N. and Hayes, W. C. (1990) Structural consequences of transcortical holes in long bones loaded in torsion, *Journal of Biomechanics*, **23**, pp. 1261-1268

Holzach, P., Matter, P. (1978) The comparison of steel and titanium dynamic compression plates used for internal fixation of 256 fractures of the tibia, *Injury*, **10**(2), pp. 120-123

La Budde, J. K., Orosz, J. F., Bodgho, T. A., Pellegrini, V. D. Jr. (1994) Particulate titanium and cobalt-chrome metallic debris in failed total knee arthroplasty: A quantitative histologic analysis, *Journal of Arthroplasty*, **9**(3), pp. 291-304

Lawrence, J. K. (2000) *Mechanics of Hard Tissue*, The Biomedical Engineering Handbook, Edited by Joseph, E. and Bronzino, D., CRC Press

Lin, C. L., Lin, Y. H. and Chen, A. C. Y. (2006) Buttressing angle of the double-plating fixation of a distal radius fracture: a finite element study, *Medical & Biological Engineering and Computing*, **44**, pp. 665-673

Lovald, S. T., Khraishi, T., Wagner, J., Baack, B., Kelly, J. and Wood, J. (2006) Comparison of plate-screw systems used in mandibular fracture reduction: finite element analysis, *Journal of Biomechanical Engineering*, ASME, **128**, pp. 654-662

Manninen, M. J., Paivarinta, U., Taurio, R., Tormala, P., Suuronen, R., Raiha, J., Rokkanen, P., and Patiala, H. (1992) Polylactide screws in the fixation of olecranon osteotomies: a mechanical study in sheep, *Acta Orthopaedica Scandinavica*, **63**, pp. 437-442

McKibbin, B. (1978) The biology of fracture healing in long bones, *Journal of Bone and Joint Surgery (Br)*, **60(B)**, pp. 150-162

McRae, R. (2002) *Practical Fracture Treatment*, Churchill Livingstone, New York, 4th edition

Millar, B. G., Frame, J.W. and Browne, R. M. (1990) A histological study of stainless steel and titanium screws in bone, *British Journal of Oral and Maxillofacial Surgery*, **28(2)**, pp. 92-95

Narang Medical Limited (www.narang.com)

Perren, S. M. (1979) Physical and biological aspects of fracture healing with special reference to internal fixation, *Clinical Orthopaedics and Related Research*, **138**, pp. 175-196

Pheasant, S. (1986) *Bodyspace: Anthropometry, Ergonomics and the Design of Work*, Taylor & Francis, Philadelphia

Ramakrishna, K., Sridhar, I., Sivashanker, S., Khong, K. S. and Ghista, D. N (2004) Design of fracture fixation plate for necessary and sufficient bone stress shielding, *JSME International Journal Series C*, **47**, pp. 1086-1094

Robert, K. Q. III, Chandler, R. Baratta, R. V., Thomas, K. A. and Harris, M. B. (2003) The effect of divergent screw placement on the initial strength of plate-to-bone fixation, *The Journal of Trauma: Injury, Infection, and Critical Care*, **5**(6), pp. 1139–1144

Rybicki, E. F. and Simonen, F. A. (1977) Mechanics of oblique fracture fixation using a finite-element model, *Journal of Biomechanics*, **10**, pp. 141-148

Saidpour, S. H. (2006) Assessment of carbon fibre composite fracture fixation plate using finite element analysis, *Annals of Biomedical Engineering*, **34**, pp. 1157-1163

Salter, R. B. (1999), *Textbook of Disorders and Injuries of the Musculoskeletal System*, Lippincott, Williams & Wilkins, 3rd edition

Salvati, E. A., Betts, F., Doty, S. B. (1993) Particulate metallic debris in cemented total hip arthroplasty, *Clinical Orthopaedics and Related Research*, **293**, pp. 160-173

Schatzker, J. and Tile, M. (2005) *The Rationale of Operative Fracture Care*, Springer, 3rd edition

Simon, B. R., Woo, S. L., Stanley, G. M., Olmstead, S. R., McCarty, M. P., Jemmott, G. F. and Akeson, W. H. (1977) Evaluation of one-, two-, and three-dimensional finite element and experimental models of internal fixation plates, *Journal of Biomechanics*, **10**, pp. 79-86

Suuronen, R., Pohjonen, T., Vasenius, J. and Vainionpaa, S. (1992) Comparison of absorbable self-reinforced multilayer poly-L-lactide and metallic plates for the fixation of mandibular body osteostomies: an experimental study in sheep, *Journal of Oral and Maxillofacial Surgery*, **50**, pp. 255-262

Taira, M. and Lautenschlager, E. P. (1992) In vitro corrosion fatigue of 316L cold worked stainless steel, *Journal of Biomedical Materials Research*, **26(9)**, pp. 113-119

Tencer, A. F. and Johnson, K. D. (1994) *Biomechanics in Orthopaedic Trauma: Bone Fracture and Fixation*, Informa Healthcare, 1st edition

Thibodeau, G. A. and Patton, K. T. (2007) *Anatomy & Physiology*, 6th Edition, Elsevier

Uhthoff, H. K., Bardos, D. and Liskova-Kiar, M. (1981) The advantages of titanium alloy over stainless steel plates for the internal fixation of fractures. An experimental study in dogs, *Journal of Bone and Joint Surgery (Br)*, **63**, pp. 427-484

Van der Elst, M., Dijkema, A. R. A., Klein, C. P. A. T., Pakta, P. and Haarman, H. J. Th. M. (1995) Tissue Reaction on PLLA versus stainless steel interlocking nails for fracture fixation: an animal study, *Biomaterials*, **16(2)**, pp. 103-106

Van Dongen, R. (1963) The shoulder girdle and humerus of the Australian Aborigine, *American Journal of Physical Anthropology*, **21**, pp. 469-488

Zadpoor, A. A. (2006) Finite element method analysis of human hand arm vibrations,
The International Journal of Scientific Research, **16**, pp. 391-395